ABSTRACT

Title of Thesis: TRAJECTORY OPTIMIZATION AND AERODYNAMIC MODELING OF LONG RANGE MORPHING PROJECTILES

Degree candidate: Kevin Ryan

Degree and year: Master of Science, 2011

Thesis directed by: Professor Mark J. Lewis
Department of Aerospace Engineering

The use of pattern search and gradient-based optimization methods to determine optimal geometries of morphing guided unpowered projectiles are examined. An investigation of continuously varying geometries vs. discrete-point morphing concepts is performed. A detailed aerodynamic analysis, applicable to a wide flight envelope, is coupled with a trajectory simulation program for use within the optimization schemes. Optimal projectile geometries that give maximum range subject to the constraints of static stability and trimmed conditions were then determined. Deployment of a single optimum geometry set of wings and canards at apogee provided a 98.6% increase in range over the baseline projectile configuration. Dual geometry and continuous morphing schemes increased the range over the baseline geometry by an additional 3.4% and 12.1% respectively. The trade off between range and morphing complexity showed that deployment of a single optimized geometry was the most beneficial for unguided unpowered 155mm projectiles.

TRAJECTORY OPTIMIZATION AND AERODYNAMIC MODELING OF LONG RANGE MORPHING PROJECTILES

by

Kevin Ryan

Thesis submitted to the Faculty of the Graduate School of the
University of Maryland, College Park in partial fulfillment
of the requirements for the degree of
Master of Science
2011

Advisory Committee:
Professor Mark J. Lewis, Chairman/Advisor
Professor Christopher Cadou
Professor Ken Yu

© Copyright by
Kevin Ryan
2011

Dedication

To my parents John and Sheryl, my brother Michael, and my sister Christine. Everything that I have accomplished wouldn't have been possible without the love and support that you have given me throughout my life. Thank you!

Acknowledgments

I would like to thank my advisor Dr. Mark Lewis for giving me the opportunity to conduct this research. His vast knowledge and passion for the field of aerospace engineering has inspired me throughout the completion of this thesis and continues to do so. I would also like to thank my committee members Dr. Cadou and Dr. Yu whose instruction helped lay the foundation necessary for my research. Their time and effort is much appreciated.

I would like to acknowledge the US Army Research Lab funding that supported this work. Much appreciation is expressed to Ilmars Celmins, Ed Schmidt, Fred Brandon, and all of the fine people at ARL who has supported my efforts on this project. A special thanks to Fred Brandon for providing his help and expertise in using PRODAS. His instruction and advice has been extremely helpful.

Finally I would like to thank my fellow coworkers in the hypersonics group (Neal Smith, Vijay Ramasubramanian, Adam Beerman, Jeremy Knittel, Gillian Bussey, and Leslie Eurice) whose help and support I could not have done with out. Also, I would like to thank Ian Smith for his interest in discussing projectile optimization and always providing me with helpful advice and thought experiments.

Table of Contents

List of Tables

List of Figures

List of Symbols and Abbreviations

A	=	Aspect ratio
a_t	=	$\beta \tan\left(\frac{\pi}{2} - \Lambda_{LE}\right)$
b	=	Span at trailing edge (mm)
C_D	=	Drag coefficient
C_L	=	Lift coefficient
C_m	=	Pitching moment coefficient
C_N	=	Normal force coefficient
Cp	=	Pressure coefficient
C_S	=	Suction force coefficient
c	=	root chord (mm)
d	=	Missile max diameter (mm)
E	=	Complete elliptic integral of the second kind
$\vec{e}$	=	vector of ones the size of $\vec{G}$
$F\left(\vec{X}\right)$	=	Objective function
$F_m\left(\vec{X}\right)$	=	Approximate objective function
fn	=	Nose fineness ratio = $\frac{ln}{d}$
$G\left(\vec{X}\right)$	=	Nonlinear inequality constraint function
$\vec{G}$	=	Vector of constraint functions
G_j	=	j-th constraint
H	=	Hessian matrix
h	=	Altitude (increments of 10km)
I	=	Identity matrix
J	=	Jacobian matrix of constraint functions
$K_{B(f)}$	=	Body-fin influence factor
K_b	=	Boattail correction factor
$K_{F(b)}$	=	Fin-body influence factor
K_p	=	Potential flow constant of proportionality
K_T	=	Total influence factor
K_v	=	Vortex flow constant of proportionality
$\frac{L}{D}$	=	Lift to drag ratio
ln	=	Nose length (mm)
M	=	Mach number
m	=	Barrier parameter
N	=	Number of design variables
p	=	Pressure (Pa)
q	=	Dynamic pressure = $\frac{1}{2}\rho U^2$ (Pa)
Re	=	Reynolds number
S	=	Reference Area (m^2)
$\vec{S}$	=	Vector of slack variables
S_{diag}	=	Diagonal matrix of slack variables
S_j	=	j-th slack variable of j-th constraint
U	=	Velocity (m/s)

$\vec{X}$	=	Vector of design variables
X_{cg}	=	Distance to the center of gravity measured from the base (calibers)
X_{cp}	=	Distance to the center of pressure measured from the base (calibers)
X_i	=	i-th design variable
Y	=	Sutherland constant (K)
α	=	Body angle of attack (deg)
β	=	$\sqrt{M_\infty^2 - 1}$
Γ	=	Total effective circulation (m^2/s)
γ	=	Ratio of specific heats
Δ	=	Some small increment
δ	=	Canard angle of attack (deg)
ϵ	=	Mach cone semi-vertex angle (deg)
Θ	=	Lagrangian barrier function
κ	=	Launch angle (deg)
$\Lambda_{\frac{1}{2}}$	=	Complementary angle to wing semi-vertex angle at mid-chord (deg)
Λ_{diag}	=	Diagonal matrix of Lagrange multipliers
Λ_{LE}	=	Leading edge sweep angle (deg)
$\vec{\lambda}$	=	Vector of Lagrange multipliers
λ_j	=	j-th Lagrange multiplier
μ	=	Dynamic viscosity (Pa·s)
ρ	=	Density (kg/m^3)
ϕ	=	Velocity potential equation (m^2/s)
ψ	=	Wing angle of attack (deg)

Superscripts

L	=	Lower bound
T	=	Transpose matrix
U	=	Upper bound
$*$	=	Optimum design

Subscripts

0	=	Coefficient at zero lift
base	=	Missile base component
body	=	Missile body component
bt	=	Including boattail
*c*1	=	Configuration 1
*c*2	=	Configuration 2
canard	=	Missile canard component
cs	=	With respect to missile cross section
f	=	Due to friction
i	=	Induced
L	=	Equivalent flat plate length
nbt	=	No boattail
nose	=	Missile nose component

$norm$	=	Normalized
pf	=	With respect to wing, fin, or canard planform area
$plate$	=	Flat plate
s	=	Sutherland reference parameter
$ssle$	=	Supersonic leading edge conditions
$sonic$	=	Sonic leading edge conditions
v	=	Vortex contribution
w	=	Wave drag component
wet	=	Wetted surface
$wing$	=	Missile wing/fin component
α	=	$\frac{\partial}{\partial \alpha}$
ϕ	=	Potential contribution
ψ	=	$\frac{\partial}{\partial \psi}$
$-comb$	=	Wing-body combination
∞	=	Freestream

Acronyms

ALPS	=	Augmented Lagrangian Pattern Search
DATCOM	=	Data Compendium
GADS	=	Genetic Algorithm and Direct Search
KKT	=	Karush-Kuhn-Tucker
MATLAB	=	Matrix Laboratory
NASA	=	National Aeronautics and Space Administration
NSWC AP	=	Naval Surface Warfare Center Aeroprediction
POST	=	Program to Optimize Simulated Trajectories
PRODAS	=	Projectile Rocket Ordnance Design and Analysis System
RAeS	=	Royal Aeronautical Society

Chapter 1

Introduction

1.1 Motivation

An aircraft or projectile flying across a range of mission legs or flight regimes inherently requires a compromise in performance. An aircraft can be well suited for a cruise or dash mission leg, yet would suffer a performance penalty when operating in a loiter mission leg. Similarly, a projectile designed for high altitude subsonic flight will suffer during low altitude or supersonic flight. Incorporating configuration or shape changes to the aircraft or projectile during flight can potentially improve performance when operating in off-design conditions.

This idea of a morphing aircraft has been around since the dawn of human powered flight. The Wright brothers' aircraft used a variable twist wing for increased roll control. The integration of slats or flaps on a wing can essentially be seen as a morphing wing of variable wing camber. The development of the swing wing on the F-14 fighter jet allows for a variable wing aspect ratio. The benefits of morphing bodies is so promising that even over 100 years after the Wright brothers' first flight, the research community is actively pursuing all aspects of morphing technologies [1, 2].

The present work applies the idea that the morphing wing strategies for aircraft can be coupled with projectile shape optimization techniques in order to achieve de-

sired design and performance objectives. Current ballistic fin stabilized projectiles, when fired from standard gun muzzles, are limited to a specific range. If a target is beyond the capabilities of the ballistic projectiles, powered cruise missiles must be employed. By utilizing both optimization methods and morphing wing techniques, the aerodynamic efficiency of the standard projectile can be improved, thus increasing the maximum range. The goal of this research is to optimize the range of unpowered ballistic systems by utilizing several different morphing strategies. The trade-offs between the optimal range and morphing complexity will be discussed.

1.2 Previous Work

1.2.1 Morphing Aircraft Optimization

Due to the long history of morphing aircraft research, a large volume of literature exists on the topic. The goal of this work is to couple the morphing wing strategies of aircraft to the optimization techniques of projectiles in an effort to advance the field of projectile design and trajectory optimization. As such, this section will primarily focus on the morphing aircraft research which is most applicable to morphing projectile optimization.

Rodriguez [1] compiled a comprehensive morphing aircraft technology survey summarizing various projects, concepts, and technologies of morphing aircraft to date. Out of the diverse nature of the works, a common economic motivator was identified: having a single type of morphing aircraft capable of fulfilling a variety of mission objectives and functions under many flight conditions. In other words, an

idealized morphing aircraft would reduce the inherent compromise in the aerodynamic performance between mission legs. The most common strategy for achieving multi-objective flexibility is through changes in wing geometry [2–6]. The geometry changes in the reviewed literature are most often defined by simple continuous changes in the wing span and sweep of rectangular or delta planform wings. Methods to obtain an optimum morphing wing concept is still under much investigation. A common technique is to analyze the mission objectives, derive optimum geometries for each flight condition, then decide what morphing wing design will best mimic these optimum shapes [3–6].

Crossley, et al. [2] summarized the different methods for which an individual optimized aircraft wing geometry could be attained. The associated numerical optimization techniques and concerns for each method were addressed. It was concluded that an optimum design for a aircraft flying a range of missions is best found using multi-level optimization. The optimization schemes would more effectively find a solution when each mission leg was evaluated as a subproblem to the overall top level optimization. It was also revealed that many non-closure cases existed where the optimization code failed due to a numerical issue or a discontinuous design space. Crossley found that gradient-free optimization methods are necessary for many types of aircraft optimization problems.

Ref. [5] is an illustrated example of how the success of a morphing concept can measured by comparing it to an array optimum designs. Joshi, et al. analyzed the optimum wing geometries for 11 flight conditions representing various mission segments (takeoff, cruise, dash, etc.). Each mission segment is represented by a

performance metric to be maximized or minimized to obtain "optimal" performance. For example, a takeoff mission leg indicates a minimization of the time to accelerate, a cruise mission leg indicates a maximization of range, etc. An optimum wing geometry was found for each of these 11 mission segments. Two morphing wing designs were then conceptualized and their performance was compared to the 11 optimum geometries using a spider plot as shown in Figure 1.1. The optimum

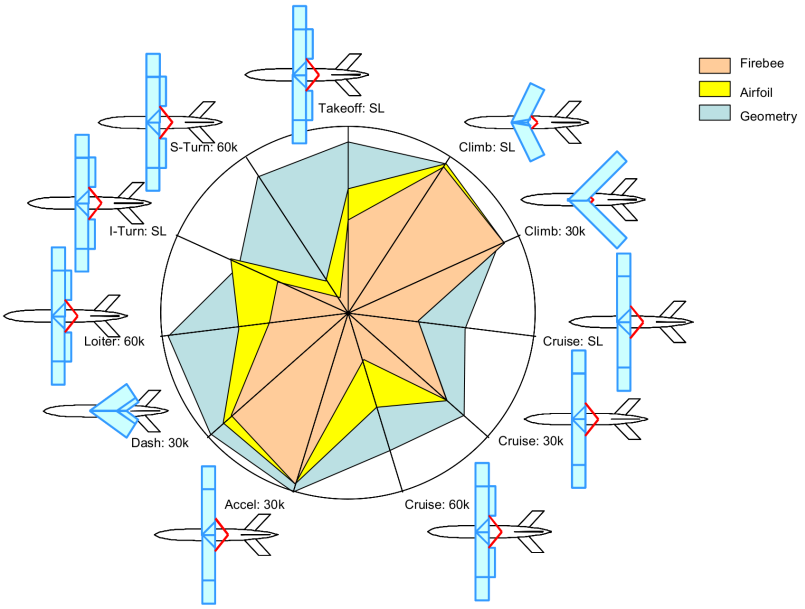

Figure 1.1: Spider plot comparing predicted performance of a fixed geometry Firebee wing, morphing airfoil Firebee wing, and morphing planform Firebee wing from Ref. [5]

geometries define the outer radius of the spider plot. The inner most shaded area on the plot is the performance of a fixed geometry wing. The plot shows that the fixed wing performs well in acceleration and climbing legs, but a compromise in performance exists at a cruise and s-turn leg. A morphing geometry and morphing

airfoil wing are also plotted as shaded areas on the diagram extending out from the center and approaching each optimum geometry to a certain degree. The plot shows that the morphing geometry wing helps alleviate the compromise inherent in the fixed geometry wing, bringing the overall performance closer to optimum for all 11 flight conditions.

As exemplified in Refs. [2–5], the main objective in optimizing morphing aircraft, aside from minimizing vehicle weight, is to optimize performance based on multiple mission legs. Takahashi, et al. [6] adapted the mission leg optimization schemes of morphing aircraft to morphing tactical cruise missiles. This adaptation was successful because a winged, tactical cruise missile is practically a small autonomous aircraft. It is designed to transport a payload to a designation while following distinct mission legs. Takahashi, et al. divided the mission into three sections: high altitude long range cruise, low altitude cruise with moderate maneuverability, and low altitude loiter. As is found for aircraft, each of these mission legs require different optimized aerodynamic performance metrics, rendering different wing designs. Ref. [6] exemplifies the main idea of this thesis: morphing wing aircraft strategies can be applied to missile or projectile optimization to increase performance.

1.2.2 Morphing Projectile Optimization

The quantity of published literature on morphing projectile design is quite limited. Most of the previous research focused a singular optimum shape rather than

one that changes shape throughout flight [7–12]. Refs. [8,10,12] implemented trajectory simulations to their optimization schemes giving them the ability to optimize trajectory characteristics, such as maximizing range. Tanil [10] explored the optimization design space of missiles using discrete fin sets rather than continuous fin geometry variables. The results showed what capabilities are possible given a particular set of fin geometries. Yang, et al. [12] took the optimization one step further and maximized the range of a guided projectile. Although the geometry variation was limited and the speeds subsonic, the addition of canard control exemplified the ability to optimize a more complex design space.

Projectile design has also been extended past single-objective optimization to incorporate multi-objective and multidisciplinary design optimization. Refs. [7,9,11] used multi-objective optimizers to maximize both performance and stability objectives concurrently. Results produced Pareto fronts of possible designs, rather than obtaining a single optimum design. This gives the user the option of weighing the trade-offs between the combination of objective functions, to find which design is best for the mission. Refs. [9, 11] successfully showed that genetic algorithms are capable of designing aerodynamic shapes that perform well in both single and multiple goal applications. Refs. [7–12] all utilized genetic algorithms to find an optimum projectile geometry. This is no surprise considering previous research in airplane design optimization found that the design spaces are susceptible to discontinuities or may be non-differentiable, rendering zero-th order methods necessary.

The shape changes and morphing capabilities as discussed in Section 1.2.1 can also be applied to projectiles. This migration to projectiles is first seen in Ref. [8],

where missile shape changes are considered for different mission legs. If a missile is launched with sufficient velocity, the flight regimes (i.e. Mach ranges and altitude ranges) it will experience over the trajectory can also benefit from shape changes, thus improving performance. This idea is what is investigated in this thesis. Intuition states that subsonic, supersonic, low-altitude, and high-altitude flight regimes would lead to different optimum projectile geometries, making optimized morphing projectiles beneficial.

1.3 Objectives and Contributions

The application of this thesis is for the development of ballistic systems that can reach beyond the 150 km range out of standard gun muzzles (155mm), or potentially electromagnetic systems. These are ranges that would normally be associated with powered cruise missiles, but with a sufficiently high lift-to-drag ratio, and adequate launch energy, unpowered systems can achieve them. Part of the analysis involves trades between morphing complexity, range, and launch energy.

The primary objective of this research is to perform a detailed investigation into optimization trade-offs. This includes an analysis of continuously varying geometry vs. discrete-point morphing concepts (i.e. two position wings, jettisonable surfaces, etc.) and an analysis of the penalties associated with such morphing. To accomplish this, the present work includes a combination of a detailed aerodynamic analysis, applicable to a wide flight envelope, coupled with studies of optimal trajectories. The aerodynamic modeling is applicable to subsonic, transonic, and

supersonic conditions, for small-finned and winged geometries. The aerodynamic modeling is integrated within optimization techniques, where best projectiles shapes can be found for any given trajectory, and then the best combination of trajectory and shape can be identified.

This work provides many contributions to the field of both morphing projectiles and projectile design optimization. Lifting body projectile aerodynamic phenomena are identified and their importance to modeling gliding trajectories are discussed. These aerodynamic phenomena may not always be included in standard military projectile aero-prediction codes. The optimization design code in this thesis provided a working example which implemented direct search and gradient based optimization methods for searching a gliding projectile design space. Most importantly, this research acts as a tool for analyzing a given baseline projectile with a particular mission profile and identifying the best morphing strategy to maximize the range. It can determine the feasibility of extending the mission profile for existing fin stabilized munitions through morphing.

Specifically for the gun muzzle energies used in the analysis, it was found that the trade-off between range and morphing complexity is clearly most beneficial for a single optimized geometry. The range of the projectile can be nearly doubled by simply adding one extra set of wings and canards to the baseline configuration. However, the additional morphing schemes analyzed in this thesis would be technologically difficult to implement and the payoff with ideal conditions is minimal at best. If transient aerodynamic effects of wing and canard morphing are taken into account it is possible that the more complex morphing schemes would no longer

provide an increase in range.

The optimum designs and explanations of the results are fully outlined in Chapter 4 and summarized in Chapter 5. The optimum geometries were found by first creating an aerodynamic prediction model using all pertinent aerodynamic theory and applicable assumptions which are outlined in Chapter 2. The aerodynamic prediction code, when coupled with a trajectory simulation program, was applied to three morphing strategies creating objective functions to be optimized for maximum range (Chapter 3).

Chapter 2

Projectile Aerodynamics

A significant effort has been devoted to developing a detailed aerodynamic model that is valid across all flight regimes, and appropriate to ballistic forms as well as those with considerable lifting area. The overall analysis of the aerodynamics is semi-empirical. Where applicable, established data sets were used to obtain aerodynamics. The majority of the emphasis has been placed on models that capture aerodynamic performance from a fundamental physics perspective, including responses not typically seen in conventional ballistic configurations. For example the vortex lift off a delta wing is included and its importance in the aerodynamic design is discussed. The theory behind the aerodynamics is presented in this section. The aerodynamic coefficients presented here are applied via MATLAB function files which are then called within the optimization code outlined in Chapter 3.

Methods for determining total projectile aerodynamic characteristics from component aerodynamics are introduced and parallel the analysis done in Ref. [13]. The category of projectile under consideration is a four-canard controlled delta wing projectile. A standard example of such a projectile is shown in Figure 2.1. The projectile consists of one set of four cruciform delta planform fins and canards. The aft end of the projectile contains a linearly tapered boattail. The aerodynamic modeling of the projectile has been subdivided into three primary parts: the body, the

wings/fins or canards, and the interference associated with the wing-body interaction. All final calculated aerodynamic coefficients are referenced to the projectile cross-sectional area S_{cs}.

Figure 2.1: Example projectile under consideration

2.1 Body Aerodynamics

The body of the projectile includes the nose, the center-body, and the boattail. For preliminary designs, the nose shapes of interest are bounded by cones and ogives [13]. Therefore, the nose is modeled as either a right circular cone or a slender secant ogive and is left as a user parameter in the code. The centerbody is a cylinder of circular cross section. The boattail is modeled as a linear tapering of the circular cross section of the center body, in other words a truncated cone with the frustum as the projectile base.

2.1.1 Body Lift

The body alone lift and drag due to lift (induced drag) is found using following expressions:

$$C_{L_{body}} = C_{N_{\alpha,body}} \alpha \cos(\alpha) \tag{2.1}$$

$$C_{D_{i,body}} = C_{N_{\alpha,body}} \alpha \sin(\alpha) \tag{2.2}$$

where, $C_{N_{\alpha,body}}$ is the gradient of the normal force coefficient with respect to α. The body alone normal force coefficient gradient values were obtained from wind tunnel tests of tangent ogive-cylinder bodies for subsonic and transonic flow conditions [14], from theoretical data sets obtained from the Royal Aeronautical Society, and from wind tunnel data through the supersonic range [15]. This data was compiled and analyzed by De Jong [16], who concluded that the data in the RAeS data sets and Refs. [14] and [15] were in close agreement. The data from Ref. [16] is presented in Table 2.1, where $C_{N_{\alpha,body}}$ can be found as a function of Mach number and body caliber. Note that these coefficients are referenced to the cross-sectional area of the cylinder center body, S_{cs}. The aerodynamic model in the present study uses a two dimensional linear interpolation and extrapolation of the data in Table 2.1 to provide a value of the body normal force gradient for the projectile of interest.

2.1.2 Body Drag

2.1.2.1 Viscous Drag

The laminar viscous drag is calculated using the Blasius solution to the boundary layer equations over a flat plate. The full derivation of the Blasius equation and its solution is presented in White [17]. White applies the Blasius solution for a laminar boundary layer to the definition of the drag coefficient and integrates over a plate of length L. This results in a viscous drag coefficient for a laminar boundary layer expressed as:

$$C_{D_{f,plate}} = \frac{1.328}{\sqrt{Re_L}} \tag{2.3}$$

Table 2.1: $C_{N_{\alpha,body}}$(in per radians) for 8, 10, 12, and 14 caliber bodies at various Mach numbers from Ref. [16]

M_∞	8 Cal. body	10 Cal. body	12 Cal. body	14 Cal. body
0.0	2.03	2.32	2.39	2.67
0.4	1.83	2.10	2.18	2.36
0.8	2.40	2.46	2.51	2.54
1.0	2.75	2.80	2.88	3.15
1.1	2.69	2.81	2.91	3.10
1.2	2.64	2.75	2.85	3.04
1.3	2.62	2.72	2.80	2.99
1.5	2.71	2.75	2.79	2.95
1.8	2.85	2.85	2.85	2.94
2.0	2.90	2.92	2.94	2.97
2.5	3.01	3.06	3.10	3.13
3.0	3.06	3.16	3.25	3.26
3.5	3.05	3.20	3.30	3.35

where Re_L is the Reynolds number with respect to flat plate length L and is defined as:

$$Re_L = \frac{\rho_\infty U_\infty L}{\mu_\infty} \tag{2.4}$$

The values for μ_∞ are found using the well known approximation resulting from a kinetic theory by Sutherland using an idealized intermolecular-force potential [17]. The final formula to solve for μ_∞ is the following:

$$\mu_\infty = \mu_s \left(\frac{T_\infty}{T_s}\right)^{\frac{3}{2}} \left(\frac{T_s + Y}{T_\infty + Y}\right) \tag{2.5}$$

where μ_s and T_s are gas property reference parameters and Y is Sutherland's constant, which is a characteristic of the gas being examined. The values for T_∞ and ρ_∞ are found as a function of altitude via the 1959 ARDC model atmosphere [18].

Both laminar and fully turbulent boundary layers are considered. The viscous drag coefficient for a fully turbulent boundary layer over a flat plate is shown by the

following equation:

$$C_{D_{f,plate}} = \frac{0.074}{Re_L^{0.2}} \tag{2.6}$$

Equation 2.6 is derived as a power-law approximation to the momentum-integral equation and is often quoted in the literature and recommended for general use [17]. The transitional Reynolds number threshold is set at 10^5. This value was taken as a conservative value for flat plate boundary layer transition as discussed in White [17]. Meaning that when $Re_L \leq 10^5$ the boundary layer is considered laminar and Equation 2.3 is used. When $Re_L > 10^5$ the boundary layer is considered completely turbulent and Equation 2.6 is used. This was done under the assumption that the projectile will not spend considerable time flying within the band of transitional Reynolds numbers.

Equations 2.3 and 2.6 were derived such that the drag coefficients are referenced to the surface of the flat plate for which viscous forces are present, while calculating the Reynolds number with respect to a flat plate length L. In the case of our projectile body, the drag coefficient is referenced to the wetted surface of the body by calculating the Reynolds number with respect to the body length. The final viscous drag coefficient of the body must be scaled in order to correctly reference the cross sectional area of the projectile as shown in Equation 2.7, as well as substituting the body length for L in Equation 2.4.

$$C_{D_{f,body}} = C_{D_{f,plate}} \left(\frac{S_{wet,body}}{S_{cs}} \right) \tag{2.7}$$

2.1.2.2 Nose Wave Drag

Wave drag is present on the projectile nose, afterbody, and fins/wings. Since wave drag is produced by pressures normal to the surface, no wave drag is present on the center-body cylindrical section of the projectile. This is precisely true only when the body is at a zero angle of attack. For the scope of this work, the assumption made for preliminary design estimates is to assume the center-body wave drag is small enough at the angles of attack experienced here to be negligible [13]. Therefore, the aerodynamic model in the present work will only include that of the nose, afterbody(boattail), and the fins/canards.

The wave drag on the nose is calculated for slender secant ogives and cones when applied to supersonic and transonic flight speed regimes. The supersonic wave drag for both the ogive and cone can be found in Figure 2.2 as a function of freestream Mach number and nose fineness ratio (fn). Figure 2.2, found in Ref. [13], serves as a more detailed extension of the values given by Stoney [19]. The supersonic cone wave drag values in Figure 2.2 is derived from a numerical solution to the Taylor-Maccoll equation. The ogive wave drag values are found using second-order calculations by the method of Van Dyke [20]. It can be seen from Figure 2.2 that for low freestream Mach numbers and/or higher nose fineness ratios (giving a M_∞ to fn ratio below 1), the wave drag for a cone is virtually the same for that of an ogive. As outlined in the latter sections of this thesis, the nose fineness ratio being analyzed in this study has a value of 4.125. The Mach numbers experienced during the trajectory simulations are generally low. The highest Mach number value is at

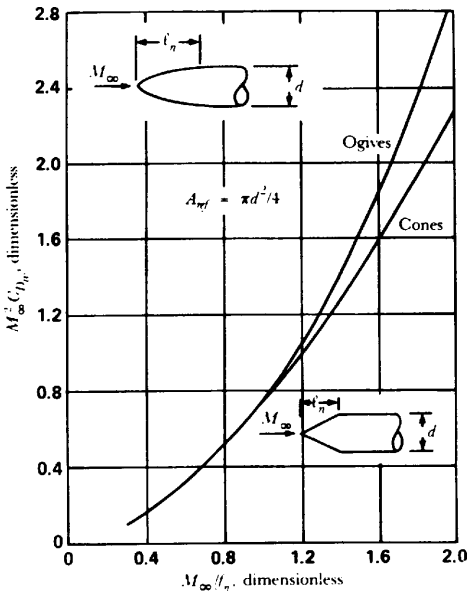

Figure 2.2: Wave drag of cones and ogives from Ref. [13]

launch conditions, which immediately starts to decrease due to the ballistic nature of the trajectory. It was seen during the investigation of the projectile trajectories in the present work that one nose shape did not provide any appreciable advantage over the other.

Transonic wave drag for a conical nose is calculated using a similarity system approach to derive a second order approximation of the slope of the drag coefficient across $M_\infty = 1$ given by:

$$\frac{dC_{D_{w,nose}}}{dM} = \left(\frac{4}{\gamma+1}\right)\left(1 - \frac{1}{2}C_{D_{w,nose}}\Big|_{M=1}\right) \tag{2.8}$$

where, $C_{D_{w,nose}}\Big|_{M=1}$ is the nose wave drag found at $M_\infty = 1$ obtained in Figure 2.2.

Equation 2.8 is derived by manipulating the pressure drag coefficient applicable for transonic flow, while making certain assumptions about the surface Mach number and keeping the first and second order terms. The complete derivation and applied assumptions can be found in Appendix C of Ref. [21]. The suggested use of this

method is discussed and compared to experimental data in Ref. [22]. Equation 2.8 is used in the aerodynamic model for freestream Mach numbers below unity.

The transonic wave drag for slender ogives is found using the values given in Figure 2.3. Here the transonic wave drag is given as a function of freestream Mach number and nose fineness ratio. Figure 2.3 was prepared in Ref. [13] as an alternate representation of the computations outlined in Ref. [23]. The underlying data represented by the curve in Figure 2.3 was split up into an interpolation table for use in the aerodynamic model.

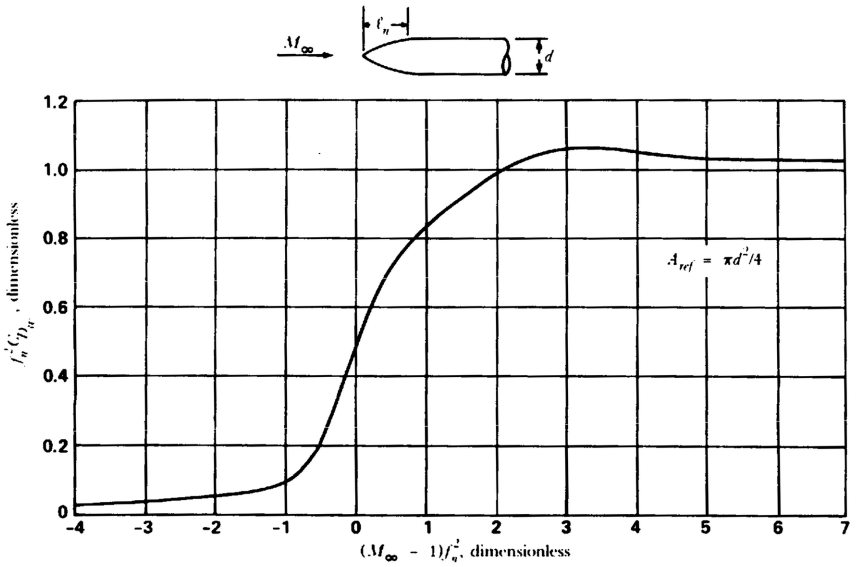

Figure 2.3: Transonic wave drag of slender ogives from Ref. [13]

2.1.2.3 Base Drag

Base drag is the result of pressure forces due to airflow separation from rearward-facing steps found at the base of the projectile. The drag is affected by the geometry of the rearward-facing step and the properties of the airflow approaching the step. The flow field present at the base can be somewhat complex when taking into ac-

count boundary layer conditions, flow separation physics, and propulsion system exhaust [13]. For the case of a preliminary design, empirical relationships and generalized curves can be used and still provide quality base drag data. The base drag coefficient is defined by the following equation:

$$C_{D_{base,nbt}} = C_{p_{base,nbt}} = \frac{p_{base} - p_\infty}{q_\infty S_{cs}} \tag{2.9}$$

The boundary layer approaching the base of the projectile is generally turbulent [13]. For the purpose of this work, the correlations for base drag coefficients will assume a fully turbulent boundary layer immediately approaching the base. For subsonic flow, Reynolds number effects will be included in the calculation of the base drag coefficients. For supersonic flow conditions, Chapman [24] shows that base pressure does not vary greatly with Reynolds number and will therefore be assumed constant in this thesis.

Subsonic base pressure coefficients were estimated using the correlations with experimental data from Ref. [25]. These correlations were split up into data points in order to create a lookup table as a function of altitude and freestream Mach number. The correlations by Brazzel [25] are shown in Figure 2.4. Brazzel only includes data for freestream pressures as low as 0.25 atmospheres. Therefore the data in Figure 2.4 needed to be extrapolated to the freestream pressures which are experienced at the altitudes of interest in the current study.

Supersonic base pressures of axisymmetric bodies are well defined from data obtained by numerous wind tunnel and flight tests. Many of which are correlated and discussed by Love [26] and Seiff et al. [27]. Love's correlation for supersonic

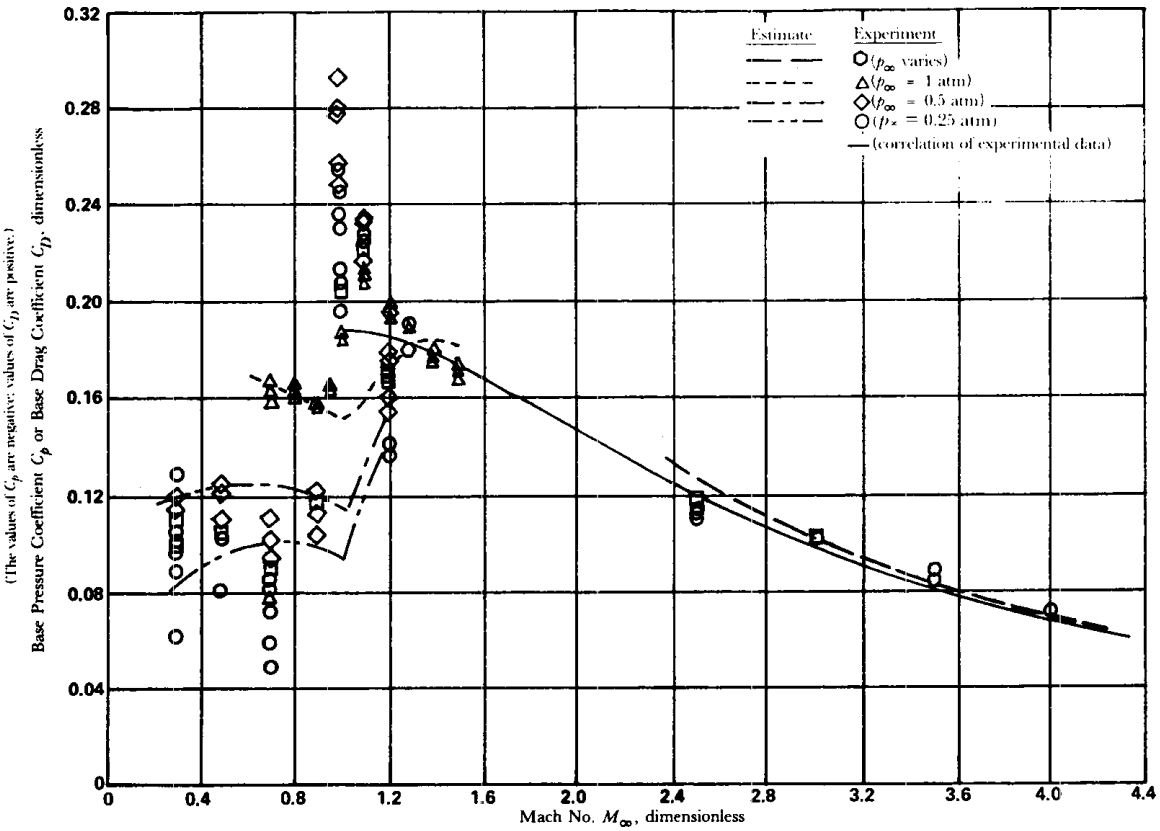

Figure 2.4: Subsonic base pressure coefficient for bodies of revolution from Ref. [25]

base pressure drag coefficient is shown by the solid line in Figure 2.5.

Love and Seiff calculated the variation of the base pressure coefficient with respect to the local Mach number immediately upstream of the base. The assumption is made that the local values of Mach number and pressure are approximately equal to the freestream values. This assumption is valid only for bodies with no boattail. The projectile geometry of interest in the current study includes a boattail afterbody. Therefore a boattail correction factor must be included to the base pressure drag coefficient. Rubin et al. [28] studied the influence of boattail geometry on supersonic base pressure. Supersonic base pressures appeared to correlate as a function of base to cylinder area ratio, $\frac{S_{base}}{S_{cs}}$. This correlation is illustrated in Figure

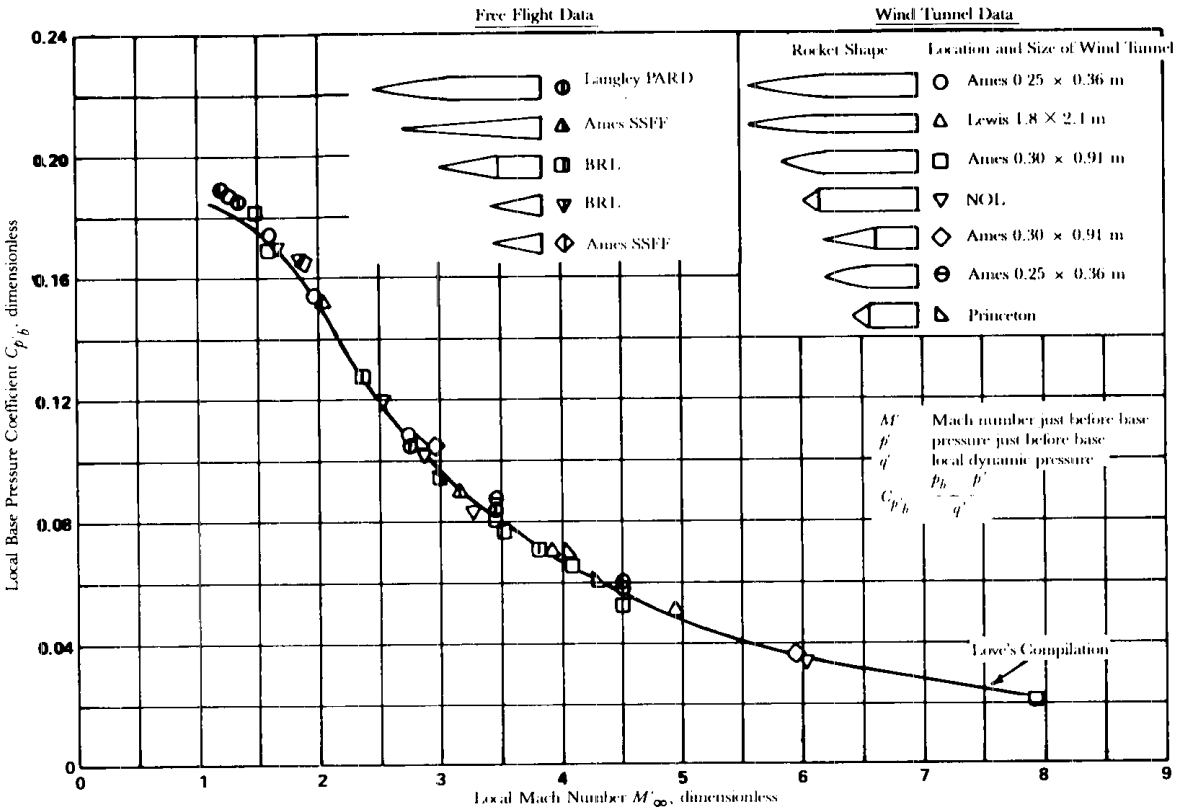

Figure 2.5: Supersonic base pressure coefficient for bodies of revolution from Ref. [27]

2.6. The effect of boattail fineness ratio also influences the supersonic base pressure. This effect is essentially neglected in Ref. [28] because the data was taken at a near constant boattail fineness ratio. A correction factor for fineness ratio is outlined in Ref. [29]. Both effects of the boattail are added to the aerodynamic model for both supersonic and subsonic conditions to produce the corrected final base drag coefficient:

$$C_{D_{base,bt}} = \left(C_{D_{base,nbt}}\right)(K_b)\left(\frac{S_{base}}{S_{cs}}\right) \tag{2.10}$$

where, $K_b = 0.5$ as approximated from Ref. [29] for the boattail geometry used in this thesis.

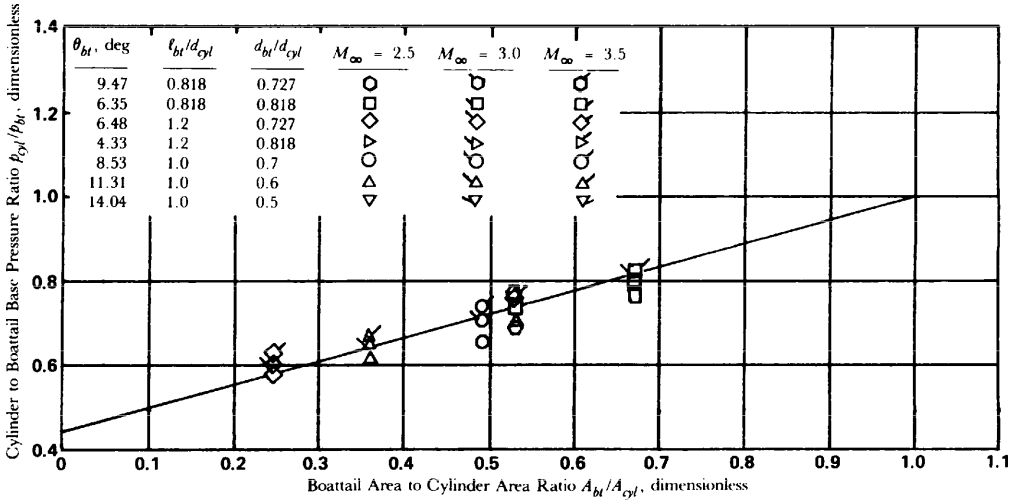

Figure 2.6: Cylinder to boattail pressure ratio as a function of base area ratio from Ref. [28]

2.2 Fin and Canard Aerodynamics

This section describes the aerodynamic modeling used for the wings/fins and canards. The wings and canards are modeled as delta-planform lifting surfaces with a symmetric double wedge cross section. Also, the delta planform is modeled as right triangles. For simplicity, the maximum thickness of the fin occurs at the midpoint of the root chord. The tip chord to root chord ratio is zero, meaning that the delta planform is not "clipped".

2.2.1 Wing and Canard Lift

Similar to the body aerodynamics, the lift and drag due to lift of the wings are calculated by taking the parallel and perpendicular components of the normal force with respect to the oncoming velocity vector (analogous to Equations 2.1 and 2.2). For standard fin-stabilized ballistic projectiles, it is usually sufficient to calculate the normal force of the fins using potential flow theory. This is due to the underlying

assumption that the angles of attack will be sufficiently small as to minimize any influence of vortex flow over the top surface of the delta wing. For cases considered in this study, given the desired high-lift projectile geometries, the wings and canards act as main lifting surfaces rather than simply to provide stability. To account for the aerodynamics at high angles of attack, it is necessary to include the influence of the vortex lift contribution as well as the potential lift.

When a delta wing is at an angle of attack, two coherent vortical structures form on the top surface of the wing. The presence of these flow structures increases the normal force experienced by the wing. The general nature of vortex flow has been understood for many years and several notable analytical methods have been established to predict the aerodynamic characteristics of leading edge separated flow [30–32]. These methods are limited to modeling specific geometries, angles of attack, and Mach numbers and may not be accurate for all the cases to be considered in this study. It was necessary to use an analytical model which is accurate for a wide range of wing geometries and angles of attack for subsonic,transonic, and supersonic flight regimes. The most appropriate method for use in this thesis is the Leading Edge Suction Analogy by Polhamus [33–36]. This method relates the flow about the spiral vortices to the potential flow about the leading edge and formulates an analogy between the leading edge suction in potential theory to that of an induced vortex flow. Comparisons of this analytical technique to experimental data for a wide range of aspect ratios and angles of attack has indicated excellent agreement [34].

The Leading Edge Suction Analogy method developed by Polhamus applies to delta wings that have no camber or twist. It assumes that the wings are thin

and have sharp leading edges such that the flow separation is fixed at the leading edge and no leading edge suction is developed. The approach also assumes that if flow reattachment occurs on the upper surface of the wing, the total lift can be calculated as the sum of a potential flow lift contribution and a vortex flow lift contribution. The following sections will summarize the derivation of the governing equations in Refs. [33–36] to calculate the potential and vortex lift contributions for subsonic,transonic, and supersonic flow.

2.2.1.1 Potential Lift

The derivation of the governing equations of the potential flow lift contribution starts off with the equation relating the lift coefficient to the normal force coefficient as a function of angle of attack. This equation is given by:

$$C_{L,\phi} = C_{N,\phi} \cos\psi \tag{2.11}$$

The normal force is determined by applying the Kutta-Joukowski theorem with respect to the velocity component parallel to the wing chord giving:

$$N = \rho \Gamma b \left(U \cos\psi\right) \tag{2.12}$$

where, b is the wingspan and Γ is the total effective circulation. The distribution of circulation for this lifting body must satisfy the boundary condition requiring that the velocity normal to the chord plane induced by the total vortex system be equal to $U \sin\psi$ at all points on the wing planform. If this condition is satisfied, the total effective circulation can be written as:

$$\Gamma = K_p \left(\frac{S_{wing} U}{2b}\right) \sin\psi \tag{2.13}$$

where, S_{wing} is the wing planform area, or simply one half the root chord length multiplied by the wing span, and K_p is a constant of proportionality. Plugging in Equation 2.13 into 2.12, then into 2.11 would render the following:

$$C_{L,\phi} = K_p \sin\psi \cos^2\psi \tag{2.14}$$

The value of K_p is derived differently for incompressible flow than it is for compressible flow. For incompressible flow it is possible to derive this constant purely as a function of aspect ratio using a suitable lifting-surface theory [33]. In this current work, K_p was found using the curves provided by Ref. [34] which was produced using the modified Multhopp lifting-surface theory [37]. For compressible flow, it is incorrect to use lifting-surface theory to derive this constant. For supersonic flow, K_p was derived by Stewart [38] using exact linearized supersonic flow theory as applied to a delta wing at an angle of attack. Stewart bases his derivation off of the Prandtl-Glauert equation:

$$\left(1 - M_\infty^2\right)\frac{\partial^2\phi}{\partial x^2} + \frac{\partial^2\phi}{\partial y^2} + \frac{\partial^2\phi}{\partial z^2} = 0 \tag{2.15}$$

This linearized velocity potential equation is important to recognize because it shows that Stewart accounts for the compressibility effects at supersonic speeds when deriving a relationship for K_p. The final result from Ref. [38] is seen as:

$$K_p = \frac{\pi A}{2E} \tag{2.16}$$

where, $A = \frac{b^2}{S_{pf}}$ is the aspect ratio of the wing. E in Equation 2.16 is the complete elliptic integral of the second kind with a modulus of:

$$\left[1 - \left(\left(M_\infty^2 - 1\right)^{\frac{1}{2}} \cot\Lambda_{LE}\right)^2\right]^{\frac{1}{2}} \tag{2.17}$$

where, Λ_{LE} is the leading edge sweep angle of the delta wing.

Now the potential lift coefficient is known for both the subsonic and supersonic flight regimes. As for the transonic region, Polhamus outlines a technique for which subsonic compressibility effects can be taken into account [35]. A Prandtl-Glauert transformation along with the Goethert rule [39] is used to relate the pressure coefficient at a given nondimensionalized point on the "real" wing to that of an equivalent incompressible flow type wing. The full derivation of this technique is found in Ref. [35]. Essentially the method uses the factor of $\sqrt{1 - M_\infty^2}$ on the subsonic values to correctly apply compressibility effects to the high subsonic or transonic flow regime.

2.2.1.2 Vortex Lift

The vortex lift contribution is found using the Leading Edge Suction Analogy by Polhamus. The most difficult aspect of calculating the vortex lift is determining the strength and shape of the spiral vortex sheet produced on the wing. The Polhamus method relates the force needed to maintain equilibrium flow over the reattached spiral vortex to that of the leading edge suction force which would occur if the flow were to be analyzed in a fully potential flow.

For an attached flow condition in a potential flow over a sharp leading edge (Figure 2.7(a)), flow ahead of the stagnation point flows toward the leading edge and accelerates around the leading edge to the top surface. The pressure needed to counter act the centrifugal force and maintain flow equilibrium is called the leading edge suction force. This is denoted by C_S in Figure 2.7. Since the leading edge

suction pressures are inversely related to the leading edge radius, the total suction force for a rounded edge (Figure 2.7(b)) is the same as that of the sharp edge. For separated flow over a sharp edge (Figure 2.7(c)), the flow ahead of the stagnation point flows forward and separates from the wing as it leaves the leading edge forming a spiral vortex sheet. Air flows over this vortex and accelerates down and reattaches on the top surface of the wing. Since the flow reattaches to the wing, the assumption Polhamus makes in his technique is that the force on the wing needed to maintain equilibrium flow over a separated spiral vortex is the same as the leading edge suction force associated with a wing in a potential flow [36]. For a sharp leading edge condition, the force as indicated in Figure 2.7(c) will act normal to the top surface of the wing.

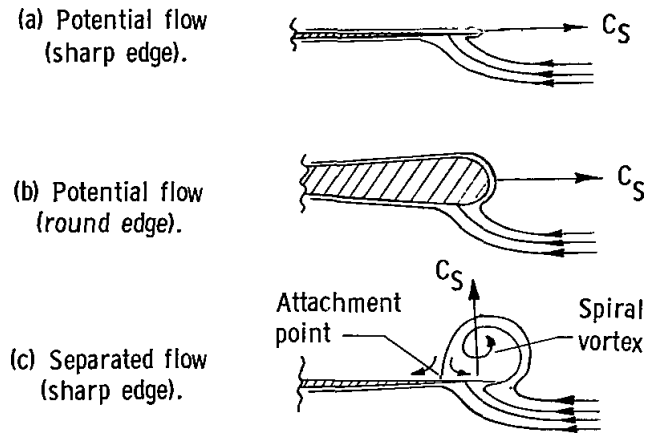

Figure 2.7: Leading edge flow conditions from Ref. [36]

The vortex lift coefficient is found using a similar derivation to that of the potential flow case in Equation 2.11 through Equation 2.14. Yet, for the vortex lift case,the Kutta-Joukowski theorem is applied using the velocity components normal to the wing chord plane while also taking into account an effective downwash velocity

induced from the vortex system. This analysis gives an equation for the vortex lift contribution given by:

$$C_{L,v} = K_v \sin^2 \psi \cos \psi \tag{2.18}$$

where,

$$K_v = \frac{\partial C_S}{\partial \psi^2} \tag{2.19}$$

Similar to K_p, the constant K_v is derived differently for compressible flow than it is for incompressible flow. For incompressible flow, K_v can be found using the same lifting-surface theory used for the potential flow case while keeping in mind that the force is now perpendicular to the leading edge. For compressible flow, the proportionality constant for vortex flow can be based on a derivation by Brown [40]. Brown's method starts by using the supersonic linearized potential function of a line of doublets. The flow about a delta wing is obtained by the surface distribution of the doublet flows. When applying the correct boundary conditions, the coefficient is found to be a function of the ratio of the apex angle of the wing to the Mach angle. This effectively maintains the influence of compressibility on the lift of the wing. The final outcome of the derivation of K_v in Ref. [40] is given by the following expression:

$$K_v = \frac{\pi \left[\left(16 - (A\beta)^2 \right) (A^2 + 16) \right]^{\frac{1}{2}}}{16E} \tag{2.20}$$

where, $\beta = \sqrt{M_\infty^2 - 1}$.

Now that both the potential lift and vortex lift contributions are derived, the total lift of the delta wing can be written as the sum of the two contributions:

$$C_{L_{wing}} = C_{L,v} + C_{L,\phi} = K_p \sin \psi \cos^2 \psi + K_v \sin^2 \psi \cos \psi \tag{2.21}$$

With the lift coefficient known, the induced drag can be calculated using the following expression:

$$C_{D_{i,wing}} = C_{L_{wing}} \tan \psi \tag{2.22}$$

2.2.1.3 Leading Edge Suction Analogy Limits and Supersonic Leading Edge Considerations

The most important assumption being made in the Leading Edge Suction Analogy method is that the vortical structure successfully re-attaches to the top surface of the wing. This assumption is valid unless vortex breakdown starts to occur. All wings will eventually reach an angle of attack where vortex breakdown starts to occur and a Helmholtz type of flow exists [33]. This effect will reduce the total effective lift on the wing and render the Polhamus method inaccurate. This type of vortex breakdown is expected to be greatest on a wing with high aspect ratio. For extremely low aspect ratio wings, vortex contact or vortex asymmetry can occur and also affect flow re-attachment and reduce lift. Figure 2.8 summarizes the cases for which vortex breakdown and vortex asymmetry are expected to occur. The figure is presented showing boundaries placed on the angle of attack and aspect ratio of the wing below which complete vortex re-attachment occurs. Within these boundaries the leading edge suction analogy will provide an accurate estimate of the vortex lift.

Another important assumption for the Leading Edge Suction method is that of a subsonic leading edge. In order to discuss the situation of a supersonic leading edge, refer to the scenario in Figure 2.9. Here the variation of K_p and K_v is shown

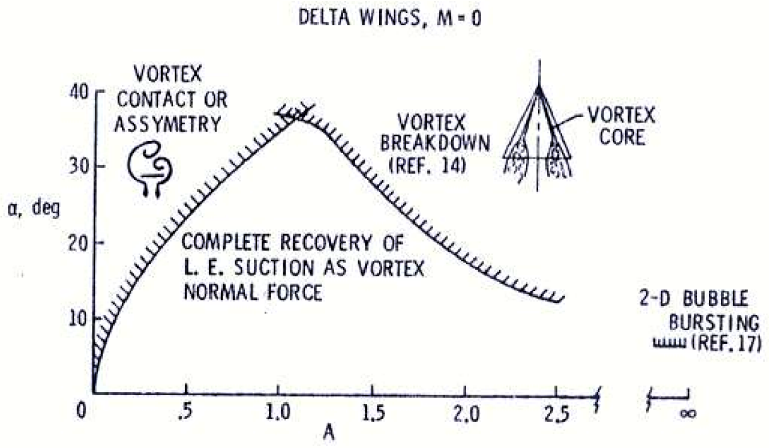

Figure 2.8: Leading Edge Suction Analogy limits from Ref. [33]

as a function of Mach number for a delta wing of aspect ratio 1, which corresponds to a leading edge sweep angle of 76 degrees. It can be seen that the variation of K_v decreases rapidly as it passes sonic flight conditions. The value approaches zero as a flight Mach number is reached for which the Mach cone coincides with the wing leading edge. This is due to the forward shift of the lower surface stagnation point with increasing Mach number. The lower stagnation point reaches the leading edge at a sonic leading edge condition, meaning no flow reversal occurs at the edge. The weakening vortex with increasing Mach number is illustrated in the sketches of Figure 2.9.

For supersonic leading edge conditions, only a potential flow solution is needed to calculate the lift and induced drag coefficients of the delta wing. In order to know when the leading edge is outside of the Mach cone, one can start by using the equation for the semi-vertex angle of a Mach cone [41] given by:

$$\epsilon = \sin^{-1}\left(\frac{1}{M_\infty}\right) \tag{2.23}$$

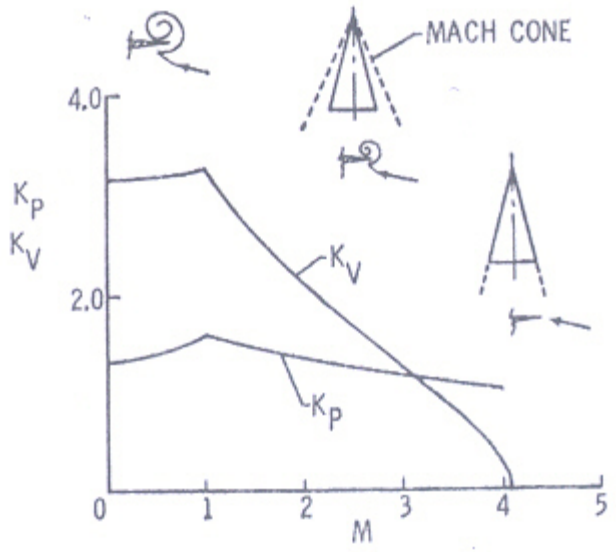

Figure 2.9: Weakening vortex lift as a function of Mach number from Ref. [33]

Supersonic leading edge conditions occur when the semi-vertex angle of the wing is greater than that of the corresponding Mach cone at flight conditions. Solve Equation 2.23 for M_∞ and then substituting the equivalent semi-vertex angle of the wing in for ϵ gives:

$$M_{sonic} = M_\infty = \frac{1}{\sin\left(\frac{\pi}{2} - \Lambda_{LE}\right)} \tag{2.24}$$

Equation 2.24 represents the Mach number which produces sonic leading edge conditions. It can be seen as the limit on the flight Mach number above which supersonic leading edge conditions exist for a given wing sweep angle.

When the wings or canards are at a flight Mach number greater than sonic conditions, it is necessary to now calculate the lift and drag coefficients using linearized supersonic flow theory. Linearized flow theory has been found to be an accurate way of predicting supersonic normal force coefficients of thin profile delta wings [13, 16, 41, 42]. Starting with the linearized potential flow equation for planar

flow given by,

$$(1 - M_\infty)\frac{\partial^2 \phi}{\partial x^2} + \frac{\partial^2 \phi}{\partial y^2} = 0 \tag{2.25}$$

the well known wavy wall problem can be solved to obtain a solution for the two dimensional velocities and pressure coefficient along the wall. Once the pressure coefficient along the wall is known, it can be applied to the case of a thin airfoil. Integrating along the top and bottom surface of the airfoil, the normal force coefficient gradient is found to be:

$$C_{N_\psi} = \frac{4}{\sqrt{M_\infty^2 - 1}} \tag{2.26}$$

The same result can also be obtained using the shock-expansion method as applied to supersonic thin airfoils. Full derivations of Equation 2.26 using each method can be found in Ref. [41]. Once the normal force gradient is known, Equations 2.1 and 2.2 can be applied to the wing as shown:

$$C_{L_{wing,ssle}} = C_{N_\psi} \psi \cos(\psi) \tag{2.27}$$

$$C_{D_{i,wing,ssle}} = C_{N_\psi} \psi \sin(\psi) \tag{2.28}$$

Note that the coefficients used in Equations 2.21, 2.22, 2.27, and 2.28 are based on the wing planform area S_{pf} and must be transfered to reference the projectile cross sectional area S_{cs} in order to stay consistent with the rest of the aerodynamic modeling. To do so, the following simple transformation was used:

$$\begin{aligned} C_{L_{wing,cs}} &= C_{L_{wing,pf}} \left(\frac{S_{pf}}{S_{cs}}\right) \\ C_{D_{i,wing,cs}} &= C_{D_{i,wing,pf}} \left(\frac{S_{pf}}{S_{cs}}\right) \end{aligned} \tag{2.29}$$

2.2.2 Wing and Canard Drag

2.2.2.1 Wave Drag of Fins and Canards

The wings and canards are modeled as delta-planform lifting surfaces with a symmetric double wedge cross section. The wave drag for such wings is strongly influenced by the thickness to chord ratio, sectional shape, and sweep angle. Figure 2.10 presents the theoretical supersonic wave drag coefficient for delta planform wings of double wedge cross section for different values of $\left(A \tan \Lambda_{\frac{1}{2}}\right)$. $\Lambda_{\frac{1}{2}}$ is defined in the figure as the complementary angle to the wings semi-vertex angle at mid-chord. The curves presented in Figure 2.10 were found using an analysis based on supersonic thin-airfoil theory and applying an assumption of small disturbances, thus was derived using the linearized equation for the velocity potential in three dimensions. The distribution of pressure over the wings is obtained by applying semi-infinite line sources and sinks as boundary conditions to a superposition of wedge-type solutions [43, 44].

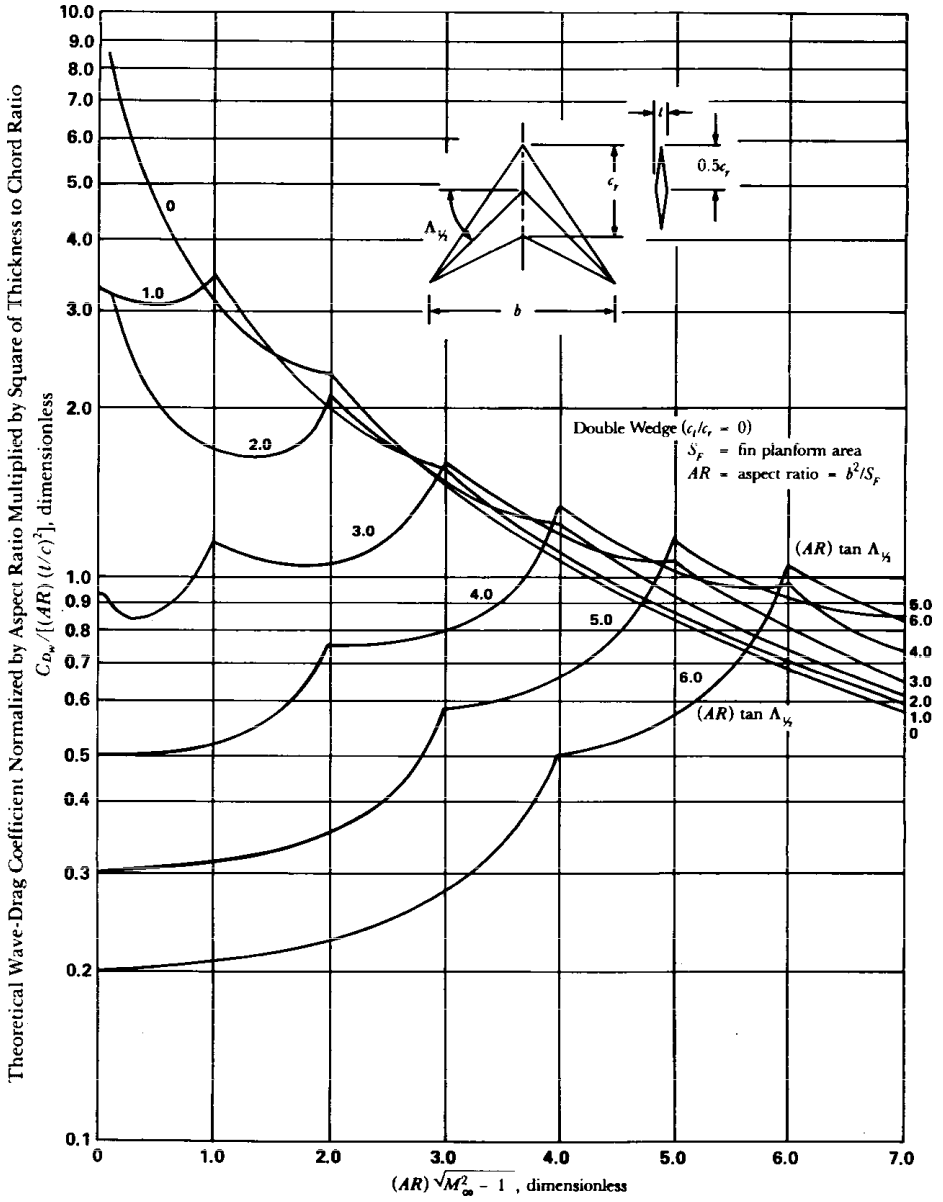

Figure 2.10: Wing supersonic wave drag coefficient from Ref. [13], adapted from Ref. [43] and Ref. [44]

In order to use Figure 2.10 for the right triangle delta planform of interest, consider the following proof:

$$\begin{aligned}
(A)\tan\left(\Lambda_{\frac{1}{2}}\right) &= g \\
\left(\frac{b^2}{S_{wing}}\right)\tan\left(\frac{\pi}{2}-\Lambda_{LE}\right) &= g \\
\left(\frac{b^2}{\frac{1}{2}bc}\right)\tan\left(\frac{\pi}{2}-\arctan\left(\frac{\frac{b}{2}}{\frac{c}{2}}\right)\right) &= g \\
\left(\frac{b}{c}\right)\tan\left(\frac{\pi}{2}-\arctan\left(\frac{\frac{b}{2}}{\frac{c}{2}}\right)\right) &= \frac{g}{2} \\
\tan\left(\frac{\pi}{2}-\arctan\left(\frac{b}{c}\right)\right) &= \left(\frac{g}{2}\frac{c}{b}\right) \\
\arctan\left(\frac{g}{2}\frac{c}{b}\right)+\arctan\left(\frac{b}{c}\right) &= \frac{\pi}{2}
\end{aligned}$$

The above is a true trigonometric identity if $g = 2$

$$\Rightarrow (A)\tan\left(\Lambda_{\frac{1}{2}}\right) = 2 \qquad (2.30)$$

Equation 2.30 shows that for right triangle delta wing planforms, only the curve where $A\tan\Lambda_{\frac{1}{2}} = 2$ is to be used. One important thing to mention about this curve is the cusp found at an x-axis value of 2. With some mathematical manipulation along with Equation 2.30 and Equation 2.24, it can be proved that this point is representative of the sonic leading edge condition. Therefore any point on the curve to the right of $A\sqrt{M_\infty^2 - 1} = 2$ gives the wave drag for a wing with supersonic leading edges. The data from Figure 2.10 was segmented into discrete data points to be used as a data table for which linear interpolated values of supersonic wing wave drag coefficients could be found. As was done in previous sections (i.e. Equation 2.29), the values in Figure 2.10 are coefficients with respect to the wing planform reference area and must be converted to the projectile cross sectional area.

The transonic wave drag coefficient for delta wings can be found using Figure 2.11. The transonic wave drag is highly dependent on the thickness to chord ratio of the wing. For the thickness to chord ratios used in this study, it is found that the transonic wave drag was vanishingly small for Mach numbers less than unity. Therefore, the wave drag is only modeled using Figure 2.10 for flight Mach numbers of unity and above.

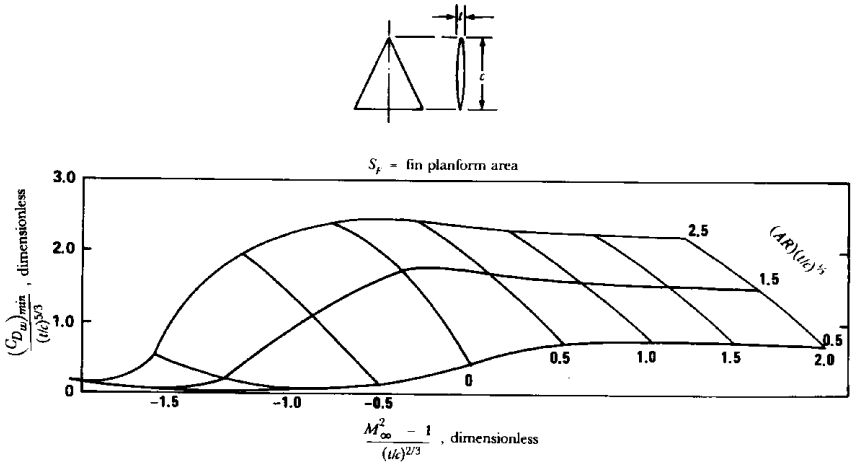

Figure 2.11: Transonic delta wing wave drag from Ref. [13]

2.2.2.2 Fin/Canard Viscous Drag

The viscous drag on the fins and canards are modeled using the same approach as the body. Yet, now the wetted surface of the wings will be used in Equation 2.7, rather than the wetted surface of the body. Also, the Reynolds number will now be calculated using the mean chord length as the length parameter L in Equation 2.4.

2.3 Wing-Body Influence Factors

When fins or canards are attached to a body, interference effects between the components increase the normal force over that of the wings or body if they were isolated from one another. This interference effect can be split into two categories: the increase in normal force of the wing due to the presence of the body and the increase in normal force of the body due to the presence of the wings. The increase of the normal force of the wings can be attributed to the upwash of the body upstream of the wing, the reflection of the upwash off the body, and the reflection of wing tip disturbances [45]. The increase in normal force of the body due to the wings is produced by the lifting pressure distribution of the wing carrying over to the body [13].

These effects can be integrated into the aerodynamic model by use of influence coefficients. The influence coefficients are defined by the following:

$$K_{F(b)} = \frac{C_{N_{\psi,wing-comb}}}{C_{N_{\psi,wing}}}$$
$$K_{B(f)} = \frac{C_{N_{\psi,body-comb}}}{C_{N_{\psi,wing}}} \tag{2.31}$$

where, $C_{N_{\psi,wing}}$ is the normal force gradient of an isolated wing, $C_{N_{\psi,wing-comb}}$ is the normal force gradient of a wing in the presence of a body, and $C_{N_{\psi,body-comb}}$ is the normal force gradient produced by the body in the presence of a wing. Note that all the normal force coefficients in Equation 2.31 are taken with respect to the wing planform reference area S_{pf}.

The values of $K_{F(b)}$ and $K_{B(f)}$ for freestream Mach numbers less than unity can be found using slender-body theory as described by Pitts, et al. [46]. Based

on the load distribution, slender-body theory gives the following expressions for the influence coefficients as a function of the wing span and body diameter:

$$K_{F(b)} = \left(\frac{\frac{2}{\pi}}{\left(1-\frac{d}{b}\right)^2}\right)\left\langle\left(1+\frac{d^4}{b^4}\right)\left\{\frac{1}{2}\tan^{-1}\left[\frac{1}{2}\left(\frac{b}{\frac{d}{2}}-\frac{d}{b}\right)\right]+\frac{\pi}{4}\right\}\right.$$
$$\left.-\frac{d^2}{b^2}\left[\left(\frac{b}{d}-\frac{d}{b}\right)+2\tan^{-1}\left(\frac{d}{b}\right)\right]\right\rangle \quad (2.32)$$

$$K_{B(f)} = \left(1+\frac{d}{b}\right)^2 - K_{F(b)} \quad (2.33)$$

The underlying assumptions in slender-body theory would normally render Equations 2.32 and 2.33 inapplicable for modeling wings of high aspect ratio. Yet, Pitts has shown that when compared to an "upwash theory", both give similar results for high and low aspect ratio wings, with the upwash theory values being slightly greater in all instances. The higher values are due to the fact that the upwash theory does not take into account the loss of lift due to interaction between the wing and the body. Therefore, the slender-body theory values can be used for all wing-body combinations [46].

For freestream Mach numbers greater than unity, wing leading edge sweep angle and Mach number become important parameters to include in determining the values of $K_{F(b)}$ and $K_{B(f)}$. The method utilized here was developed by Morikawa [45]. This method is also based on slender-body theory and uses a total influence factor K_T simply defined as:

$$K_T = K_{B(f)} + K_{F(b)} \quad (2.34)$$

The values for K_T are summarized as a function of $\left(\frac{d}{b}\right)$ by the curves presented in

Figure 2.12. Each curve is plotted for a different value of the parameter a_t given by:

$$a_t = \beta \cot(\Lambda_{LE}) \tag{2.35}$$

where, $0 \leq a_t \leq \infty$. All the values in Figure 2.34 were segmented into data tables to be linearly interpolated within the aerodynamic model. The subsonic and supersonic values of the influence coefficients are applied strictly to the potential contribution of the normal force gradient coefficients for the wings and canards.

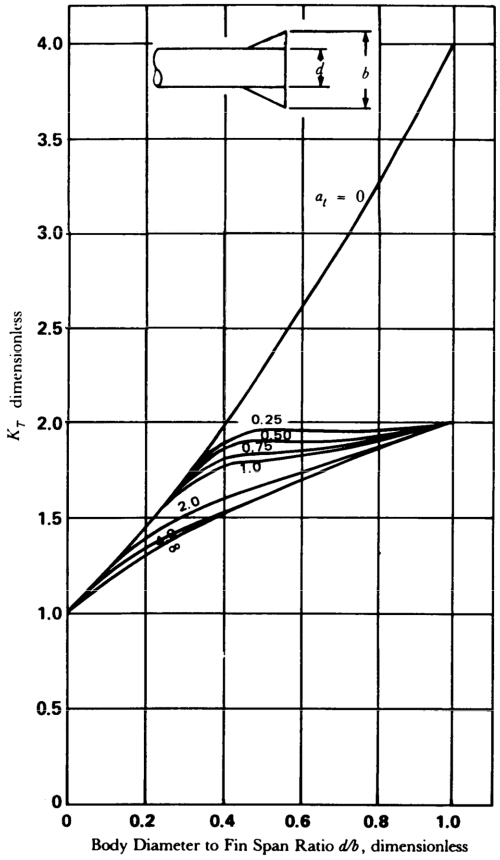

Figure 2.12: Total wing-body combination influence factors from Ref. [45]

Wing-body aerodynamic interference is not the only interaction which occurs on canard controlled finned projectiles. Fin-fin and fin-canard interactions also occur. Fin-fin interactions become important when the spacing between two adjacent

fins become small. At supersonic speeds, the shock waves produced by the leading edge of each fin can impinge on the adjacent fins. This creates considerable interference effects. Further detail on theoretical and experimental methods which can be used to approximate this effect is available in Ref. [13]. The projectiles modeled in the current work contain 4 cruciform canards and fins and therefore assume the fin-fin effects to be negligible.

Fin-canard interactions occur when the canards are positioned close enough to the leading edge of the fins that they alter the oncoming flow field. This interaction can often result in increased maximum lift and decreased trim drag [47]. The use of canards to improve the performance of the projectile has been investigated by numerous experimental and computational studies. These studies are listed in detail in Ref. [47]. It is assumed that the fin and canard configurations studied in this thesis are isolated enough to neglect any fin-canard interference.

2.4 Center of Pressure and Static Stability

The usual aerodynamic design goal when developing a projectile is to select a configuration which can achieve the desired mission objectives while flying in stable flight throughout the entire altitude-velocity flight envelope. Therefore calculating projectile stability derivatives is important to include in this study. For the projectile geometries studied in this thesis, the sole constraint on all final optimized geometries is that of static stability. A projectile is considered statically stable if a small disturbance from equilibrium sets up forces that tend to restore the projectile back to equilibrium. The measure of a projectiles stability is achieved by calculating the

moments about its center of gravity. This section will describe the methods used to calculate the stability of the projectiles.

The optimization scenarios of interest require the projectile to fly trajectories at various angles of attack. Therefore the main stability derivatives of importance are the pitching moment coefficient and the pitching moment coefficient gradient at different angles of attack. Side slip angles are assumed to be zero throughout the entire trajectory and roll effects are neglected. The pitching moment coefficient can be expressed as:

$$C_m = C_N \left(X_{cp} - X_{cg} \right) \tag{2.36}$$

where, C_N is the total normal force of the projectile. It is the sum of the contributions from the body, wings, and canards. X_{cp} is the axial distance from the base of the projectile to the center of pressure of the projectile. X_{cg} is the distance from the base to the center of gravity of the projectile. C_m is defined such that a pitch of the nose upward produces a positive value.

The value of X_{cg} was either calculated using the assumption of constant density throughout the projectile or taken as user input in the simulation. The center of gravity is measured as the distance in calibers from the base of the body. The value of X_{cp} is calculated as a weighed sum of the distances to the center of pressure for individual components of the projectile given by:

$$X_{cp} = \frac{X_{cp_{body}} C_{N_{body}} + X_{cp_{wing}} C_{N_{wing}} + X_{cp_{canard}} C_{N_{canard}}}{C_N} \tag{2.37}$$

Both the body and delta wing/canard center of pressure locations are found in tables presented by De Jong [16]. The body alone center of pressure locations were

obtained from wind tunnel tests of tangent ogive-cylinder bodies for subsonic and transonic flow conditions [14], from theoretical data sets obtained from the Royal Aeronautical Society, and from wind tunnel data through the supersonic range [15]. This data was compiled and analyzed by De Jong [16], who concluded that the data in the RAeS data sets and Refs. [14] and [15] were in close agreement. The data from Ref. [16] is presented in Table 2.2, where $X_{cp_{body}}$ can be found as a function of Mach number and body caliber. These values are measured in calibers from the base of the body and are used in the aerodynamic model via a linear interpolation between Mach number and body caliber.

The delta wing center of pressure locations are found in tables presented by Ref. [16]. These values are derived from the work of Pitts [46] using slender-body theory. Tables 2.3, 2.4, and 2.5, give $X_{cp_{wing}}$ as a function of Mach number, leading edge sweep angle, and body diameter to wingspan ratio. To find values for $X_{cp_{wing}}$ in the aerodynamic model, a two dimensional linear interpolation was used for different Mach numbers and leading edge sweep angles. To interpolate between different body diameters to wing span ratios, a semi-logarithmic interpolation must be taken with the $X_{cp_{wing}}$ value on the log base 10 axis, and $\frac{d}{b}$ on the linear axis [16].

The pitching moment gradient coefficient can be derived simply by using a central finite differencing scheme applied to Equation 2.36 around some body angle of attack as shown by the following equation:

$$C_{m_\alpha} = \frac{(C_m|_{\alpha+\Delta\alpha} - C_m|_{\alpha-\Delta\alpha})}{2\Delta\alpha} \tag{2.38}$$

where, $\Delta\alpha$ is some very small increment in angle of attack.

Equations 2.36 and 2.38 provide valuable information about a projectile's stability characteristics for a given geometry at a given angle of attack. If the value of C_m is zero, the projectile is at trimmed conditions. For static stability, the value of C_{m_α} must be less than zero.

Table 2.2: $X_{cp_{body}}$ for 8, 10, 12, and 14 caliber bodies at various Mach numbers (measured in calibers from base) from Ref. [16]

M_∞	8 Cal. body	10 Cal. body	12 Cal. body	14 Cal. body
0.0	5.50	6.53	8.21	9.45
0.4	5.87	7.15	8.75	10.2
0.8	5.57	7.00	8.62	10.2
1.0	4.95	6.45	7.83	9.18
1.1	5.18	6.85	8.06	9.24
1.2	5.48	7.14	8.55	9.8
1.3	5.65	7.31	8.88	10.4
1.5	5.85	7.47	9.26	10.94
1.8	5.63	7.48	9.40	11.33
2.0	5.44	7.39	9.30	11.35
2.5	5.17	7.12	9.08	11.05
3.0	5.05	6.95	8.87	10.75
3.5	5.01	6.82	8.70	10.60

Table 2.3: $X_{cp_{wing}}$ for $\frac{d}{b} = 0.4$ at various Mach numbers and leading edge sweep angles (measured in calibers from base) from Ref. [16]

M_∞	$\Lambda_{LE} = 80°$	$\Lambda_{LE} = 75°$	$\Lambda_{LE} = 70°$	$\Lambda_{LE} = 65°$
0.0	1.61	1.11	0.85	0.69
0.4	1.55	1.06	0.80	0.65
0.8	1.42	0.93	0.69	0.54
1.0	1.42	0.93	0.69	0.54
1.1	1.42	0.93	0.69	0.54
1.2	1.42	0.93	0.69	0.54
1.3	1.42	0.93	0.69	0.54
1.5	1.42	0.93	0.69	0.54
1.8	1.42	0.93	0.69	0.54
2.0	1.42	0.93	0.69	0.54
2.5	1.42	0.93	0.69	0.54
3.0	1.42	0.93	0.69	0.54
3.5	1.42	0.93	0.69	0.54

Table 2.4: $X_{cp_{wing}}$ for $\frac{d}{b} = 0.5$ at various Mach numbers and leading edge sweep angles (measured in calibers from base) from Ref. [16]

M_∞	$\Lambda_{LE} = 80°$	$\Lambda_{LE} = 75°$	$\Lambda_{LE} = 70°$	$\Lambda_{LE} = 65°$
0.0	1.07	0.74	0.57	0.46
0.4	1.04	0.71	0.54	0.43
0.8	0.95	0.62	0.46	0.36
1.0	0.95	0.62	0.46	0.36
1.1	0.95	0.62	0.46	0.36
1.2	0.95	0.62	0.46	0.36
1.3	0.95	0.62	0.46	0.36
1.5	0.95	0.62	0.46	0.36
1.8	0.95	0.62	0.46	0.36
2.0	0.95	0.62	0.46	0.36
2.5	0.95	0.62	0.46	0.36
3.0	0.95	0.62	0.46	0.36
3.5	0.95	0.62	0.46	0.36

Table 2.5: $X_{cp_{wing}}$ for $\frac{d}{b} = 0.6$ at various Mach numbers and leading edge sweep angles (measured in calibers from base) from Ref. [16]

M_∞	$\Lambda_{LE} = 80°$	$\Lambda_{LE} = 75°$	$\Lambda_{LE} = 70°$	$\Lambda_{LE} = 65°$
0.0	0.71	0.49	0.38	0.31
0.4	0.69	0.47	0.36	0.29
0.8	0.61	0.41	0.30	0.24
1.0	0.61	0.41	0.30	0.24
1.1	0.61	0.41	0.30	0.24
1.2	0.61	0.41	0.30	0.24
1.3	0.61	0.41	0.30	0.24
1.5	0.61	0.41	0.30	0.24
1.8	0.61	0.41	0.30	0.24
2.0	0.61	0.41	0.30	0.24
2.5	0.61	0.41	0.30	0.24
3.0	0.61	0.41	0.30	0.24
3.5	0.61	0.41	0.30	0.24

2.5 Aerodynamic Modeling Comparison

Results from the aeroprediction code in this thesis have been compared to three other standard missile aeroprediction codes. This was done in order to ensure that the aerodynamic modeling outlined in the sections of Chapter 2 accurately predicts projectile aerodynamics. Overall, the aerodynamics and stability characteristics predicted by the present work appear to be in agreement with the other codes when held to the standards of preliminary design.

The program PRODAS (Projectile Rocket Ordnance Design and Analysis System) was used to generate the data of the three aeroprediction codes used in the comparison. PRODAS is a semi-empirical aeroballistics software package which provides performance characteristics for both spin stabilized and fin stabilized projectiles. PRODAS not only uses its own aeroprediction code (FINNER), but also

interfaces with other standard aeroprediction codes to provide aerodynamic data. The two interfaced codes used for comparison here were Missile DATCOM and the Naval Surface Warfare Center Dahlgren Division Aeroprediction 98 (NSWC-AP98). Missile DATCOM is a semi-empirical missile aeroprediction developed for and widely used by the United States Air Force. NSWC-AP98 is also a semi-empirical missile aeroprediction code which was developed by the United States Navy.

PRODAS, DATCOM, NSWC-AP98 have significantly different user interfaces and projectile geometry definitions. In order for PRODAS to use a single GUI and projectile geometry to predict aerodynamics using all three codes, different assumptions to the projectile geometry must me made at the interface to each of the external codes (DATCOM and NSWC AP-98). These assumptions will account for some of the differences in the results shown in the comparisons. Each of the three codes also make their own set of aerodynamic assumptions and use different algorithms for parsing separate sets of empirical projectile aerodynamic data. In lieu of all these differences, it would not be possible to provide succinct quantitative comparisons between the aerodynamic predictions. Determining the reasons for the errors between each of these aero-prediction codes would be impossible. Therefore, the following section will focus on determining if the trends in the aerodynamic coefficients between the codes are characteristically similar for a range of geometries and conditions.

Five different geometries of varying wing and canard aspect ratios were used to generate data for the comparison. Configuration 1 is identical to the "low drag configuration" which is used for all pre-apogee model simulations (see Chapter 3).

The wing geometric parameters for Configurations 2-5 vary such that the wing aspect ratio increases for each configuration. Wing aspect ratios of 0.22, 0.5, 2, and 7 were used for Configurations 2-5 respectively. This will ensure that the aerodynamic predictions were tested for accuracy over the range of aspect ratios of interest in the optimization. The canard geometric parameters for Configurations 2-5 vary such that both statically stable and unstable conditions were investigated. This will ensure that the static stability constraint was accurately modeled for the projectiles. A complete list of geometric parameters used in the comparisons is found in Table 2.6. The geometry outlined in Table 2.6 was input into PRODAS, where the FINNER, DATCOM, and NSWC aerodynamic data was generated for each configuration. Comparisons between the aerodynamic and stability coefficients of zero-lift drag, normal force, and pitching moment gradient were investigated.

Table 2.6: Projectile geometry used for aerodynamic and stability coefficient comparison

Geometric parameter	Configuration 1	Configuration 2	Configuration 3	Configuration 4	Configuration 5
Total length (mm)	970	970	970	970	970
Body diameter (mm)	80	80	80	80	80
Nose length (mm)	330	330	330	330	330
Boattail length (mm)	200	200	200	200	200
Boattail diameter (mm)	50	50	50	50	50
Wing root chord (mm)	190	640	500	310	200
Wing span (mm)	190	150	205	390	780
Wing aspect ratio	1.157	0.22	0.5	2	7
Canard root chord (mm)	60	200	200	120	100
Canard span (mm)	82	150	130	200	430
Canard aspect ratio	2.25	1.02	0.82	2.85	8.12
Wing mid-chord thickness (mm)	5	5	5	5	5
Canard mid-chord thickness (mm)	5	5	5	5	5
Number of wings	4 (cruciform)	4 (cruciform)	4 (cruciform)	4 (cruciform)	4 (cruciform)
Number of canards	4 (cruciform)	4 (cruciform)	4 (cruciform)	4 (cruciform)	4 (cruciform)

The relationship between zero-lift drag coefficient and freestream Mach number at sea level conditions for Configurations 1-5 can be found in Figure 2.13 through Figure 2.17. The curves produced by the aeroprediction code in the present work follow reasonably close to curves produced by the other three aeroprediction codes for Configurations 1-5. The minor differences between the zero-lift drag values are likely to be caused by one or more subtle assumptions made between the different aeroprediction codes. The biggest discrepancy in zero-lift drag coefficient is found in the supersonic Mach range in Figure 2.17. Configuration 5 has such high aspect ratio wings that shortly after sonic flight conditions, the wing leading edges become supersonic. This means that the differences in the trends after Mach 1 are likely due to different theories or assumptions made on how to calculate the supersonic leading edge wave drag on the wings and canards. Overall, the trends of the curves and the range of zero-lift drag values are all acceptable for a preliminary design analysis.

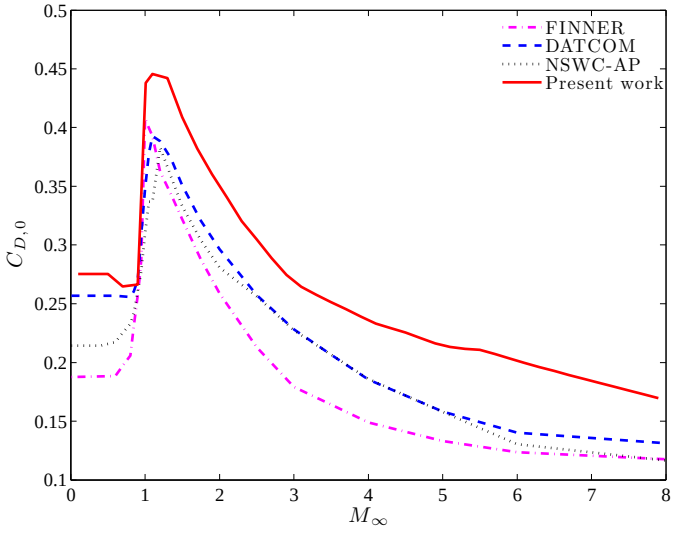

Figure 2.13: Zero-lift drag as a function of freestream Mach number for Configuration 1

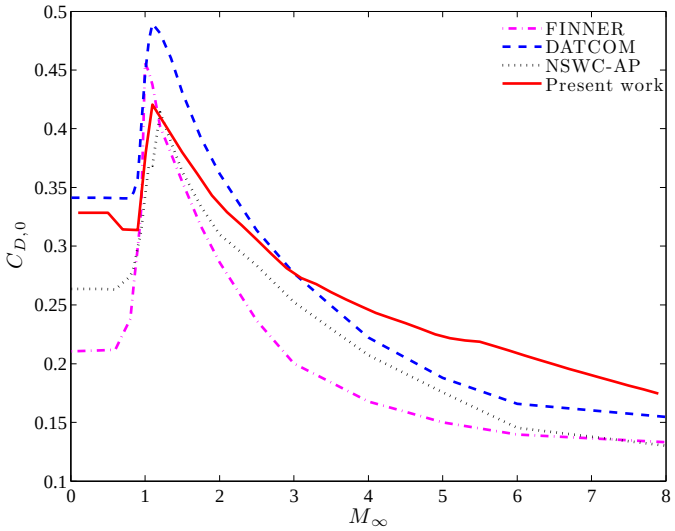

Figure 2.14: Zero-lift drag as a function of freestream Mach number for Configuration 2

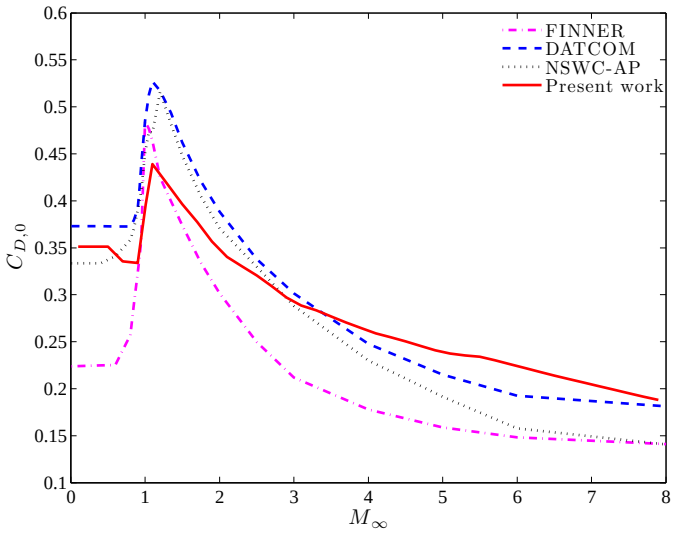

Figure 2.15: Zero-lift drag as a function of freestream Mach number for Configuration 3

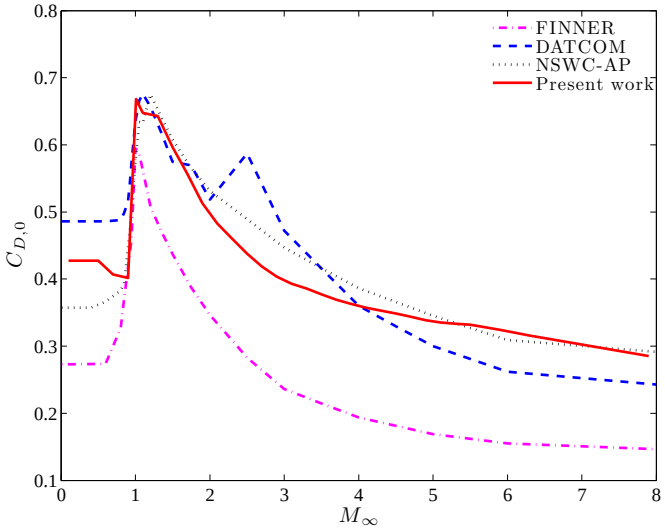

Figure 2.16: Zero-lift drag as a function of freestream Mach number for Configuration 4

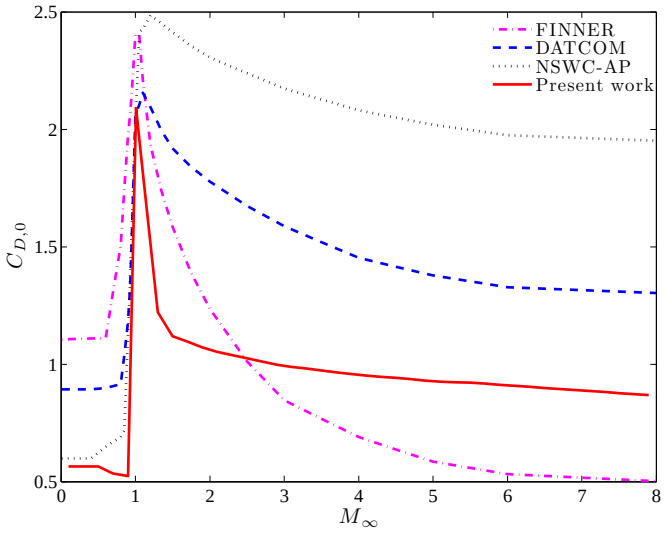

Figure 2.17: Zero-lift drag as a function of freestream Mach number for Configuration 5

The normal force coefficient as a function of angle of attack was only available for comparison with the FINNER aeroprediction code. This comparison was made at a subsonic, transonic, and supersonic freestream Mach number for each of the five configurations. The aeroprediction code in the present work includes the influence of vortex lift (see Section 2.2.1.2) on the overall normal force experienced by the projectile. The projectiles designs commonly modeled in PRODAS most often include fins purely as stabilizing surfaces rather than main lifting surfaces. Therefore, the fins and canards only experience small angles of attack for short periods of time. This means the overall vortex lift contribution would be small, if not negligible for such projectiles. This leads to the assumption that the PRODAS aerodynamic model might neglect to include the vortex lift contribution due to its small contribution and complex nature.

This assumption was investigated and is presented in Figure 2.18 through Figure 2.22. PRODAS FINNER data is plotted next to data produced by the current work outlined by the theory discussed in Chapter 2. When the vortex lift was omitted in the calculation, the present work showed similar trends and values of normal force coefficients for a wide range of angles of attack for each of the five configurations. When the vortex lift contribution was included, a rapid increase in normal force was found for increasing angle of attack. This trend follows the relationship which was found by Polhamus [33–36] shown in Figure 2.23. Figure 2.18 through Figure 2.22 show a decrease in the difference between the vortex lift and potential lift contributions for increasing aspect ratio at a given Mach number. This trend is also found by Polhamus and is illustrated by Figure 2.24.

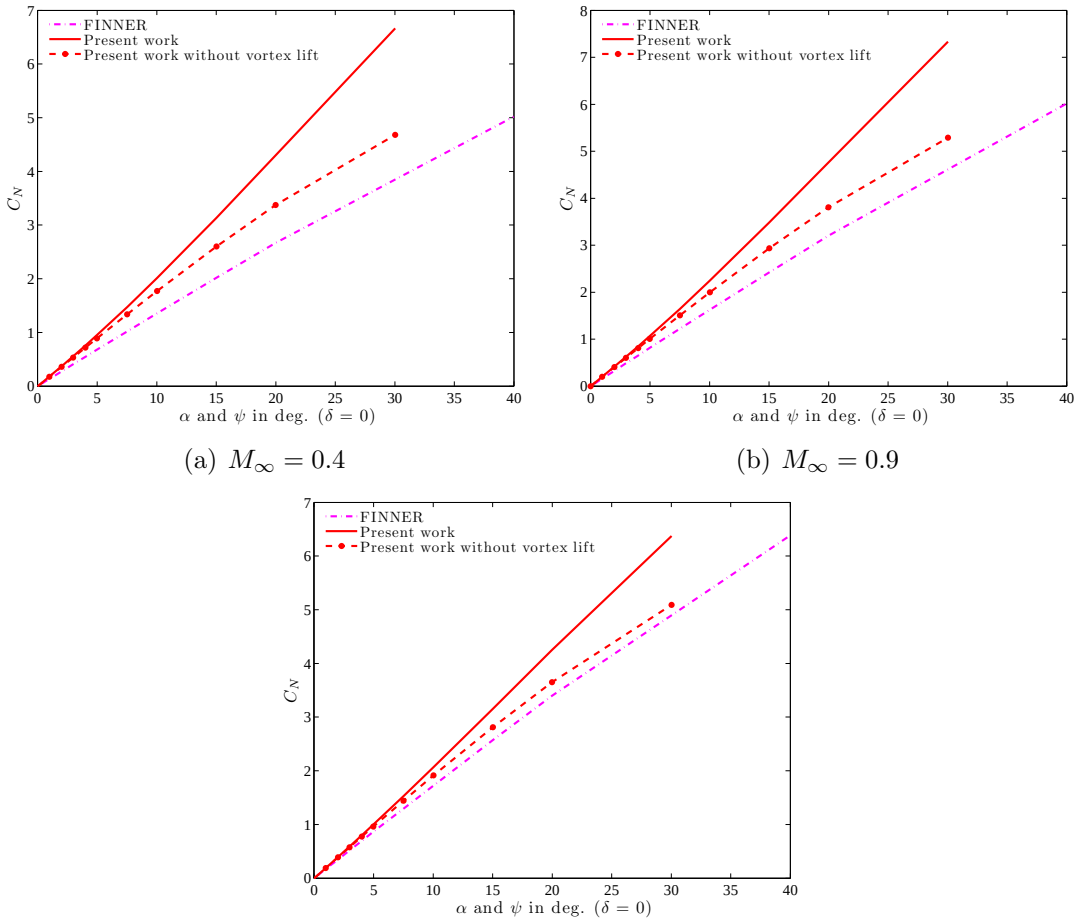

(a) $M_\infty = 0.4$

(b) $M_\infty = 0.9$

(c) $M_\infty = 2$

Figure 2.18: C_N variation at subsonic, transonic, and supersonic speeds for Configuration 1

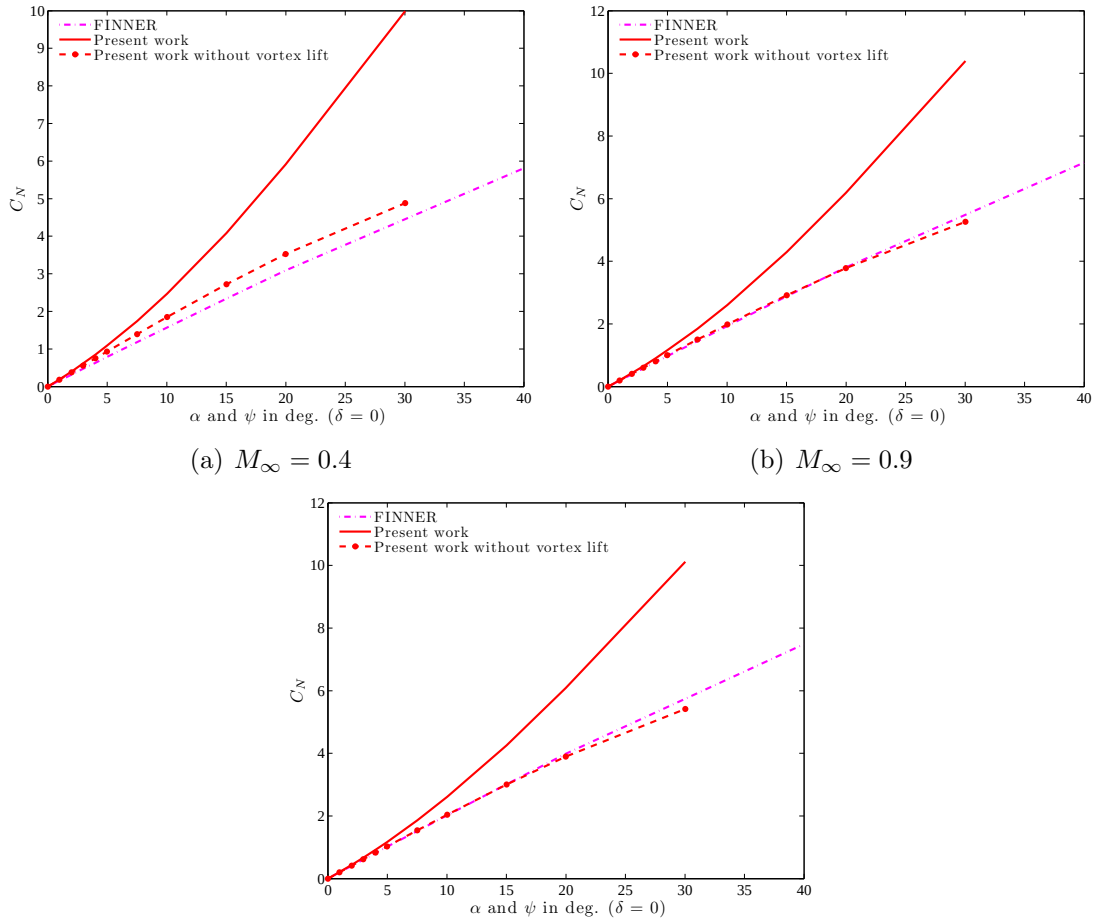

(a) $M_\infty = 0.4$

(b) $M_\infty = 0.9$

(c) $M_\infty = 2$

Figure 2.19: C_N variation at subsonic, transonic, and supersonic speeds for Configuration 2

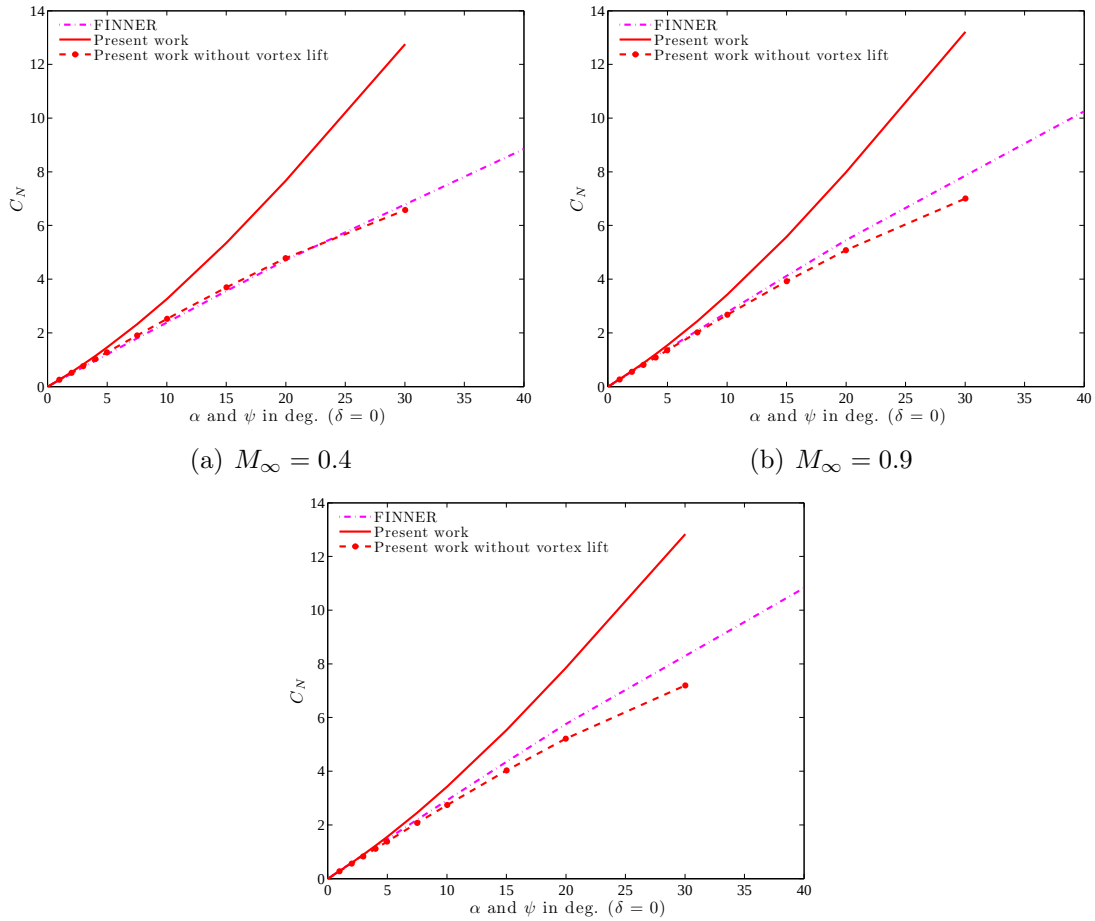

(a) $M_\infty = 0.4$

(b) $M_\infty = 0.9$

(c) $M_\infty = 2$

Figure 2.20: C_N variation at subsonic, transonic, and supersonic speeds for Configuration 3

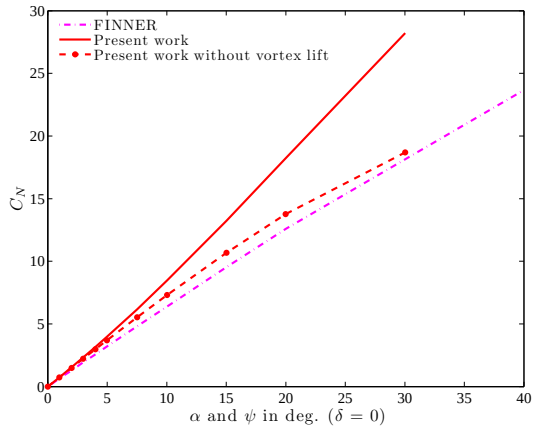

(a) $M_\infty = 0.4$

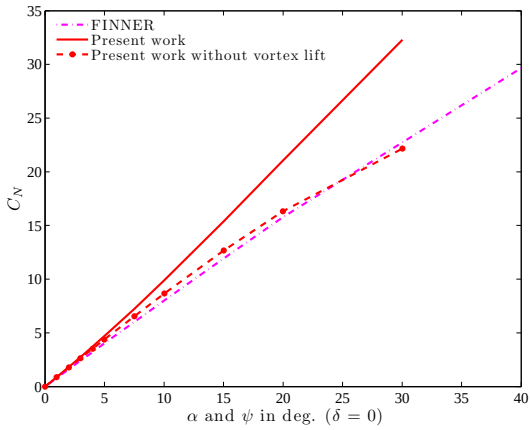

(b) $M_\infty = 0.9$

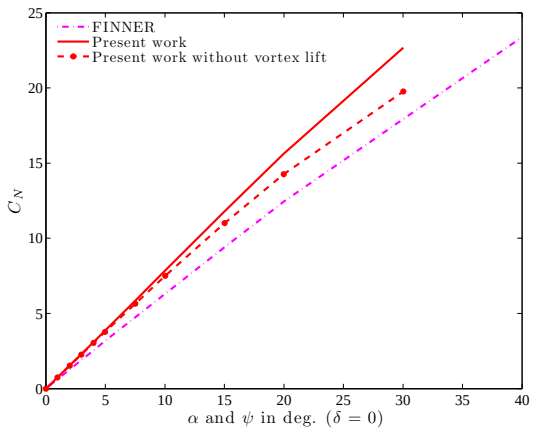

(c) $M_\infty = 2$

Figure 2.21: C_N variation at subsonic, transonic, and supersonic speeds for Configuration 4

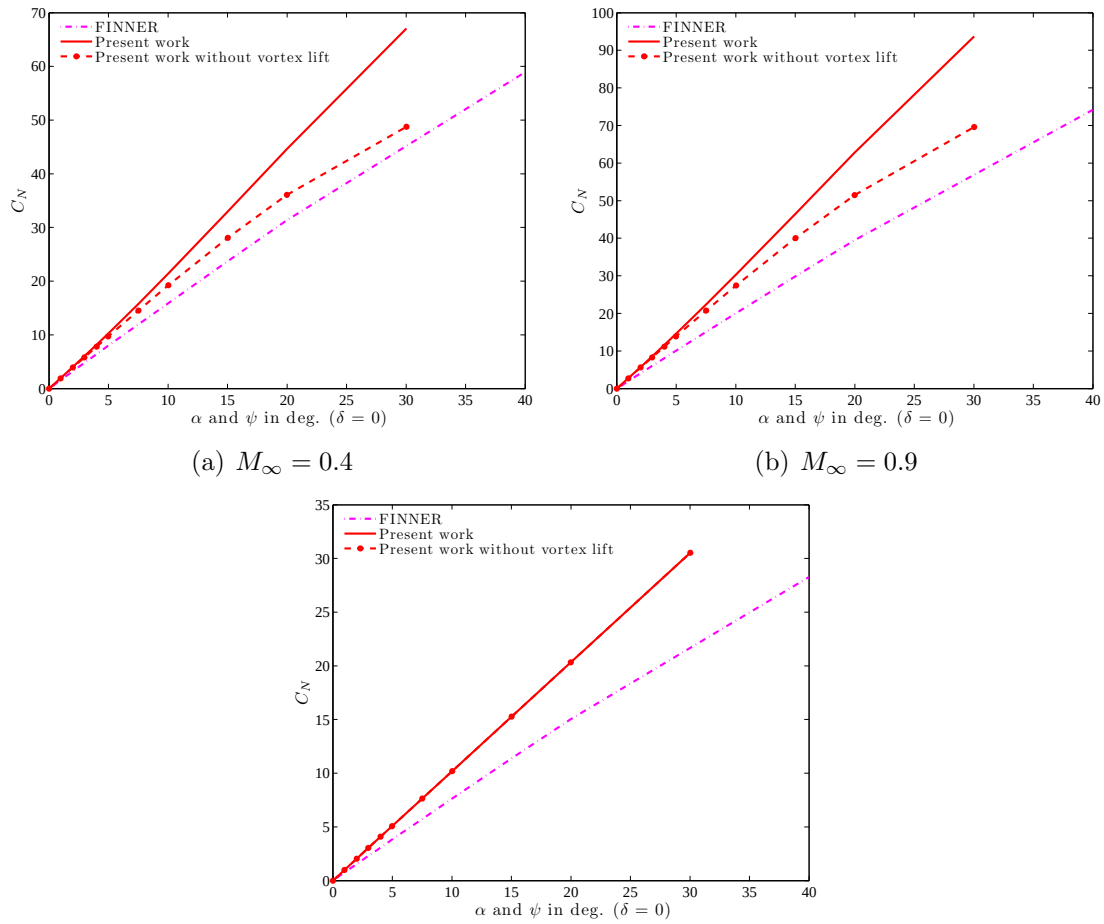

(a) $M_\infty = 0.4$

(b) $M_\infty = 0.9$

(c) $M_\infty = 2$

Figure 2.22: C_N variation at subsonic, transonic, and supersonic speeds for Configuration 5

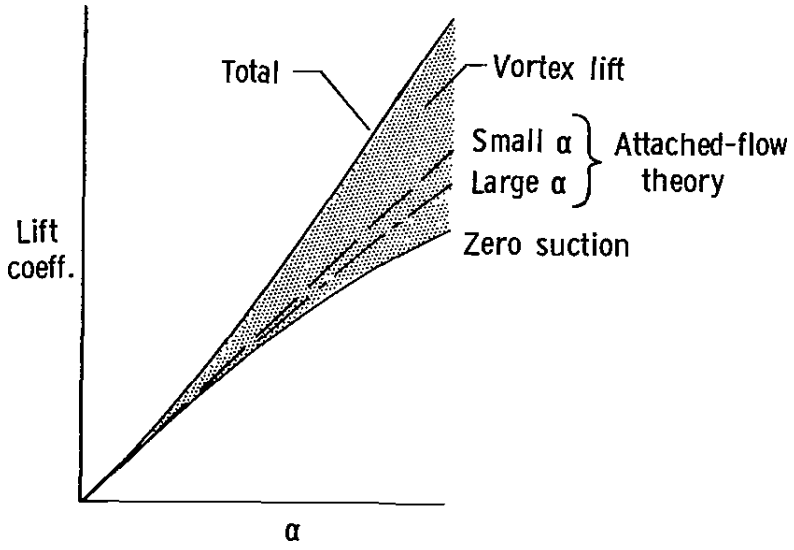

Figure 2.23: Vortex lift contribution as a function of angle of attack from Ref. [36]

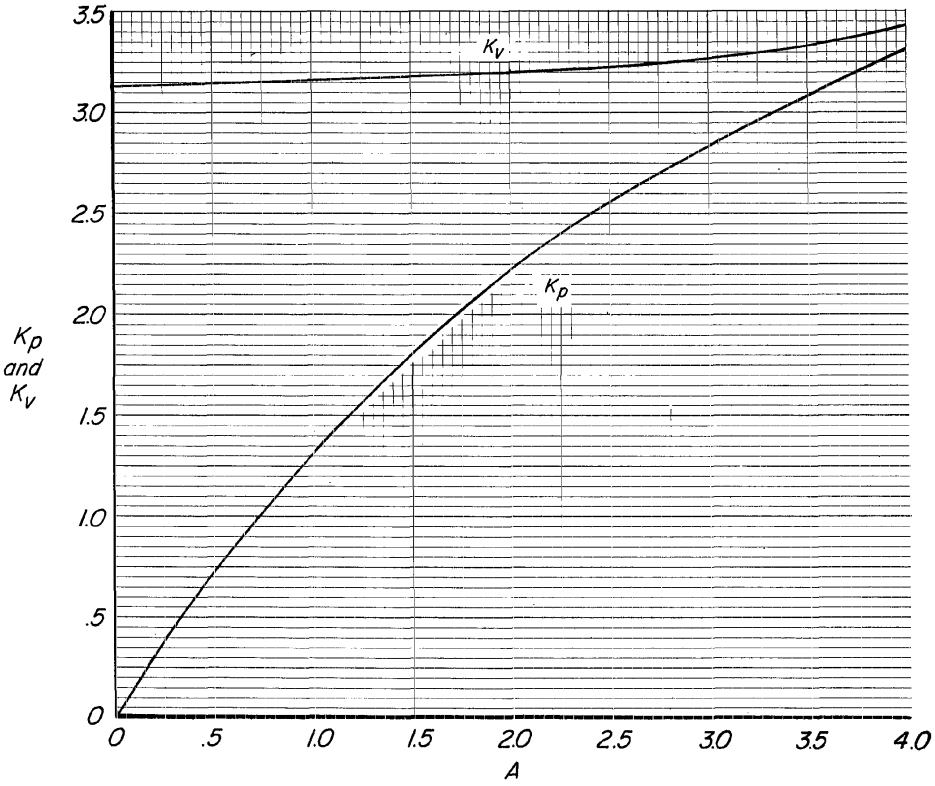

Figure 2.24: K_p and K_v values as a function of aspect ratio at $M_\infty = 0$ from Ref. [34]

The pitching moment gradient coefficients were compared for each of the five configurations listed in Table 2.6. The values for the location of the center of gravity were held constant between PRODAS and the aeroprediction code used in this thesis. Therefore, according to Equation 2.36 and Equation 2.38, the pitching moment gradient coefficient helps compare the predicted center of pressure locations between the aeroprediction codes.

Figure 2.25 through Figure 2.29 show the pitching moment gradient coefficients in per radians around $\alpha = \psi = \delta = 0$ as a function of freestream Mach number. The curves produced by the aeroprediction code in the current work exhibit the same trends with similar values to the curves produced by the other aeroprediction codes for each of the five configurations. Figure 2.25, Figure 2.28, and Figure 2.29 show that the present work accurately predicts the coefficient for a statically stable projectile. Figure 2.26 shows that the present work under predicts the coefficient value for a statically unstable projectile when compared to the other three codes. More importantly, Figure 2.26 shows an agreement between all four codes predicting that the projectile is in fact unstable for all Mach numbers of interest. Figure 2.27 shows an interesting case where the projectile is somewhere near the borderline between static stability and static instability.

The present work predicts stability for the entire Mach range. NSWC-AP predicts stability for most of the Mach range with a band of instability between Mach 2.5 and Mach 3.5. DATCOM and FINNER predict instability below Mach 3, and stability above Mach 3. Even with these differences, the magnitudes of the pitching moment gradient coefficient in Figure 2.27 are generally close. The overall assessment of the pitching moment gradient renders a sufficiently accurate prediction for use in preliminary design optimization.

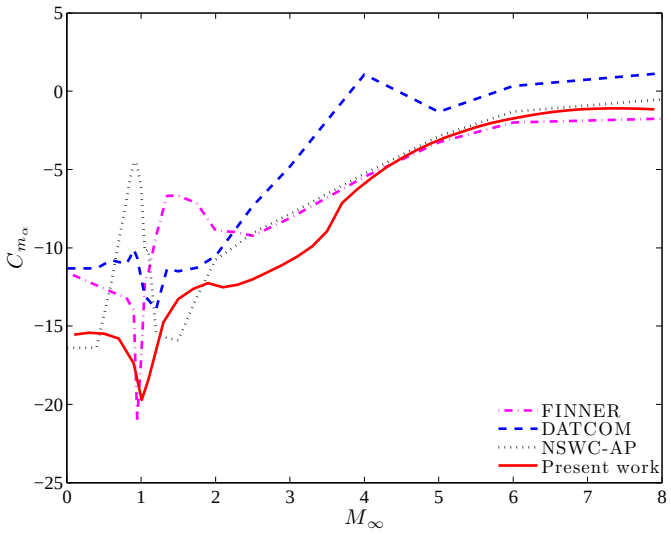

Figure 2.25: Pitching moment gradient coefficient as a function of freestream Mach number for Configuration 1

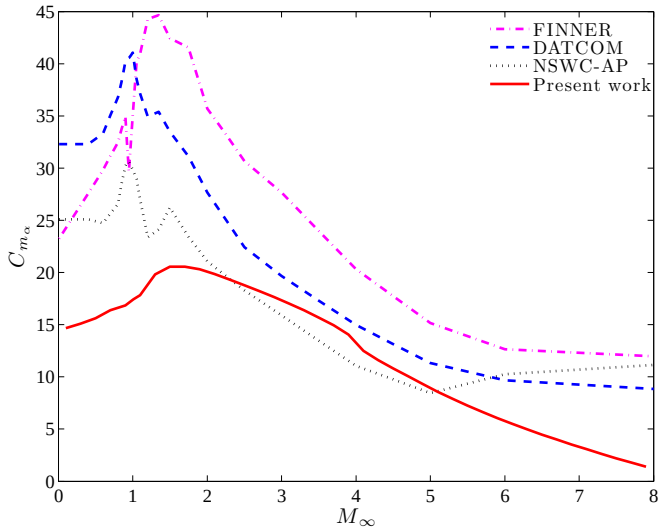

Figure 2.26: Pitching moment coefficient as a function of freestream Mach number for Configuration 2

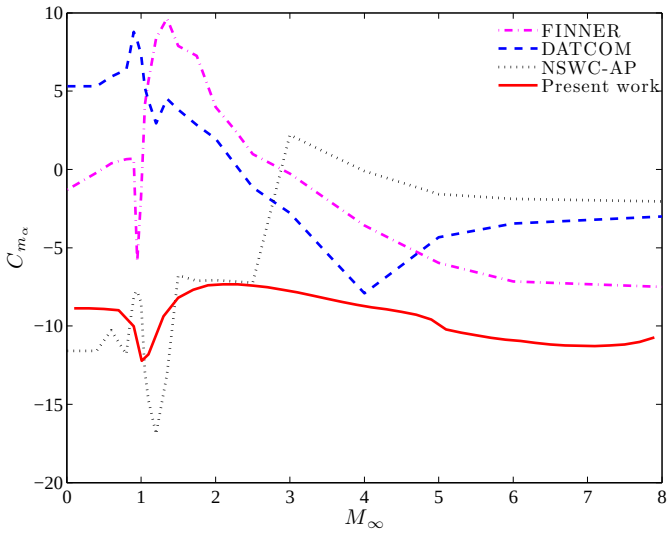

Figure 2.27: Pitching moment coefficient as a function of freestream Mach number for Configuration 3

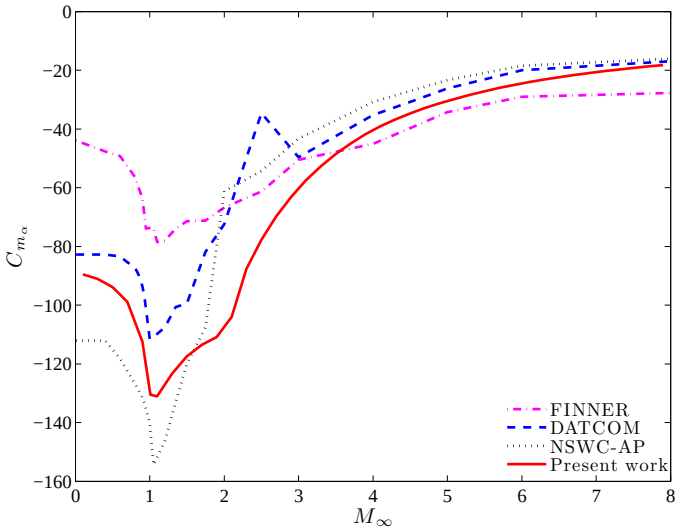

Figure 2.28: Pitching moment coefficient as a function of freestream Mach number for Configuration 4

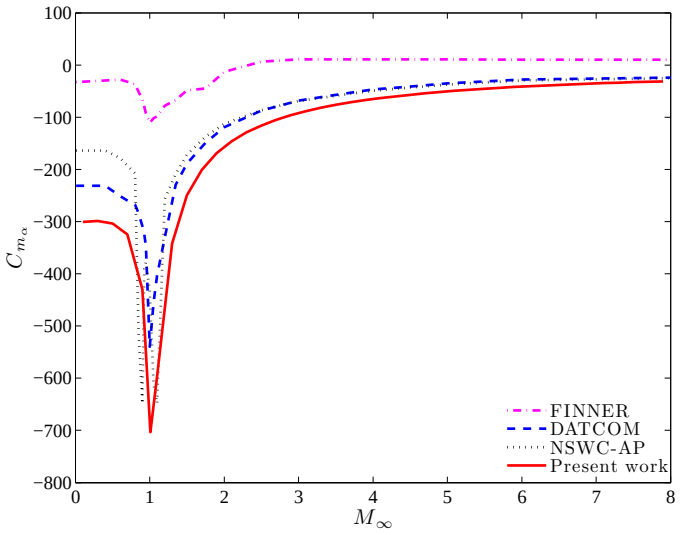

Figure 2.29: Pitching moment coefficient as a function of freestream Mach number for Configuration 5

Chapter 3
Description of Code and Optimization Methodology

The main goal of this research is to optimize the range of unpowered ballistic systems by utilizing several different morphing strategies. Three different scenarios of progressively increasing wing deployment capability were investigated. All three cases (Case 1, Case 2, and Case 3) assume a trajectory that begins with a projectile in a specific low drag zero lift configuration. Once apogee is reached, the respective morphing strategy takes over and the projectile sustains a canard controlled glide for the remainder of the trajectory. The three morphing strategies consist of a singular discrete post-apogee geometry, a configuration with dual swapping post-apogee geometries, and a rubber projectile of continuous morphing capability. An overall computer simulation code was written linking the aerodynamics of Chapter 2 with the morphing schemes, a trajectory simulation, and an optimizer. The general code layout is discussed in Section 3.1. The morphing strategies of Case 1, Case 2, and Case 3 and their implementation within an optimized trajectory simulation are discussed in detail in Sections 3.2, 3.3, and 3.4 respectively.

3.1 General Code Layout

The overall code layout consists of two main components: the objective/constraint functions and the optimizer. The objective functions are coded and implemented differently for each scenario, yet when optimized all accomplish the task of maximizing the range of the projectile. The objective function for each case uniquely

calls upon two different subroutines in order to provide a means of calculating its objective function value. The two subroutines are the aeroprediction subroutine and the trajectory simulation subroutine. The theory behind the code used in the aeroprediction subroutine is discussed in detail in Chapter 2. The aeroprediction code itself is organized such that for a given projectile geometry, freestream Mach number, projectile attitude, and altitude, the lift and drag coefficients can be calculated. The trajectory simulation subroutine utilizes the trajectory program Program to Optimize Simulated Trajectories (POST) developed by NASA. This program is a FORTRAN based code used to simulate point mass trajectories of aerospace flight vehicles [48]. The trajectory subroutine uses Python parsing scripts to create a POST input file. The input file includes two dimensional look-up tables for lift and drag coefficients as a function of Mach number and altitude as well as the initial launch conditions (muzzle velocity, launch angle, etc.). POST then simulates the projectile trajectory and outputs all pertinent flight data.

The objective functions and constraints are evaluated by an optimizer in order to accomplish the task of maximizing the range of the projectile. Within the three different cases, two types of optimizers are utilized. One is a gradient based optimizer and the other is a direct search algorithm based optimizer. These optimizers are used on the premise that they can find a set of design variables that maximize an objective function while obeying given constraints. The specific optimization methods used can be found in MATLAB's optimization toolbox. Details on these methods are explained in Section 3.4.1.

3.2 Case 1: Single Optimized Post-Apogee Geometry

Case 1 is the morphing scheme for which a single optimized post-apogee projectile geometry is found. The trajectory starts with a low drag projectile configuration at launch. It flies in a zero-lift (ballistic) trajectory up until apogee. From there, a single discrete wing and canard geometry is deployed. This post-apogee high lift to drag ratio configuration continues on a canard controlled glide for the remainder of the flight. The canard control surfaces deflect such that at every instance in the gliding flight the projectile is sustaining a maximum possible lift to drag ratio. Case 1,2, and 3 only consider maneuvers in the pitching plane of the projectile. Therefore, the vertical set of wings and canards do not change from the initial low drag configuration and serve only to maintain yaw stability. Note that during the entire trajectory, the constraints of both static stability and trimmed (zero pitching moment) flight conditions are satisfied. An illustrated example of this trajectory and the corresponding geometry changes are shown in Figure 3.1.

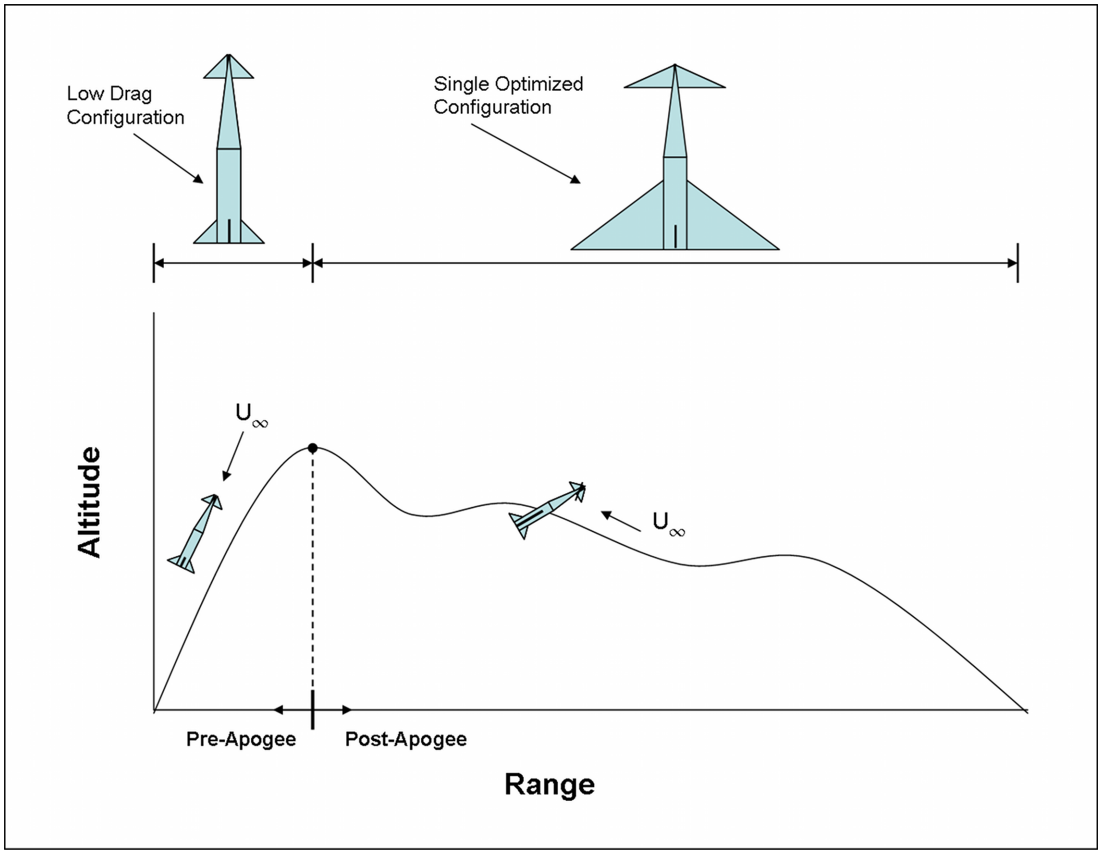

Figure 3.1: Example of Case 1 trajectory

The following Case 1 optimization problem was solved: find the values of the design variables contained in $\vec{X}$ that will maximize the objective function $F\left(\vec{X}\right)$, subject to constraints $G_j\left(\vec{X}\right) \leq 0$ for $j = 1, 2$ and design variable side constraints $X_i^L \leq X_i \leq X_i^U$ for $i = 1$ to N, where N is the total number of design variables. The design variables for Case 1 are the post-apogee wing and canard geometries as well as the initial launch angle. These variables are shown graphically in Figure 3.2

and expressed as a design vector given by Equation 3.1:

$$\vec{X} = \begin{bmatrix} b_{wing} \\ c_{wing} \\ b_{canard} \\ c_{canard} \\ \kappa \end{bmatrix} \tag{3.1}$$

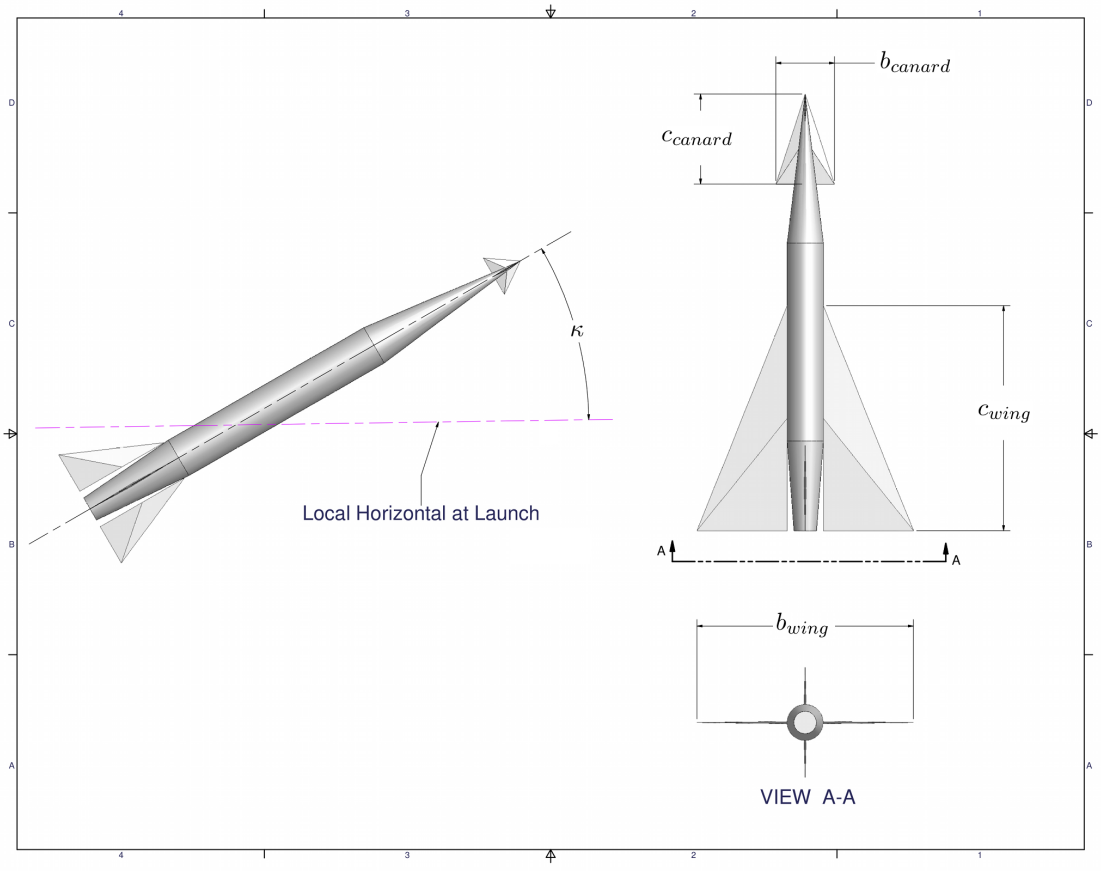

Figure 3.2: Example of Case 1 design variables

The value of the objective function for Case 1 is simply the final range of the launched projectile for a given initial launch velocity. The objective function

provides a calculation of the final range for a given $\vec{X}$ and initial launch velocity by performing the following steps:

1. Assign initial guesses of α, ψ, and δ as a function of altitude and Mach number. Note that for Case 1, ψ is set to be equal to α at all times.

2. Use aeroprediction code to calculate lift and drag coefficients as a function of altitude and Mach number keeping a zero angle of attack for pre-apogee configuration and using α, ψ, and δ values for the post-apogee configuration.

3. Simulate the projectile trajectory using POST

4. Analyze POST output and record the altitudes and Mach numbers experienced during the post-apogee trajectory to use as reference points in a 2D lookup table. See Table 3.1 as an example.

5. Solve the following optimization problem: find values of α, ψ, and δ such that $\frac{L}{D}$ is maximized for each of the recorded altitudes and Mach numbers from Step 4 (i.e. fill in 2D lookup table), while obeying the stability/trim constraints. The optimizer used in this step is the gradient based solver (see Section 3.4.1.1).

6. Repeat Steps 2-5 until consecutive trajectory total range values from Step 3 converge within a desired tolerance.

Table 3.1: Example 2D lookup table of post-apogee α/ψ values as a function of Mach number and altitude

M_∞	$h = 0$ m	$h = 5,000$ m	$h = 10,000$ m	$h = 15,000$ m	$h = 20,000$ m
0.1	7.3°	-	-	-	-
0.4	6.5°	7.1°	-	-	-
0.8	-	5.3°	5.8°	-	-
1.0	-	-	4.7°	4.9°	-
1.1	-	-	3°	3.2°	-
1.5	-	-	-	2°	1.8°

The constraints on the designs are defined by the upper and lower bounds on the variables and required static stability and proper trimmed conditions for a given body angle of attack α and canard deflection angle δ. As described in Section 2.4, the value of C_m is zero when the projectile is at trimmed conditions. For static stability, the value of C_{m_α} must be less than zero. These conditions are given by Equations 2.36 and 2.38 respectively. The four corresponding constraint functions can be expressed as the following:

$$\begin{aligned} G_1\left(\vec{X}\right) &= \vec{X} \leq \vec{X^U} \\ G_2\left(\vec{X}\right) &= \vec{X} \leq -\vec{X^L} \\ G_3\left(\vec{X}\right) &= |C_m| - tol \leq 0 \\ G_4\left(\vec{X}\right) &= C_{m_\alpha} \leq 0 \end{aligned} \tag{3.2}$$

where *tol* is some small tolerance. The constraint functions are only fully satisfied when Equation 3.2 is true at all Mach numbers and altitudes experienced during the trajectory.

Once the objective function and constraint functions are defined for Case 1,

an optimizer can solve for an optimum design vector $\vec{X}^*$ such that the range is maximized. Case 1 utilizes the PatternSearch optimizer in MATLAB's global optimization toolbox. PatternSearch is a zero-th order direct search optimizer. More detail regarding the PatternSearch optimizer methodology and characteristics can be found in Section 3.4.1.

3.3 Case 2: Dual Optimized Post-Apogee Geometries

Case 2 is the morphing scheme for which dual optimized post-apogee projectile geometries are found. The trajectory starts with a low drag projectile configuration at launch. It flies in a zero-lift (ballistic) trajectory up until apogee. From there, the projectile can choose between two discrete sets of wing and canard geometries. At any point in time after apogee, the projectile can swap between the two configurations in order to achieve the highest possible lift to drag ratio, and therefore achieve the best possible range. The projectile continues on a canard controlled glide for the remainder of the flight. The canard control surfaces deflect such that at every instance in the gliding flight the projectile is sustaining a maximum possible lift to drag ratio while obeying the stability constraints. An illustrated example of this trajectory and the corresponding geometry changes are shown in Figure 3.3.

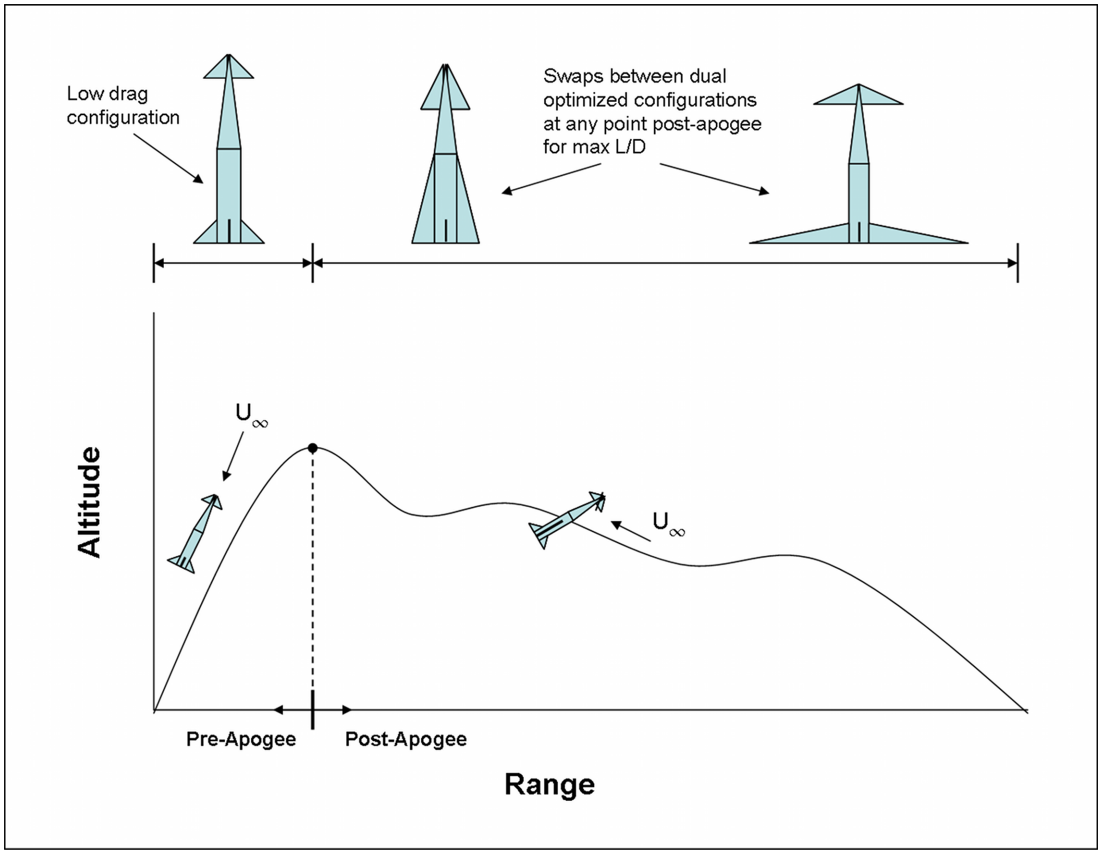

Figure 3.3: Example of Case 2 trajectory

The design variables for Case 2 are the two sets post-apogee wing and canard geometries as well as the initial launch angle. These variables are shown graphically in Figure 3.4 and expressed as a design vector given by Equation 3.3:

$$\vec{X} = \begin{bmatrix} b_{wing_{c1}} \\ c_{wing_{c1}} \\ b_{canard_{c1}} \\ c_{canard_{c1}} \\ \kappa \\ b_{wing_{c2}} \\ c_{wing_{c2}} \\ b_{canard_{c2}} \\ c_{canard_{c2}} \end{bmatrix} \tag{3.3}$$

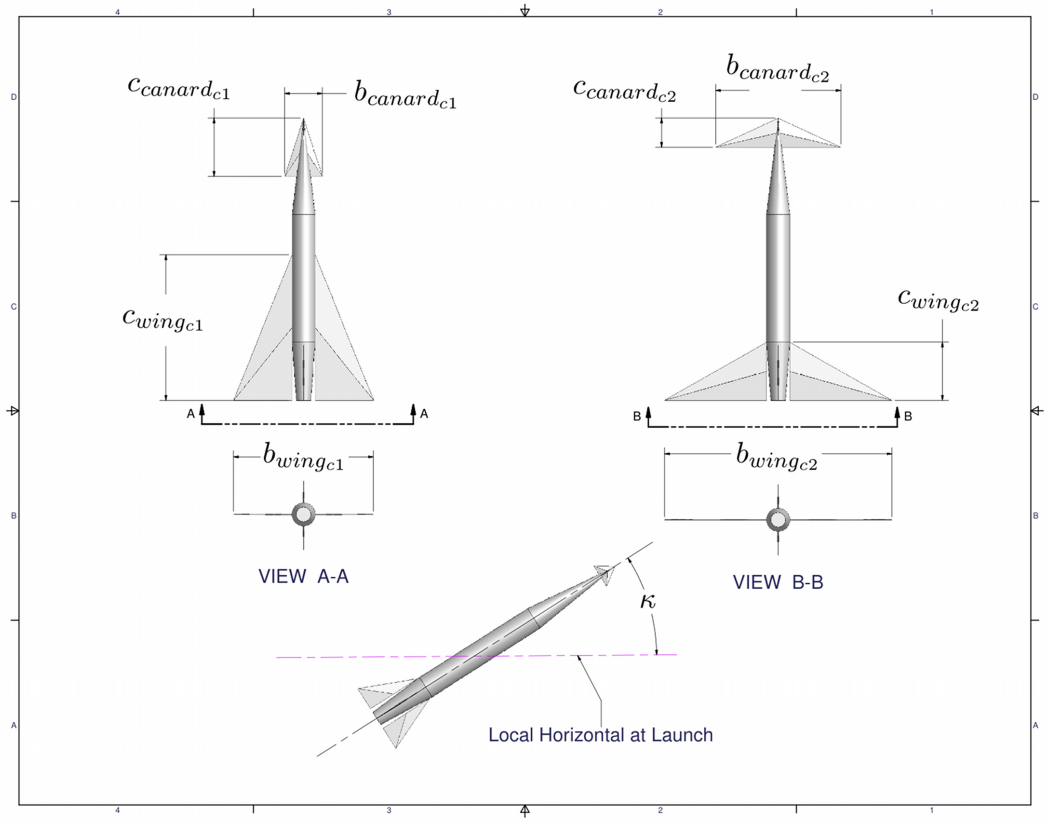

Figure 3.4: Example of Case 2 design variables

The value of the objective function for Case 2 is the final range of the launched projectile for a given initial launch velocity. The objective function provides a calculation of the final range for a given $\vec{X}$ and initial launch velocity by performing the following steps:

1. Assign initial guesses of α_{c1}, ψ_{c1}, and δ_{c1} as a function of altitude and Mach number for configuration 1. Note that for Case 2, ψ_{c1} is set to be equal to α_{c1} at all times.

2. Assign initial guesses of α_{c2}, ψ_{c2}, and δ_{c2} as a function of altitude and Mach number for configuration 2. Note that for Case 2, ψ_{c2} is set to be equal to α_{c2} at all times.

3. Use the aeroprediction code to calculate lift and drag coefficients as a function of altitude and Mach number using α_{c1}, ψ_{c1}, and δ_{c1} values for post-apogee configuration.

4. Use the aeroprediction code to calculate lift and drag coefficients as a function of altitude and Mach number using α_{c2}, ψ_{c2}, and δ_{c2} values for post-apogee configuration.

5. For each Mach number and altitude combination, evaluate which configuration from Steps 3-4 gives a larger $\frac{L}{D}$.

6. Create POST input file including the lift and drag coefficient 2D tables as functions of Mach number and altitude using the values found in Step 5.

7. Simulate projectile trajectory using POST

8. Record the altitudes and Mach numbers experienced during the post-apogee trajectory to use as reference points in a 2D lookup table. See Table 3.1 as an example.

9. Solve the following optimization problem: find values of α_{c1}, ψ_{c1}, and δ_{c1} that maximize $\frac{L}{D}$ for each of the recorded altitudes and Mach numbers (i.e. fill in 2D lookup table), while obeying the stability/trim constraints. The optimizer used in this step is the gradient based solver (see Section 3.4.1.1).

10. Solve the following optimization problem: find values of α_{c2}, ψ_{c2}, and δ_{c2} that maximize $\frac{L}{D}$ for each of the recorded altitudes and Mach numbers (i.e. fill in 2D lookup table), while obeying the stability/trim constraints. The optimizer used in this step is the gradient based solver (see Section 3.4.1.1).

11. Repeat Steps 3-10 until consecutive trajectory total range values from Step 7 converge within a desired tolerance.

The constraints on the designs are the same as described for Case 1. The constraint functions are only fully satisfied when Equation 3.2 is true at all Mach numbers and altitudes experienced by both of the two swapping geometries during the trajectory. Case 2 is similar to Case 1 as it also utilizes the PatternSearch optimizer in MATLAB's global optimization toolbox.

3.4 Case 3: Rubber Projectile

Case 3 is the scheme for which the projectile continuously morphs to an optimum geometry post-apogee. The trajectory starts with a low drag projectile configuration at launch. It flies in a zero-lift (ballistic) trajectory up until apogee. From that point on, the projectile may deploy its wings and canards to any possible geometry within the upper and lower design limits in order to achieve a maximum lift to drag ratio. The projectile continues on a canard controlled glide for the remainder of the flight. The canard control surfaces and wings deflect such that at every instance in the gliding flight the projectile is sustaining a maximum possible lift to drag ratio while obeying the stability constraints. An illustrated example of this trajectory and the corresponding geometry changes are shown in Figure 3.5.

The design variables for Case 3 include the wing and canard geometries as well as the wing angle of attack, body angle of attack, and canard deflection angle. Note that Case 3 differs from Case 1 and Case 2 for that it allows the wing angle of attack to be independent from the body angle of attack. The design variables are shown graphically in Figure 3.6 and expressed as a design vector given by Equation 3.4:

$$\vec{X} = \begin{bmatrix} b_{wing} \\ c_{wing} \\ b_{canard} \\ c_{canard} \\ \alpha \\ \psi \\ \delta \end{bmatrix} \tag{3.4}$$

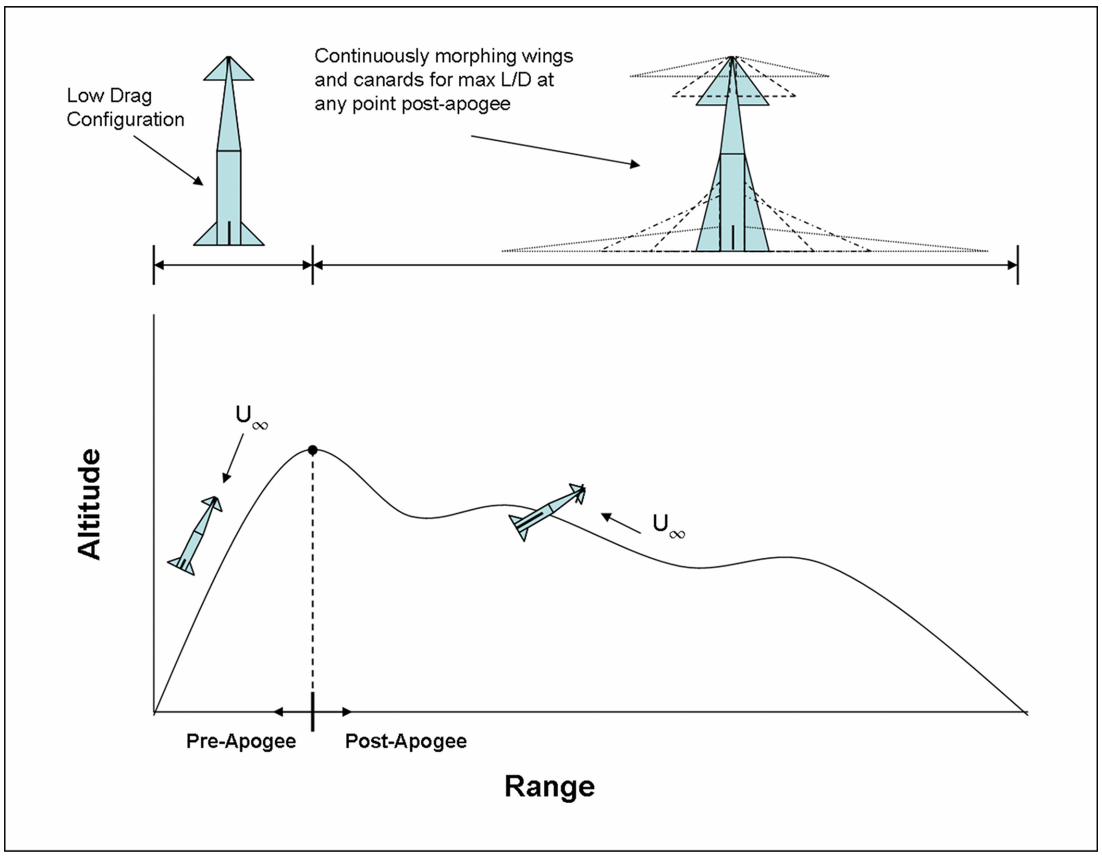

Figure 3.5: Example of Case 3 trajectory

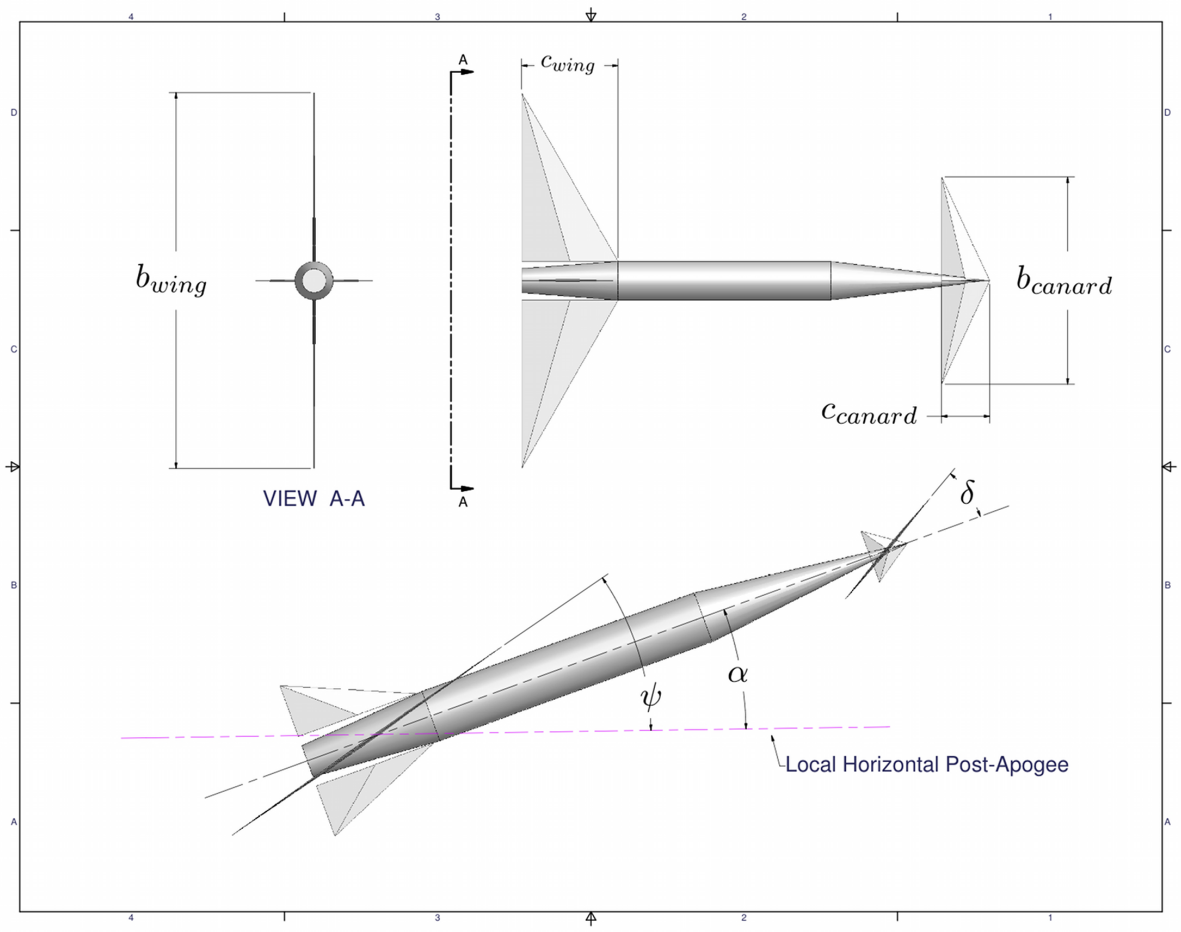

Figure 3.6: Example of Case 3 design variables

Once the design vector is defined, it can be evaluated by the objective function and constraint functions. The objective function and constraint functions are evaluated for a given value of altitude and Mach number. The objective function takes $\vec{X}$ along with a given Mach number and altitude and calculates a lift to drag ratio of the projectile. The methodology for Case 3 differs from that of Case 1 and 2. For Case 3 a gradient based optimizer solves for a $\vec{X}^*$ that gives a maximum lift to drag ratio for the given value of Mach number and altitude, while obeying the stability constraints. This optimization is done at a range of Mach number and

altitude values. This essentially builds a two dimensional table of optimum designs as a function of altitude and Mach number. This table of designs can be input into the aeroprediction code to render two dimensional look-up tables of lift and drag coefficients as a function of altitude and Mach number. POST can then read these input tables and simulate the trajectory of a continuously morphing optimized projectile for a given launch angle and launch velocity. The last step is to find the optimum launch angle. This was done by simply simulating a series of trajectories by parametrically changing the value of the launch angle until a maximum range is found.

3.4.1 Optimization Methods

3.4.1.1 Gradient Based Algorithm

The first order gradient based constrained optimization method used in this thesis employs the interior-point algorithm as described in Refs. [49–51]. The interior-point algorithm is capable of finding the constrained minimum of nonlinear multivariable functions. It is also capable of handling multiple nonlinear equality and inequality constraints. This algorithm was used because it produces feasible designs at each iteration and also for its ability to handle both large sparse problems and small dense problems. This would guarantee the most success for a feasible design for the optimization problems of interest in this thesis.

The interior-point algorithm works by solving a series of approximate minimization problems as defined by the following:

$$\min F_m\left(\vec{X},\vec{S}\right) = \min F\left(\vec{X}\right) - m\sum_j \ln\left(S_j\right), \text{ subject to } \sum_j G_j\left(\vec{X}\right) + S_j = 0 \quad (3.5)$$

where, $\vec{S}$ is a vector of j slack variables (one for each constraint). Each slack variable must be positive in order to keep the logarithmic term bounded and the constraints satisfied. The logarithmic term in Equation 3.5 is called the barrier function, where m is the barrier parameter. As m approaches zero the minimum of the approximate objective function F_m approaches the minimum of the actual objective F. In other words, as m approaches zero, Equation 3.5 approaches the following equation:

$$\min F\left(\vec{X}\right), \text{ subject to } \sum_j G_j\left(\vec{X}\right) \leq 0 \tag{3.6}$$

The algorithm solves the approximated equality constrained problem for a given value of m and iteratively decreases m until a convergence tolerance is reached. To solve the approximated problem at each step, the algorithm performs what is called a Newton step. The Newton step applies the Karush-Kuhn-Tucker (KKT) conditions to Equation 3.5 by using a linearized approximation to the Lagrangian. The KKT conditions are necessary conditions that are mathematically true when evaluated at a local constrained minimum. After applying the KKT conditions the following system of equations is obtained:

$$\begin{bmatrix} H & 0 & J^T \\ 0 & S_{diag}\Lambda_{diag} & -S_{diag} \\ J & -S_{diag} & I \end{bmatrix} \begin{bmatrix} \Delta\vec{X} \\ \Delta\vec{S} \\ \Delta\vec{\lambda} \end{bmatrix} = \begin{bmatrix} \nabla F\left(\vec{X}\right) - J^T\vec{\lambda} \\ S_{diag}\vec{\lambda} - m\vec{e} \\ \vec{G} + \vec{S} \end{bmatrix} \tag{3.7}$$

where, J is the Jacobian of the constraints, $\vec{\lambda}$ is a vector of the Lagrange multipliers, $\vec{e}$ is a vector of ones the size of $\vec{G}$, and H is the Hessian of the Lagrangian given by the following:

$$H = \nabla^2 F\left(\vec{X}\right) + \sum_j \lambda_j \nabla^2 G_j\left(\vec{X}\right) \tag{3.8}$$

At each iteration, the Hessian is approximated at the current design vector $\vec{X}$ using the Broyden-Fletcher-Goldfarb-Shanno (BFGS) method [52, 53]. Along with the Hessian, the Jacobian and the Lagrange multipliers are calculated at the current design. Equation 3.7 can then be solved for $\Delta\vec{X}$, $\Delta\vec{S}$, and $\Delta\vec{\lambda}$ by simply using matrix factorization. $\Delta\vec{X}$ is then used to increment the current design vector $\vec{X}$ to form a new design vector for use in the next iteration. The next iteration can then proceed with new value of $\vec{X}$ and the incrementally smaller value of m. This process repeats until m is sufficiently small, such that a convergence tolerance is met. Implementation of the interior-point algorithm described in Refs. [49–51] is available as a MATLAB function in the optimization toolbox. This function, *fmincon*, was used to apply the relevant constrained optimization theory to the current work.

3.4.1.2 Direct Search Algorithm

Within the gradient based optimizers the gradients and Hessians of the objective and constraint functions are usually computed by using a forward or central finite difference scheme. This is true in the MATLAB function *fmincon*. MATLAB is currently only capable of defining one step size for the finite differencing for all of the variables in the design space, per iteration. When analyzing the design space constructed for Case 1 and Case 2, it was found that the gradient based method had trouble constructing meaningful gradients and Hessians. This was due to the big differences in the hyperspace curvature of the objective function and the constraint functions. The gradient based optimizers would terminate prematurely and produce erroneous results. The use of gradient free methods would alleviate this problem and

was therefore used for Case 1 and Case 2. Several gradient-free methods available in MATLAB can solve problems that contain objective or constraint functions which are discontinuous, stochastic, or non-differentiable. These types of methods, though not guaranteed, are capable of finding global maxima or minima, whereas gradient based methods can only guarantee a local maxima or minima.

The direct search constrained optimization method used in this thesis is from the MATLAB Genetic Algorithm and Direct Search toolbox (GADS). This toolbox employs zero-th order methods to search for global solutions to problems that may contain multiple minima or maxima. The three methods which are available in this toolbox include a genetic algorithm based method, a direct search method, and a simulated annealing method. Each of these methods have their own advantages and disadvantages. When deciding which method to use, it was important to look at the structure of the posed optimization problem. The objective functions constructed for Case 1 and Case 2 tend to have long function evaluation times. The lengthy calculations occur due to the inner optimization problem which needs to be solved for each evaluation of the objective function. The long function evaluation times made it important to pick a gradient free method which would minimize the number of function evaluations needed to solve the optimization problem.

MATLAB's genetic algorithm based optimizer is highly customizable rendering it a very powerful tool. Yet, this solver tends to require more function evaluations when compared to the other available solvers. MATLAB's simulated annealing solver only allows the use of linear bound constraints. Case 1 and Case 2 require the use of non-linear constraints. The direct search solver, called *patternsearch*,

allows for non-linear constraints and tends to require less function evaluations than that of the genetic algorithm. The *patternsearch* function was therefore the best choice.

The *patternsearch* function finds the constrained minimum value of the objective function by using the Augmented Lagrangian Pattern Search (ALPS) algorithm [54–56]. ALPS solves a series of subproblems formulated by combining the objective function and nonlinear constraint functions using penalty parameters to form a Lagrangian barrier function. The Lagrangian barrier function is defined by the following equation:

$$\Theta\left(\vec{X},\vec{\lambda}\right) = F\left(\vec{X}\right) - \sum_{j} m\lambda_j^2 \log\left(m\lambda_j - G_j\left(\vec{X}\right)\right) \tag{3.9}$$

The algorithm uses a pattern search technique to find a minimum to the subproblem until convergence criteria are met. The Lagrange multipliers are then updated and the KKT conditions are checked. If all conditions are satisfied, then the optimum design vector $\vec{X}^*$ was found. If the KKT conditions are not satisfied to within a specified tolerance, then the barrier parameter m in Equation 3.9 is decreased, thus defining a new subproblem. The pattern search algorithm proceeds to find the minimum of the new sub problem. This process iterates until a minimum is found.

The pattern search algorithm finds a minimum of each subproblem by creating a mesh of trial points around the current design point. At each iteration, the algorithm polls the points in the current mesh by computing their Lagrangian barrier function values. As soon as a point whose Lagrangian barrier function value is less than that of the current point, the algorithm stops polling the mesh points. If this

occurs, the poll was successful and the point it found becomes the current point at the next iteration. If the algorithm fails to find a point that improves the objective function, the poll is called unsuccessful and the current point stays the same at the next iteration. At the end of each successful iteration the size of the mesh is doubled. At the end of each unsuccessful iteration, the mesh size is reduced by half its current size. These iterations continue until a minimum mesh size is reached, or any of the other convergence criteria are met.

Chapter 4
Optimal Configurations and Trajectories

This section presents the optimization results of the objective functions described in Sections 3.2, 3.3, and 3.4. Each case was optimized using three separate initial launch velocities for two sets of upper design variable limits, for a total of six runs per case. The three initial launch velocities tested were 1200, 1400, and 2000 meters per second. These velocities were chosen to represent the current capabilities of standard 155 mm military gun muzzles as well as the launch capabilities of electromagnetic systems. Tables of the design variables and their upper and lower constraint values for each case are given in their respective sections. Table 4.1 describes the conditions used for each of the six runs per case. The projectile parameters and launch conditions that are constant throughout all runs for all cases are listed in Table 4.2. The optimization results are provided as iteration histories for the various functions and parameters associated with the formulated problem. Full iteration histories for Case 1 and Case 2 and an example iteration history for Case 3 are available in Appendix A. Tables consisting of the final optimized geometries and the corresponding maximized ranges are given along side the initial designs given to the optimizer. Plots of the optimum trajectories are also provided.

Table 4.1: List of optimization runs for each case

Case name ($X = 1, 2, 3$)	Initial launch velocity (m/s)	Upper and lower limits
Case Xa	1200	Side constraints set 1
Case Xb	1200	Side constraints set 2
Case Xc	1400	Side constraints set 1
Case Xd	1400	Side constraints set 2
Case Xe	2000	Side constraints set 1
Case Xf	2000	Side constraints set 2

Table 4.2: Constant projectile characteristics for all cases

Constant projectile dimensions	Value
Total mass	19.5 kg
Total length	970 mm
Body diameter	80 mm
Nose length	330 mm
Boattail length	200 mm
Boattail diameter	50 mm
X_{cg}	7.5 cal. (from base)
Number of Wings	4 (cruciform)
Number of Canards	4 (cruciform)
Wing mid-chord thickness at wing root	5 mm
Canard mid-chord thickness at canard root	5 mm
Distance to canard leading edge	970 mm (from base)
Pre-apogee or "low drag" wing span	150 mm
Pre-apogee or "low drag" wing rood chord	190 mm
Pre-apogee or "low drag" canard span	70 mm
Pre-apogee or "low drag" canard chord	60 mm

4.1 Case 1 Optimum Configuration and Trajectory

The optimization results of the six runs for Case 1 are provided in this section. The set up of each run follows the nomenclature presented in Table 4.1, where the side constraints are explicitly listed in Table 4.3. The lower and upper limits of the side constraints were chosen to enable a modest range of possible projectile geometries, while keeping a sense of overall practicality. The launch system, wing deployment possibilities, and manufacturing considerations were all taken into account when deciding on the geometry limits. The lower limits of side constraints set 2 are identical to that of set 1. The upper limits for the wing span and canard span in set 2 are simply double that of set 1. The upper limits of the wing chord and canard chord lengths are the same for set 1 and set 2.

Table 4.3: Case 1 optimization design variable side constraints

Design variable	Side constraints set 1	Side constraints set 2
Wing span	88 mm $\leq b_{wing} \leq$ 970 mm	88 mm $\leq b_{wing} \leq$ 1,940 mm
Wing root chord	80 mm $\leq c_{wing} \leq$ 640 mm	80 mm $\leq c_{wing} \leq$ 640 mm
Canad span	81 mm $\leq b_{canard} \leq$ 155 mm	81 mm $\leq b_{canard} \leq$ 310 mm
Canard root chord	10 mm $\leq c_{canard} \leq$ 330 mm	10 mm $\leq c_{canard} \leq$ 330 mm
Launch angle	$26^\circ \leq \kappa \leq 75^\circ$	$26^\circ \leq \kappa \leq 75^\circ$

The initial designs given to the optimizer for each run along with the final optimized geometries are listed in Table 4.4. Geometric representations of the initial and optimum geometries for Case 1 are illustrated in Figure 4.1. The initial designs for Case 1a through Case 1e were chosen to have the same geometry as the pre-apogee or "low drag configuration". For the sake of minimizing convergence time the initial design for Case 1f was chosen to be a design found near the optimal design

within the iteration history of Case 1d. The corresponding ranges found from the optimization for each run is presented in Table 4.4. Full iteration histories of the objective function (range), mesh size, constraint value, and design variables can be found in Appendix A.

Table 4.4: Case 1 initial and optimal designs for maximizing projectile range (measurements in mm unless otherwise specified)

Case number	Design	b_{wing}	c_{wing}	b_{canard}	c_{canard}	κ	Range (km)
Case 1a	Initial	150	220	82	60	55°	94.62
	Optimum	260	584	154	124	57.15°	129.42
Case 1b	Initial	150	220	82	60	55°	94.62
	Optimum	428	108	307	220	60°	187.9
Case 1c	Initial	150	220	82	60	55°	125.20
	Optimum	238	626	155	140	54.61°	169.10
Case 1d	Initial	150	220	82	60	55°	125.20
	Optimum	335	213	309	240	55.27°	239.36
Case 1e	Initial	150	220	82	60	55°	237.97
	Optimum	194	304	152	188	50.08°	312.88
Case 1f	Initial	335	206	309	240	55.79°	383.41
	Optimum	243	269	310	328	48.72°	414.99

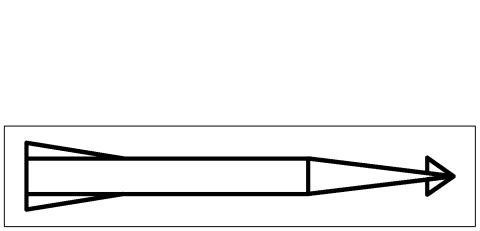

(a) Case 1a-1e initial geometry

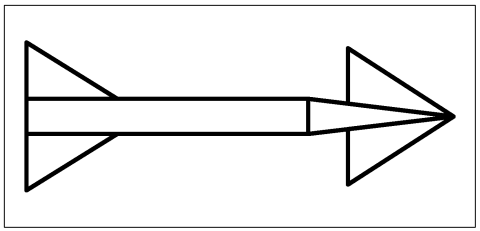

(b) Case 1f initial geometry

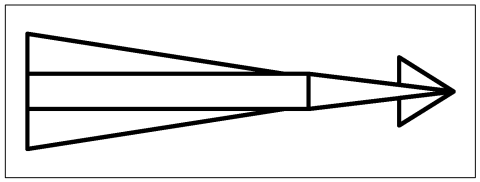

(c) Case 1a optimum geometry

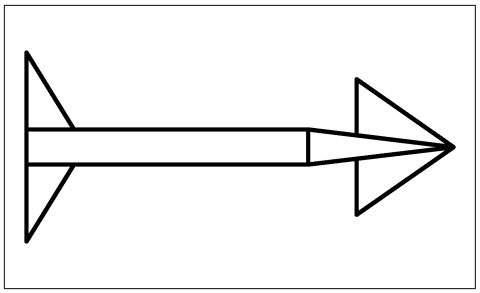

(d) Case 1b optimum geometry

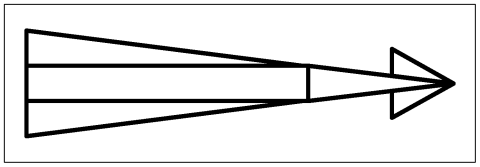

(e) Case 1c optimum geometry

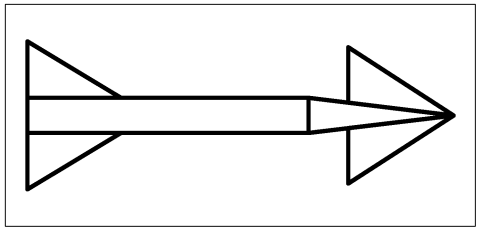

(f) Case 1d optimum geometry

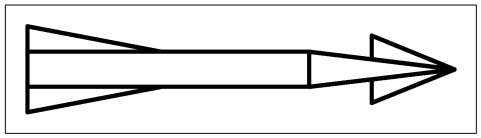

(g) Case 1e optimum geometry

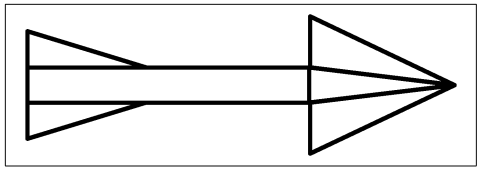

(h) Case 1f optimum geometry

Figure 4.1: Case 1 initial and optimum geometries

The optimum canard span design variable for all Case 1 runs was greater than 98% of the maximum value allowed by the side constraints. No other wing or canard design variable exhibited this trend. The optimum canard geometries maximize planform area while maintaining an optimum aspect ratio. This occurs so that the canards can allow for a wing geometry that produces as much lift as possible while keeping the projectile stable, thus maximizing the range. When designing projectiles of this scale, it is important to keep in mind that the maximum canard span is the limiting parameter. Two other important things to notice about the results from Table 4.4 are found in the wing aspect ratio and the launch angle. The runs which enforce constraint set 2 (Cases 1b, 1d, and 1f) showed a decrease in wing aspect ratio with increasing launch velocity. All wing and canard aspect ratios given in Chapter 4 are the aspect ratios as isolated from the missile body as given by:

$$A_{wing} = \frac{(b_{wing} - d)}{(0.5)\,(c_{wing})} \tag{4.1}$$

$$A_{canard} = \frac{\left(b_{canard} - \left(\frac{d}{ln} c_{canard}\right)\right)}{(0.5)\,(c_{canard})} \tag{4.2}$$

Case 1b, Case 1d, and Case 1f resulted in wing aspect ratios of 6.4, 2.4, and 1.2 respectively. Similarly, the canard aspect ratio of these cases followed the decreasing trend. Case 1b, 1d, and 1f had optimum canard aspect ratios of 2.31, 2.09, and 1.41 respectively. The runs which enforce side constraint set 1 (1a, 1c, and 1e) showed decreasing aspect ratio for an increase in launch velocity for the canards, but not for the wings. The canards exhibited aspect ratios of 2.00, 1.73, and 1.13, and the wings resulted in an aspect ratio of 0.62, 0.50, and 0.75 for Case 1a, 1c, and 1e respectively. The optimum launch angle did not deviate much from the initial value

of 55 degrees for all six runs. A more complete analysis of why the trends exist and how they compare to Case 2 and Case 3 can be found in Section 4.4

Trajectory plots for the six runs of Case 1 are provided in order to gain a better sense of the benefits of morphing to a single optimum design post-apogee. Trajectory plots for Case 1a through Case 1f are presented in Figure 4.2 through Figure 4.7 respectively. In each figure, the optimized trajectory is plotted alongside a baseline trajectory. The baseline trajectory is the resulting trajectory of a canard controlled gliding flight of the "low drag configuration" where no shape changes are occurring. The baseline flight simply launches the "low drag configuration" at a launch angle of 55 degrees, continues at zero lift conditions, and then flies in a canard controlled glide at maximum possible L/D post-apogee. The optimal flight trajectory for each run is plotted as blue and magenta circles. The blue circles represent the leg of the trajectory when the projectile is in the pre-apogee zero-lift configuration. The magenta circles represent the leg of the trajectory when the projectile has deployed its canards and wings to the optimal post-apogee configuration. The baseline trajectory used for comparison is plotted as a blue dot-dashed line.

Deployment of the optimum geometry wings and canards at apogee provides a substantial increase in range over a canard controlled glide of the baseline "low drag" configuration. The largest increase in range for the cases which enforce constraint set 1 was 36.8%, seen in Case 1a. The smallest increase in range was 31.5% for Case 1e. For the runs which enforce side constraint set 2, the largest increase in range was 98.6% for Case 1b and the smallest increase in range was Case 1f with 74.4%.

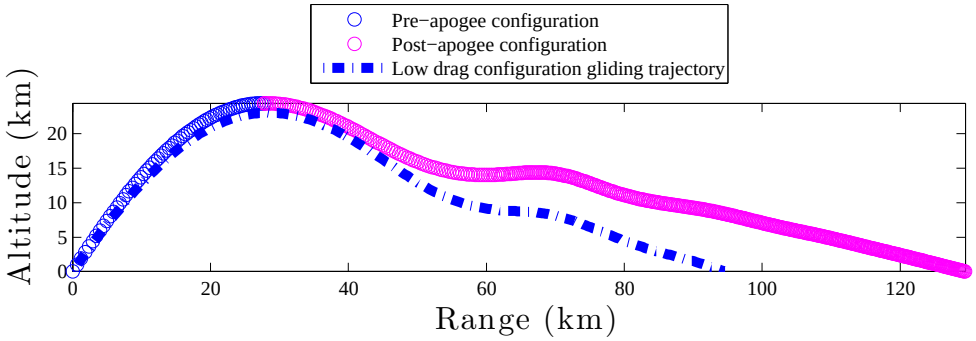

Figure 4.2: Case 1a optimal trajectory compared to low drag configuration baseline trajectory

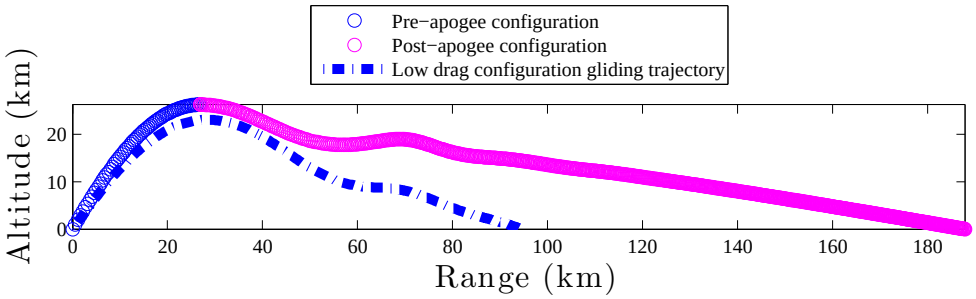

Figure 4.3: Case 1b optimal trajectory compared to low drag configuration baseline trajectory

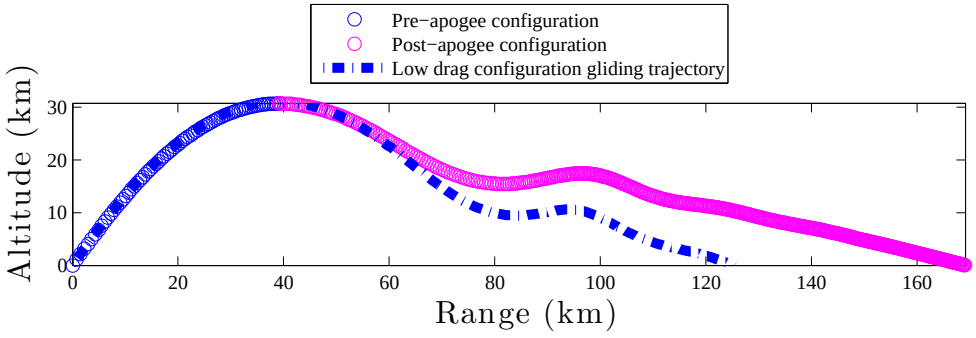

Figure 4.4: Case 1c optimal trajectory compared to low drag configuration baseline trajectory

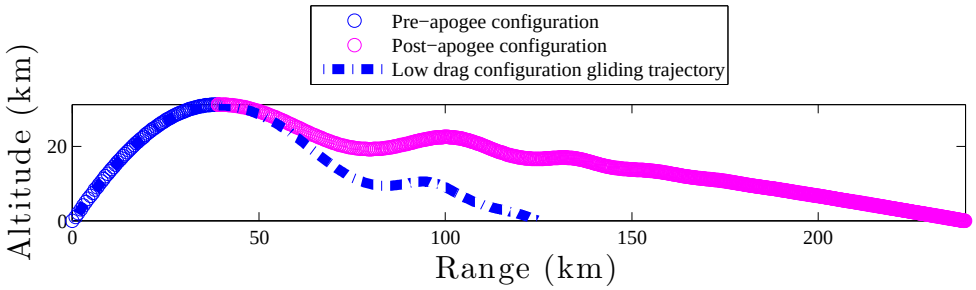

Figure 4.5: Case 1d optimal trajectory compared to low drag configuration baseline trajectory

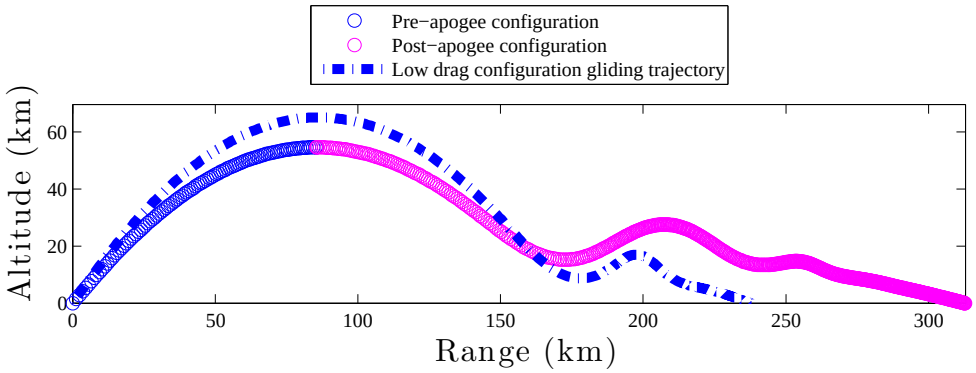

Figure 4.6: Case 1e optimal trajectory compared to low drag configuration baseline trajectory

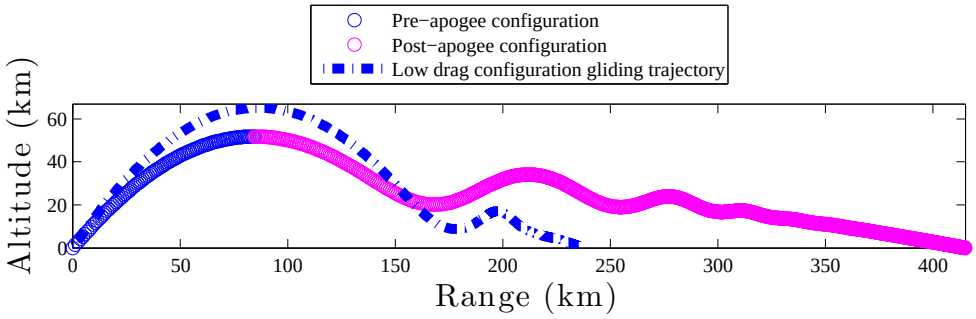

Figure 4.7: Case 1f optimal trajectory compared to low drag configuration baseline trajectory

4.2 Case 2 Optimum Configuration and Trajectory

The optimization results of the six runs for Case 2 are provided in this section. The set up of each run follows the nomenclature presented in Table 4.1, where the side constraints are explicitly listed in Table 4.5. For consistency, the two sets of side constraints for Configuration 1 and Configuration 2 were chosen to be the same as the Case 1 side constraints.

The initial designs given to the optimizer for each run along with the final optimized geometries are listed in Table 4.6. The initial designs for Case 2a through Case 2f were chosen to be the optimum geometries found in Case 1. The final designs and corresponding ranges found from the optimization are presented in Table 4.6. Full iteration histories of the range, mesh size, constraints, and design variables can be found in Appendix A.

Table 4.5: Case 2 optimization design variable side constraints

Design variable	Side constraints set 1	Side constraints set 2
Configuration 1 wing span	88 mm $\leq b_{wing_{c1}} \leq$ 970 mm	88 mm $\leq b_{wing_{c1}} \leq$ 1,940 mm
Configuration 1 wing root chord	80 mm $\leq c_{wing_{c1}} \leq$ 640 mm	80 mm $\leq c_{wing_{c1}} \leq$ 640 mm
Configuration 1 canard span	81 mm $\leq b_{canard_{c1}} \leq$ 155 mm	81 mm $\leq b_{canard_{c1}} \leq$ 310 mm
Configuration 1 canard root chord	10 mm $\leq c_{canard_{c1}} \leq$ 330 mm	10 mm $\leq c_{canard_{c1}} \leq$ 330 mm
Launch angle	$26° \leq \kappa \leq 75°$	$26° \leq \kappa \leq 75°$
Configuration 2 wing span	88 mm $\leq b_{wing_{c2}} \leq$ 970 mm	88 mm $\leq b_{wing_{c2}} \leq$ 1,940 mm
Configuration 2 wing root chord	80 mm $\leq c_{wing_{c2}} \leq$ 640 mm	80 mm $\leq c_{wing_{c2}} \leq$ 640 mm
Configuration 2 canard span	81 mm $\leq b_{canard_{c2}} \leq$ 155 mm	81 mm $\leq b_{canard_{c2}} \leq$ 310 mm
Configuration 2 canard root chord	10 mm $\leq c_{canard_{c2}} \leq$ 330 mm	10 mm $\leq c_{canard_{c2}} \leq$ 330 mm

Table 4.6: Case 2 initial and optimal designs for maximizing projectile range (measurements in mm unless otherwise specified)

Case number	Design	$b_{wing_{c1}}$	$c_{wing_{c1}}$	$b_{canard_{c1}}$	$c_{canard_{c1}}$	κ	$b_{wing_{c2}}$	$c_{wing_{c2}}$	$b_{canard_{c2}}$	$c_{canard_{c2}}$	Range (km)
Case 2a	Initial	260	584	154	124	57.15°	260	584	154	124	129.42
	Optimum	966	584	154	124	57.15°	260	584	154	124	129.62
Case 2b	Initial	428	108	307	220	60°	428	108	307	220	187.9
	Optimum	428	108	307	220	60°	428	444	307	124	191.13
Case 2c	Initial	238	626	155	140	54.61°	238	626	155	140	169.10
	Optimum	613	178	155	268	54.61°	227	626	155	140	169.63
Case 2d	Initial	335	213	309	240	55.27°	335	213	309	240	239.36
	Optimum	1447	437	218	240	55.27°	335	213	309	240	239.47
Case 2e	Initial	194	304	152	188	50.08°	194	304	152	188	312.88
	Optimum	900	416	152	188	50.08°	194	304	152	188	313.99
Case 2f	Initial	243	269	310	328	48.72°	243	269	310	328	414.99
	Optimum	335	157	309	200	48.72°	243	269	310	328	424.84

Trajectory plots for the six runs of Case 2 are provided in order to gain a better sense of the benefits of swapping between two optimized geometries post-apogee. Trajectory plots for Case 2a through Case 2f are presented in Figure 4.8 through Figure 4.13 respectively. In each figure, the Case 2 optimized trajectory is plotted. The optimal flight trajectory for each run is plotted as blue, magenta, and black circles. The blue circles represent the leg of the trajectory when the projectile is in the pre-apogee zero-lift configuration. The magenta circles represent the leg of the trajectory when the projectile is in post-apogee flight using the "Configuration 1" geometry. The black circles represent the leg of the trajectory when the projectile is post-apogee flight using the "Configuration 2" geometry.

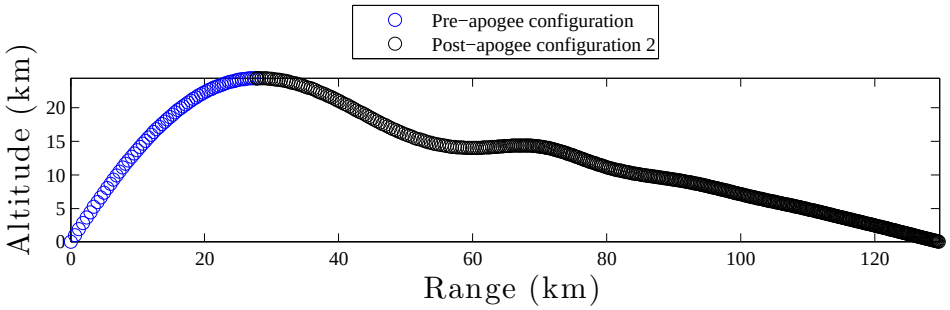

Figure 4.8: Case 2a optimal trajectory

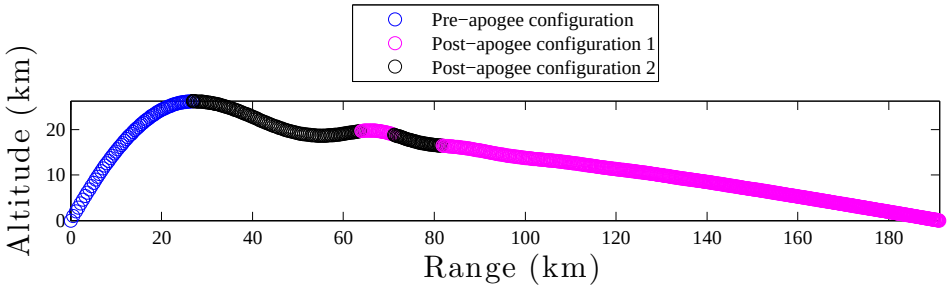

Figure 4.9: Case 2b optimal trajectory

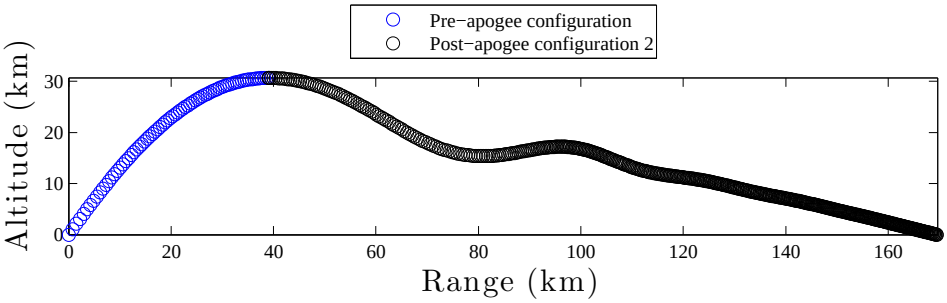

Figure 4.10: Case 2c optimal trajectory

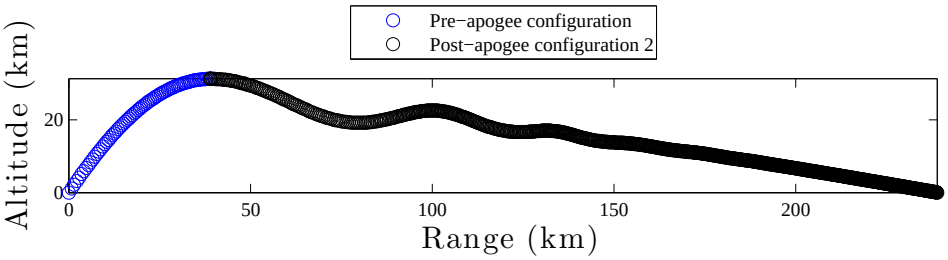

Figure 4.11: Case 2d optimal trajectory

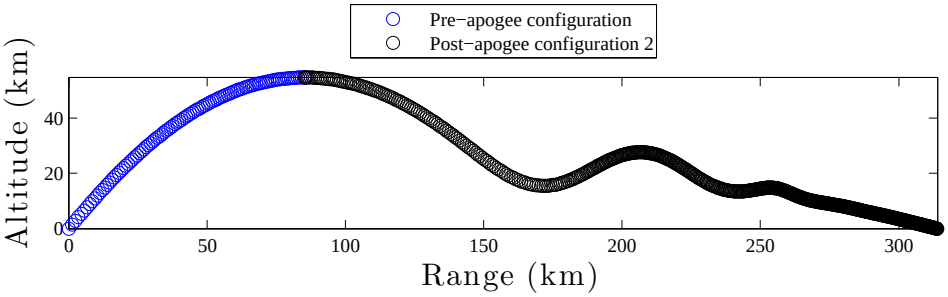

Figure 4.12: Case 2e optimal trajectory

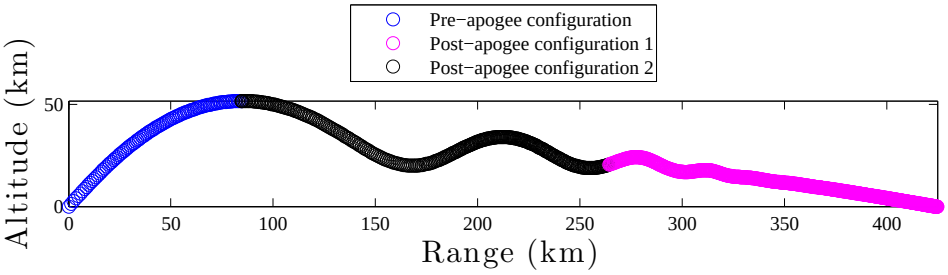

Figure 4.13: Case 2f optimal trajectory

For Case 2b and Case 2f the trajectory plots show that the pattern search optimization method was successful. An optimum Configuration 1 and Configuration 2 was found such that swapping between them throughout the trajectory resulted in an increase in range over that of their Case 1 counterparts. Geometric representations of the initial and optimum geometries for Case 2b and 2f are illustrated in Figure 4.14. For Case 2f, the resulting set of dual geometries included one configuration with low aspect ratio wings and canards and one configuration containing high aspect ratio wings and canards. Configuration 1 had wings with an aspect ratio of 3.5 and canards with an aspect ratio of 2.6. Configuration 2 had wings with aspect ratio of 1.2 and canards of aspect ratio of 1.4.

As seen in Figure 4.15, the optimum design found for Case 2f is one where each of the two configurations are deployed while the projectile is gliding in a particular freestream Mach regime. Configuration 1 is deployed during the subsonic and transonic phases of the trajectory where $M_\infty \leq 1.1$. Configuration 2 is deployed during the supersonic phase of the trajectory where $M_\infty > 1.1$. This holds true at all altitudes. This means altitude changes did not play a significant role. Using these two configurations during their respective freestream Mach number regimes intuitively makes sense. Configuration 2 has lower aspect ratio wings and canards, rendering better wave drag characteristics for supersonic flight. Configuration 1 has higher aspect ratio wings and canards which produces a better lift to drag ratio for subsonic flight. Deploying these two optimized geometries at their given freestream Mach regimes over the entire trajectory, increased the range of the projectile by 78.5% over the baseline trajectory.

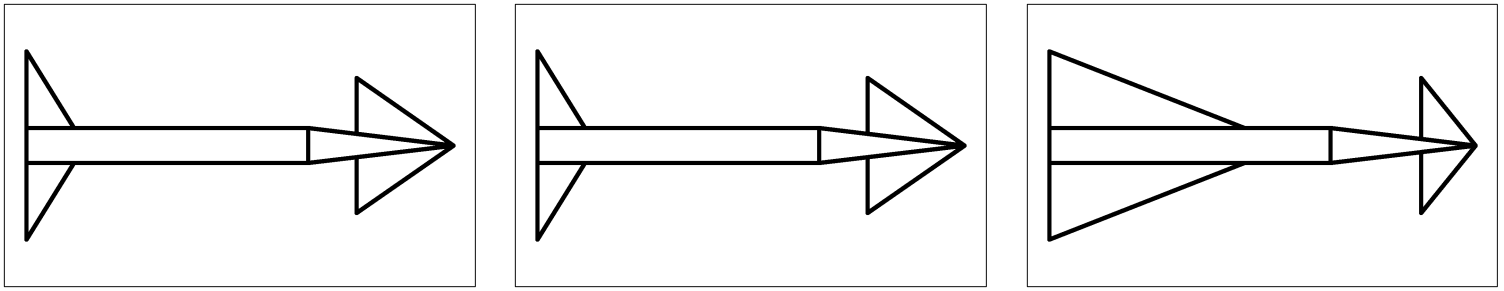

(a) Case 2b initial geometry (b) Case 2b optimum geometry c1 (c) Case 2b optimum geometry c2

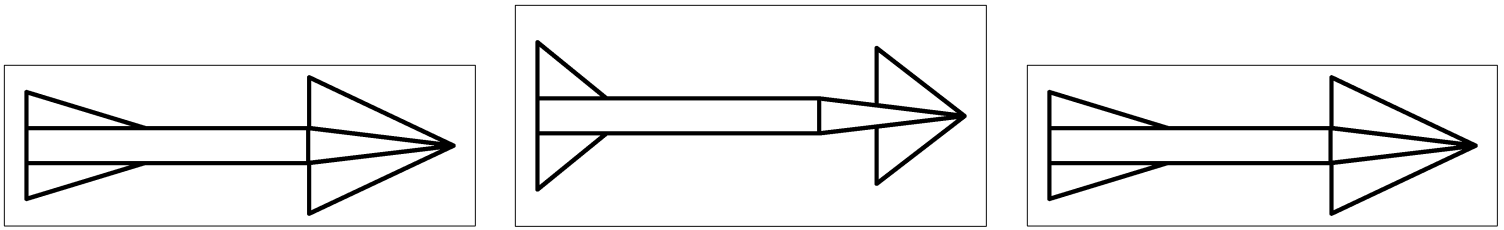

(d) Case 2f initial geometry (e) Case 2f optimum geometry c1 (f) Case 2f optimum geometry c2

Figure 4.14: Case 2b and 2f initial and optimum geometries

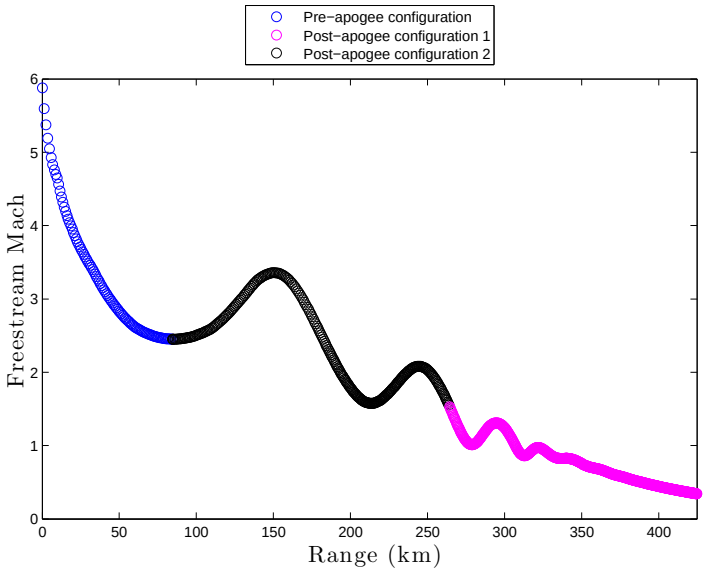

Figure 4.15: Case 2f optumum trajectory freestream Mach number vs. range

For Case 2b, where the maximum freestream Mach number experienced during the trajectory is significantly less than that of Case 2f, a slightly different dual set of configurations was found as the optimum design. The Configuration 1 wing aspect ratio of 6.4 is significantly larger than the Configuration 2 wing aspect ratio of 1.6. The canards have a less dramatic difference in aspect ratio between the two configurations, yet now the opposite relationship exists. The Configuration 1 canard aspect ratio of 2.3 is less than the Configuration 2 canard aspect ratio of 4.5. Similar to what was found in Case 2f, Figure 4.16 shows that each configuration was designated for a particular Mach regime. Configuration 2 was used solely for transonic and low supersonic flight at all altitudes where $M_\infty > 0.9$. Configuration 1 was used for subsonic flight at all altitudes where $M_\infty \leq 0.9$. Deploying the two optimized geometries at their given freestream Mach regimes over the entire trajectory, increased the range of the projectile for Case 2b by 102% over the baseline

trajectory. A more complete analysis of how the optimum geometries compare to Case 1 and Case 3 and why the certain aspect ratio trends exist can be found in Section 4.4

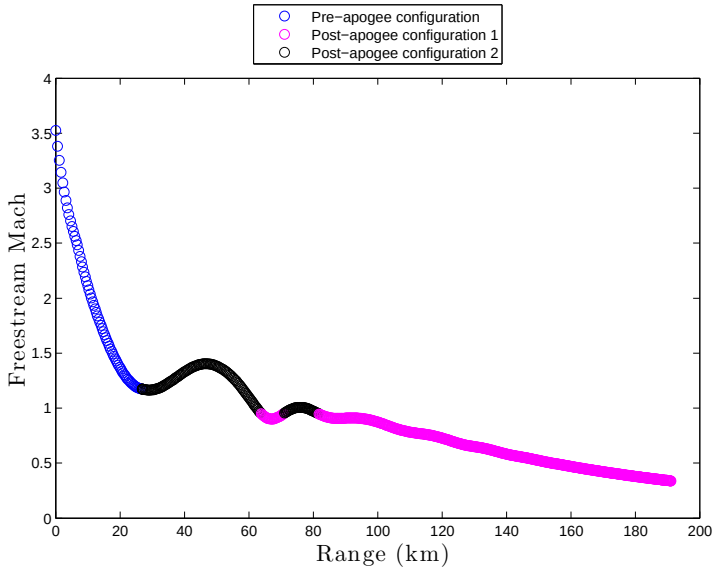

Figure 4.16: Case 2b optumum trajectory freestream Mach number vs. range

For Case 2a, 2c, 2d, and 2e, the optimum trajectory post-apogee only used one configuration out of the two, therefore no dual configuration morphing occurred. For these four runs, the configuration geometry that is used (Configuration 2) is practically the same as the initial design. The very slight differences in range are due to the minor differences in the penalty parameter at the time of convergence. This means the optimizer was unable to find a candidate design which would increase the range over what was found in Case 1. As seen in Case 1b, Case 1f, and all of Case 3, a Configuration 1 should exist that would increase the range.

The pattern search optimization method is set to decrease the current mesh size by half, when an iteration was unable to find a design which increases the

objective function. The initial mesh size dictates that a poll for better designs would increment each design variable by 20% of the difference between the upper and lower limits of the side constraints. For example, if the side constraint states that the wing span can vary between 1mm and 11mm, a mesh size of 20% would mean the polling taking place at that iteration would increment the wing span variable ±2mm. If the mesh started at 20% and no design was found which increases the range (i.e. an unsuccessful poll), the next iteration would search using a 10% increment. If the poll was successful, the mesh increment at the next iteration would be 40%, and so on. This method tends to work the best for most optimization problems, yet by no means guarantees a global maximum.

For the design space being explored in Case 2, when starting from these specific initial designs, it was found that the "areas" of better solutions within the design hyperspace were too small for the pattern search algorithm to find them in all six runs. This may be a product of the fact that the projectile does not experience enough of a range of Mach number altitude variations and hence the increment in range for a swapping geometry is minimal. If, for instance, the projectile being optimized happened to be a powered cruise missile, the range of freestream Mach numbers experienced during the flight would be more extreme for longer periods of time. This would open up the design space making it easier for the pattern search technique to find two different geometries to swap between and therefore increasing the range. Alternatively, a way to remedy this problem would be to customize the procedure for updating the mesh size or even use a different zero-th order method all together (Genetic Algorithms or Simulated Annealing). Another

possible explanation for the results of these four cases would be an existence of multiple local maxima within the design space. This concept is discussed further in Section 4.3.

Even though the pattern search method does not guarantee global optimum solutions, it is important to note that the global optimum solution may not be the "best" solution. Local optima may just as well satisfy the mission requirements or even be more beneficial than the global optimum. This happens because optimizers, by default, put no weight on off-design conditions. For example, the global optimum for the type of problem studied in this work is likely to be extremely sensitive to angle of attack perturbations. Meaning, a slight wind gust in the pitch plane may cause the projectile to go unsteady, causing catastrophic failure. Whereas, a local optimum design, even though it results in a slightly shorter range, may be more robust to such off-design conditions while still fitting the mission requirements. Therefore, it is important to never write off any of the local optimums. If possible, the entire design space should be analyzed and a sensitivity analysis should be completed at some time during the preliminary design phase.

4.3 Case 3 Optimum Configuration and Trajectory

The optimization results for Case 3 are provided in this section. The optimization process for Case 3 differs slightly from that of Cases 1 and 2. As described in Section 3.4, a gradient based optimization scheme was used to find a design that gives a maximum lift to drag ratio for a given Mach number and altitude while satisfying all the specified constraints. This optimization is then repeated at a range of

Mach number and altitude values. This essentially builds a two dimensional table of optimum designs as a function of altitude and Mach number. This table of designs is then input to the aeroprediction code rendering two dimensional look-up tables of lift and drag coefficients. POST then reads these input tables and simulates the trajectory of a continuously morphing optimized projectile for a given launch angle and launch velocity.

Two tables of optimum designs were generated as functions of Mach number and altitude. One for each set of constraints listed in Table 4.7. The resulting two dimensional tables of designs are labeled as Table 4.8 and Table 4.9 for constraint set 1 and set 2 respectively. Finding an optimum trajectory for the six runs outlined in Table 4.1 was found by completing the following steps. First, use Table 4.8 if following constraint set 1 or Table 4.9 if following constraint set 2 and convert the table into lift and drag coefficients as a function of Mach number and altitude using the aeroprediction code. Second, input these lift and drag tables into POST along with the value of the initial launch velocity. The last step is to find the optimum launch angle. This was done by simply simulating a series of trajectories by parametrically changing the value of the launch angle until a maximum range is found.

Gradient based optimizers can only guarantee a local optimum solution. Therefore, if the design space has multiple maxima, different optimum designs may be found for different initial designs. In order to increase the chances of obtaining a true global maximum for the problem studied in this thesis, Case 3 employed a multistart method. To accomplish this, 8 initial designs vectors were created by

randomly generating design variable values that satisfy the side constraints. The MATLAB parallel processing toolbox was used in order to simultaneously start the optimization from the 8 randomized initial designs. At the completion of each optimization, the candidate with the highest lift to drag ratio was said to be the global optimum and was recorded in the final table of designs (Table 4.8 and Table 4.9). A list of the final design tables and corresponding ranges from Case 3a thorough Case 3f is given in Table 4.10. Due to the large quantity of optimization iteration history data generated from Case 3, only one example of the objective function iteration history is provided in Appendix A.

Table 4.7: Case 3 optimization design variable side constraints

Design variable	Side constraints set 1	Side constraints set 2
Wing span	88 mm $\leq b_{wing} \leq$ 970 mm	88 mm $\leq b_{wing} \leq$ 1,940 mm
Wing root chord	80 mm $\leq c_{wing} \leq$ 640 mm	80 mm $\leq c_{wing} \leq$ 640 mm
Canad span	81 mm $\leq b_{canard} \leq$ 155 mm	81 mm $\leq b_{canard} \leq$ 310 mm
Canard root chord	10 mm $\leq c_{canard} \leq$ 330 mm	10 mm $\leq c_{canard} \leq$ 330 mm
Body angle of attack	$-0.01^\circ \leq \alpha \leq 45^\circ$	$-0.01^\circ \leq \alpha \leq 45^\circ$
Wing angle of attack	$-0.01^\circ \leq \psi \leq 45^\circ$	$-0.01^\circ \leq \psi \leq 45^\circ$
Canard deflection angle	$-0.01^\circ \leq \delta \leq 50^\circ$	$-0.01^\circ \leq \delta \leq 50^\circ$

Table 4.8: Case 3 optimal designs as functions of Mach number and altitude for constraint set 1 (measurements in mm unless otherwise specified)

h	M_∞	b_{wing}	c_{wing}	b_{canard}	c_{canard}	α	ψ	δ	$\frac{L}{D}$
0 km	0.01	290	639	155	141	8.33°	2.90°	3.81°	3.69
	0.8	409	80	155	121	8.24°	1.51°	2.12°	3.99
	0.9	437	80	155	109	8.03°	1.15°	2.39°	4.02
	1.0	299	639	155	98	8.07°	2.77°	3.27°	3.79
	1.1	295	639	155	98	8.97°	2.81°	2.92°	3.55
	2.0	281	634	155	170	9.76°	2.63°	1.22°	3.74
	3.0	254	631	155	202	8.94°	2.57°	1.35°	3.84
	5.0	212	496	155	262	8.27°	2.69°	1.66°	3.72
10 km	0.01	370	80	155	142	8.81°	2.17°	2.38°	3.64
	0.8	400	80	155	120	8.05°	1.55°	2.13°	4.02
	0.9	362	80	155	109	8.22°	1.67°	2.27°	3.89
	1.0	291	640	155	94	8.80°	3.12°	3.19°	3.55
	1.1	292	638	155	98	9.68°	3.02°	2.91°	3.34
	2.0	269	637	155	171	10.31°	2.99°	1.28°	3.49
	3.0	245	577	155	203	9.41°	2.89°	1.47°	3.57
	5.0	204	448	155	263	9.01°	3.16°	1.55°	3.44
20 km	0.01	315	275	155	148	9.28°	2.27°	2.66°	3.51
	0.8	422	80	155	126	8.57°	1.49°	2.29°	3.81
	0.9	347	153	155	114	8.56°	1.75°	2.77°	3.66
	1.0	274	301	155	96	8.63°	3.06°	3.77°	3.25
	1.1	282	615	155	100	10.28°	3.35°	2.93°	3.09
	2.0	257	575	155	173	11.38°	3.47°	1.07°	3.18
	3.0	231	470	155	210	10.18°	3.45°	1.54°	3.22
	5.0	199	414	155	265	10.10°	3.67°	1.34°	3.09
30 km	0.01	278	639	155	145	10.65°	3.73°	3.87°	2.97
	0.8	283	639	155	124	9.80°	3.39°	3.31°	3.30
	0.9	298	639	155	113	9.57°	3.09°	3.73°	3.23
	1.0	308	639	155	88	10.04°	3.19°	3.57°	3.11
	1.1	294	602	155	96	11.40°	3.17°	2.33°	2.94
	2.0	245	322	155	187	11.48°	3.76°	1.35°	3.01
	3.0	256	219	153	220	10.59°	4.16°	2.18°	2.97
	5.0	194	381	155	268	10.92°	4.37°	1.93°	2.75
40 km	0.01	277	299	153	180	10.93°	3.51°	5.35°	2.37
	0.8	260	81	155	127	10.55°	4.35°	2.31°	2.92
	0.9	275	80	155	114	10.61°	3.59°	2.52°	2.89
	1.0	264	638	155	82	10.53°	4.49°	3.84°	2.80
	1.1	267	638	155	99	11.23°	4.15°	3.65°	2.70
	2.0	268	639	155	178	13.72°	3.83°	1.21°	2.65
	3.0	254	639	155	217	12.67°	3.50°	1.69°	2.71
	5.0	217	555	155	269	11.71°	3.44°	2.68°	2.59

Table 4.9: Case 3 optimal designs as functions of Mach number and altitude for constraint set 2 (measurements in mm unless otherwise specified)

h	M_∞	b_{wing}	c_{wing}	b_{canard}	c_{canard}	α	ψ	δ	$\frac{L}{D}$
0 km	0.01	556	80	310	248	5.79°	1.62°	0.99°	5.49
	0.8	622	80	310	183	6.16°	1.18°	0.12°	6.14
	0.9	604	80	310	157	5.21°	1.06°	1.04°	6.30
	1.0	427	350	310	155	5.91°	1.91°	0.43°	5.85
	1.1	391	318	310	165	5.31°	2.17°	1.42°	5.48
	2.0	326	359	310	289	6.29°	2.30°	0.21°	5.29
	3.0	267	500	307	330	6.17°	2.67°	0.33°	5.13
	5.0	222	515	310	330	6.84°	2.94°	0.75°	4.42
10 km	0.01	522	80	310	241	5.66°	1.83°	1.18°	5.38
	0.8	600	80	310	173	5.42°	1.26°	0.89°	6.08
	0.9	567	80	310	154	5.64°	1.24°	0.78°	6.03
	1.0	406	312	310	149	6.48°	2.23°	0.18°	5.50
	1.1	358	239	310	165	5.88°	2.61°	1.03°	5.17
	2.0	311	279	310	290	6.80°	2.73°	0.04°	4.94
	3.0	258	407	306	330	6.55°	3.02°	0.38°	4.75
	5.0	218	486	310	330	7.51°	3.26°	0.59°	4.06
20 km	0.01	506	80	310	256	6.03°	1.98°	1.00°	5.22
	0.8	599	80	310	169	6.05°	1.34°	0.61°	5.88
	0.9	635	80	309	153	4.72°	1.03°	2.01°	5.75
	1.0	392	260	310	137	4.43°	2.58°	2.76°	5.14
	1.1	375	217	310	164	6.20°	2.58°	1.33°	4.77
	2.0	305	262	310	300	7.36°	3.08°	0.14°	4.50
	3.0	253	366	305	330	7.15°	3.47°	0.48°	4.26
	5.0	214	455	310	330	8.30°	3.78°	0.73°	3.62
30 km	0.01	441	80	310	256	7.66°	3.06°	0.75°	4.19
	0.8	496	80	310	200	6.22°	2.12°	1.39°	4.85
	0.9	364	639	310	174	6.41°	3.35°	1.49°	4.79
	1.0	427	640	310	134	6.27°	2.91°	1.73°	4.82
	1.1	425	602	310	162	7.58°	2.54°	0.82°	4.54
	2.0	348	331	310	289	7.45°	2.53°	0.55°	4.38
	3.0	248	330	305	330	8.05°	4.01°	0.25°	3.83
	5.0	210	436	310	330	9.31°	4.34°	0.69°	3.20
40 km	0.01	484	225	292	238	6.76°	2.66°	5.58°	3.15
	0.8	410	80	310	195	7.71°	3.39°	0.85°	4.15
	0.9	401	80	310	164	7.40°	3.19°	1.16°	4.24
	1.0	361	225	310	128	7.00°	3.66°	1.44°	4.24
	1.1	340	194	310	162	7.43°	3.54°	1.02°	4.05
	2.0	285	633	310	295	8.65°	4.29°	0.58°	3.71
	3.0	258	638	305	330	8.98°	3.91°	0.31°	3.58
	5.0	219	555	310	330	9.64°	4.03°	1.25°	3.08

Table 4.10: Case 3 optimum trajectory results

Case name	Table of optimum designs	Optimum launch angle	Range (km)
Case 3a	Table 4.8	58°	136.86
Case 3b	Table 4.9	60°	199.37
Case 3c	Table 4.8	55°	178.39
Case 3d	Table 4.9	55°	253.07
Case 3e	Table 4.8	50°	334.95
Case 3f	Table 4.9	47°	439.73

Tables 4.8 and 4.9 each give optimum designs for 40 Mach-altitude combinations. The altitudes ranging from 0km to 40km in 10km increments and the Mach number values ranging from subsonic, transonic, and supersonic. Having an optimum design at a variety of conditions give the opportunity to examine the patterns that exist within the data. Trends of how wing aspect ratio, canard aspect ratio, and lift to drag ratio vary with altitude and Mach number are investigated here. Furthermore, identifying where the Case 1 and Case 2 optimum designs fit within these patterns will give some insight into why these shapes give the longest range for single and dual geometry morphing. Therefore, a comparison between all cases will be discussed in Section 4.4.

The optimum canard span found in Case 1 and Case 2 was practically equal to the upper limit for all runs. As seen in the tables of designs for Case 3, this fact remains the same. The canard span is the limiting design variable in the optimization. Maximizing the upper limit of the canard span, while minimizing canard wake interference effects, should be a main focus of morphing projectile preliminary design. Figure 4.17 shows how the canard aspect ratio changes as a function of freestream Mach number and altitude for both sets of constraints.

The plots for side constraint set 1 and side constraint set 2 exhibit similar trends. For constraint set 1, the aspect ratio starts at a value of approximately 1.5 for $M_\infty = 0.01$ and increases slowly for increasing subsonic Mach numbers. The aspect ratio then exhibits a sharp increase while in the transonic range up until a value of about 3 at a freestream Mach number of unity. For increasing supersonic freestream Mach number, the canard aspect ratio decreases while leveling off around

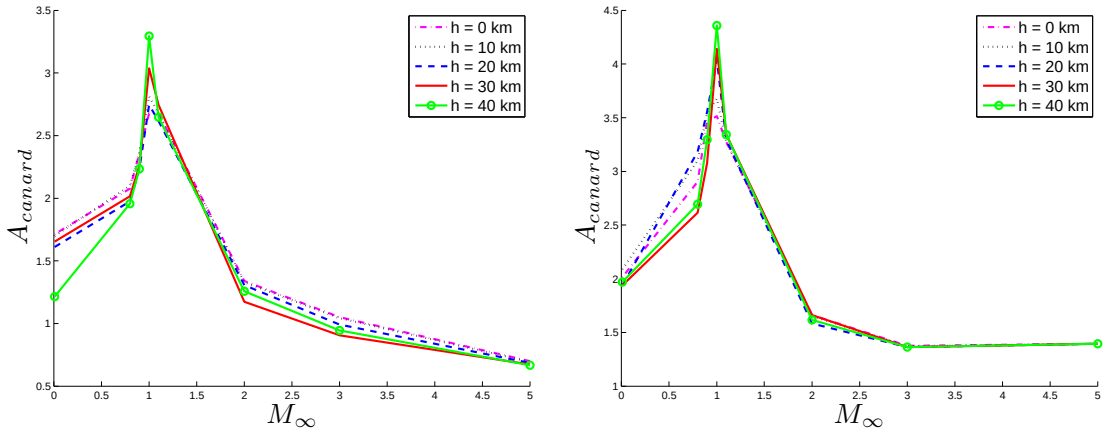

(a) Constraint set 1

(b) Constraint set 2

Figure 4.17: Case 3 canard aspect ratio as a function of freestream Mach number

an aspect ratio of 1. The trend for constraint set 2 follows that of constraint set 1, yet the specific values are all larger by and increment of about 0.5. For constraint set 2, the aspect ratio levels off more rapidly in the supersonic Mach range than side constraint set 1. In general, the variation in the curves due to altitude changes are limited.

Figure 4.18 shows two plots illustrating the variation of wing aspect ratio with altitude and freestream Mach number. The plots between side constraint set 1 and side constraints set 2 for the wing aspect ratio do not mirror one another as closely as what was seen in Figure 4.17. Similar trends exist for most of the altitude curves from around $M_\infty = 1$ to $M_\infty = 5$. The curves for constraint set 2 at low subsonic freestream Mach numbers show that as the altitude increases from 0km to 40km the aspect ratio decreases over a large range of values (from 12 to 4). Constraint set 1, however, does not exhibit this trend. For all subsonic and transonic Mach numbers, it is hard to distinguish if a comprehensible pattern exists.

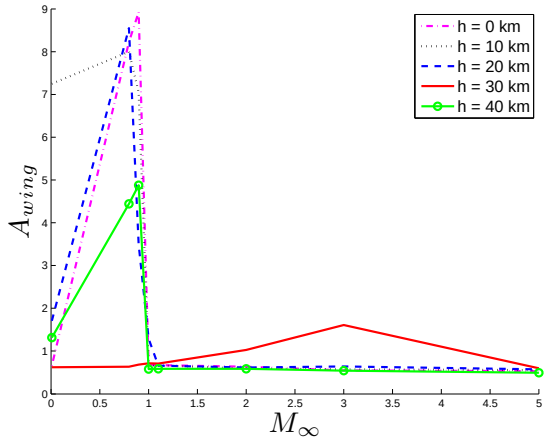

(a) Constraint set 1

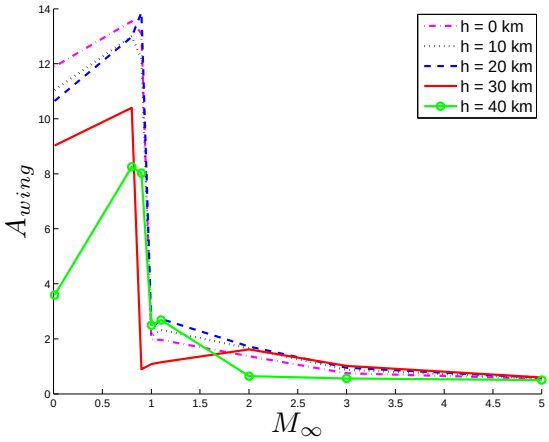

(b) Constraint set 2

Figure 4.18: Case 3 wing aspect ratio as a function of freestream Mach number

To rule out any suspicion of human or logic error, refer to the lift to drag ratio relationship shown in Figure 4.19. Here the mirroring between side constraint set 1 and set 2 is seen once again. A clear consistent trend between lift to drag ratio and both altitude and Mach number exists. There are several explanations for these results including but not limited to the following. These designs may be the global optimum. A pattern is not noticeable due to a limited resolution in the altitude points. If there were more curves in increments smaller than 10km, a more clear pattern may exist. Another possibility would be that the optimum

designs found for these points are local maxima. This could mean that a bifurcated design space exists at the subsonic Mach-altitude conditions, where a maximum exists at a large wing aspect ratio and at a smaller aspect ratio with only minor differences in lift to drag ratio. To check this, a dense multistart optimization should be conducted. Analyzing all these results would more likely capture any local maxima, and hopefully pinpoint the global maximum. A further investigation into this design space is necessary to reveal the true nature of the optimum geometry found in this study.

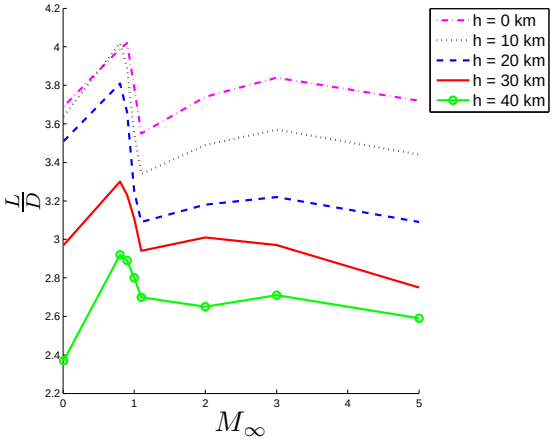

(a) Constraint set 1

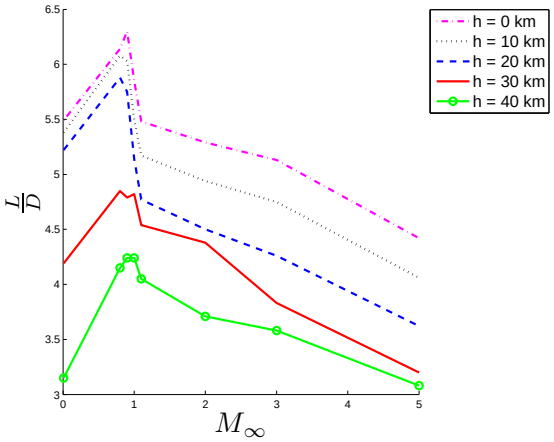

(b) Constraint set 2

Figure 4.19: Case 3 $\frac{L}{D}$ as a function of freestream Mach number

Trajectory plots for all six Case 3 runs are provided in order to gain a better sense of the benefits of continuously morphing to an optimum design at any instant post-apogee. Trajectory plots for Case 3a through Case 3f are presented in Figure 4.20 through Figure 4.25 respectively. In each trajectory plot, the optimized trajectory is plotted alongside the corresponding Case 2 trajectory. The optimal flight trajectory for each run is plotted as blue and red circles. The blue circles represent the leg of the trajectory when the projectile is in the pre-apogee zero-lift configuration. The red circles represent the leg of the trajectory when the projectile is continually morphing to an optimized geometry as dictated by the results in Table 4.8 and Table 4.9. The Case 2 trajectory is plotted as a blue dot-dashed line. The x and y axis are not of equal scale. This was done to help see the differences in the trajectories more clearly.

Continuous morphing pose-apogee provides a modest increase in range over the Case 1 and Case 2 morphing strategies. The largest increase in range over the baseline case for the cases which enforce constraint set 1 was 44.6%, seen in Case 3a. The smallest increase in range was 40.8% for Case 3e. For the runs which enforce side constraint set 2, the largest increase in range was 110.7% for Case 3b and the smallest increase in range was Case 3f with 84.8%.

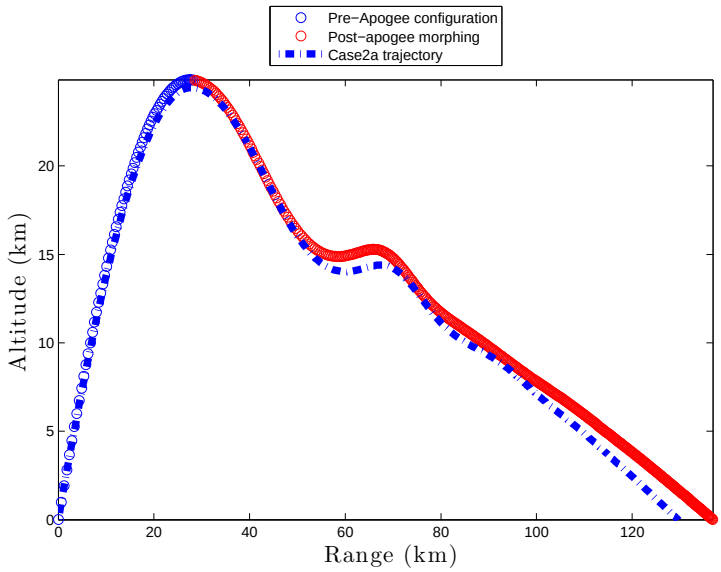

Figure 4.20: Case 3a optimal trajectory compared to low drag configuration baseline trajectory

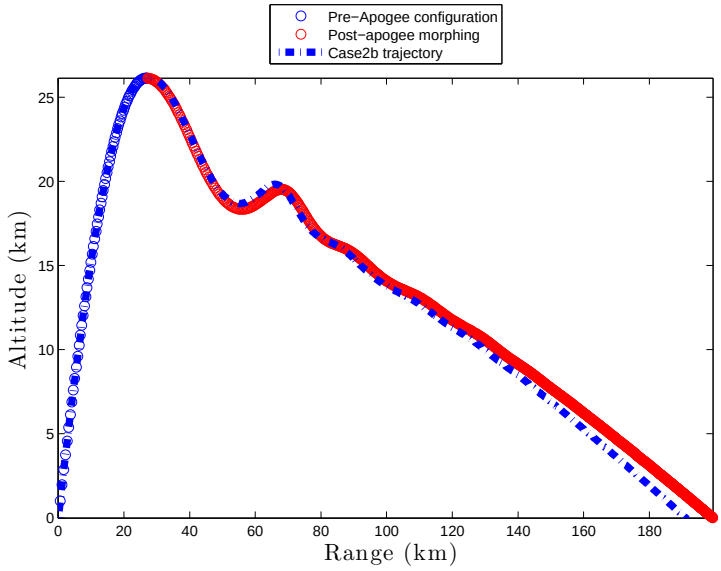

Figure 4.21: Case 3b optimal trajectory compared to low drag configuration baseline trajectory

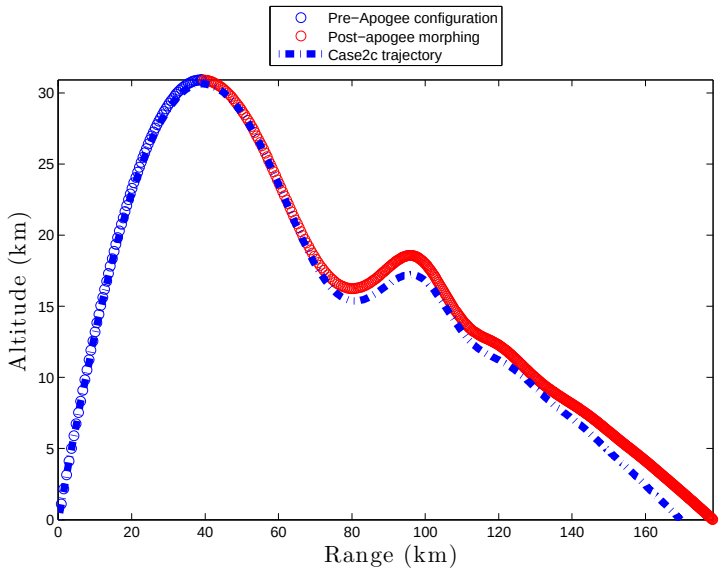

Figure 4.22: Case 3c optimal trajectory compared to low drag configuration baseline trajectory

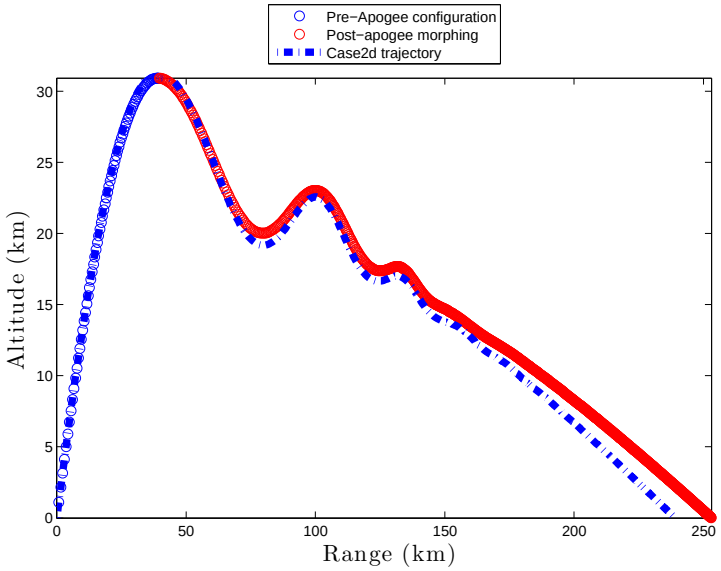

Figure 4.23: Case 3d optimal trajectory compared to low drag configuration baseline trajectory

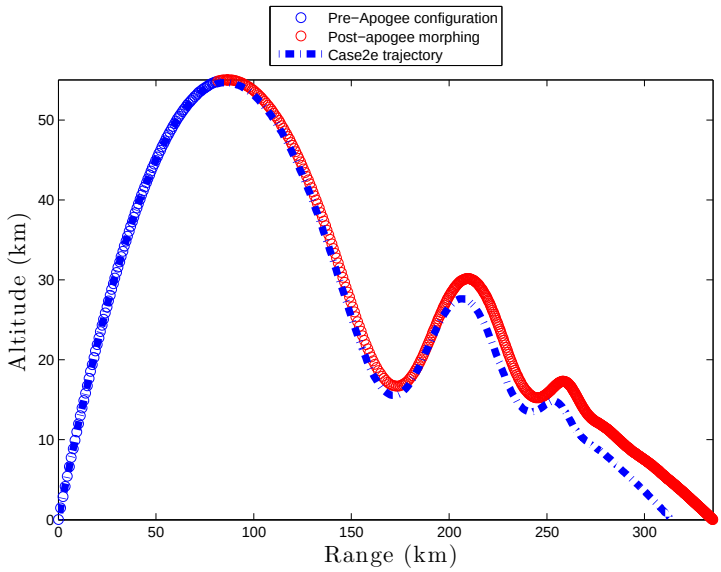

Figure 4.24: Case 3e optimal trajectory compared to low drag configuration baseline trajectory

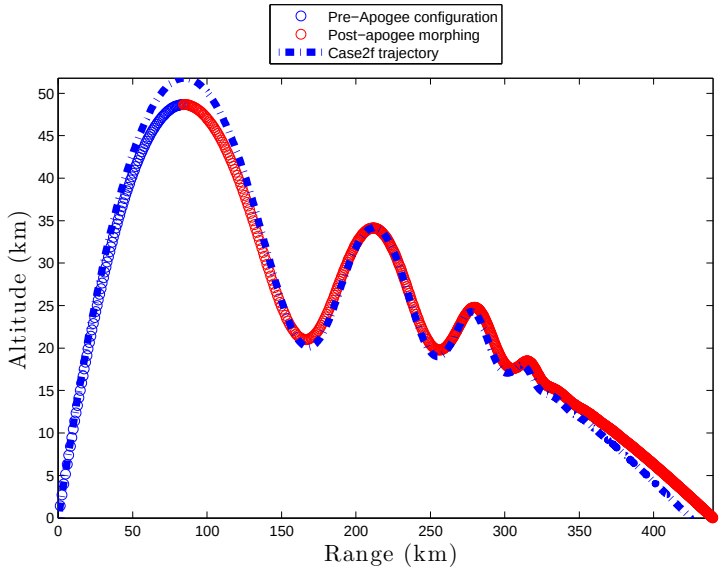

Figure 4.25: Case 3f optimal trajectory compared to low drag configuration baseline trajectory

4.4 Comparison of Results Between Cases

Case 3 provides data for a continuously morphing projectile flying through a range of Mach numbers and altitudes. Given the launch velocities and launch angles tested, Case 3a through Case 3f did not experience vast differences in freestream Mach number throughout the trajectory. Even so, the structure of the optimization methodology for Case 3 led to the calculation of data for 40 Mach-altitude points (see Tables 4.8 and 4.9), even if most of those points were not utilized. The calculation of all the extra data points was not done in vain.

Figures were produced which show how the optimum design changes as a function of altitude and freestream Mach number (see Figures 4.17 and 4.18). These figures can be used to analyze the results from Case 1 and Case 2 and is done so in Figure 4.26 through Figure 4.31. In each plot, Case 1 or Case 2 results are shown in the foreground of the figure. The Case 3 counterpart is plotted in grey as a background of the figure used for comparison and therefore is not referenced in the figure legend.

Comparisons of the canard aspect ratio of the optimum designs for Case 1 is compared to that of Case 3 in Figure 4.26 and 4.27. The single geometry morphing scheme for Case 1 renders a single aspect ratio for each run. The trends between constraint sets and runs are explained in Section 4.1. When superimposing these results onto the results from Case 3, it is seen that the Case 1 optimum designs exist at an aspect ratio that minimizes the off design penalties paid by differing from the Case 3 curves for the Mach numbers experienced during the trajectory. For example,

the trajectory for Case 1a experienced freestream Mach numbers varying between 0 and 2.0 with the majority of the trajectory in the subsonic range. A canard aspect ratio of around 2.0 best fits the Case 3 curve within this Mach range. For Case 2e, the Mach number range extends all the way to 5. A "best" fit for the Case 3 curves is therefore lower at a value of about 1.1. The illustration in Figure 4.26 and Figure 4.27 is best described qualitatively. The optimum designs for Case 1 minimize the off-design lift to drag ratio penalty paid by using one design over the range of freestream conditions rather than the best designs outlined by Case 3.

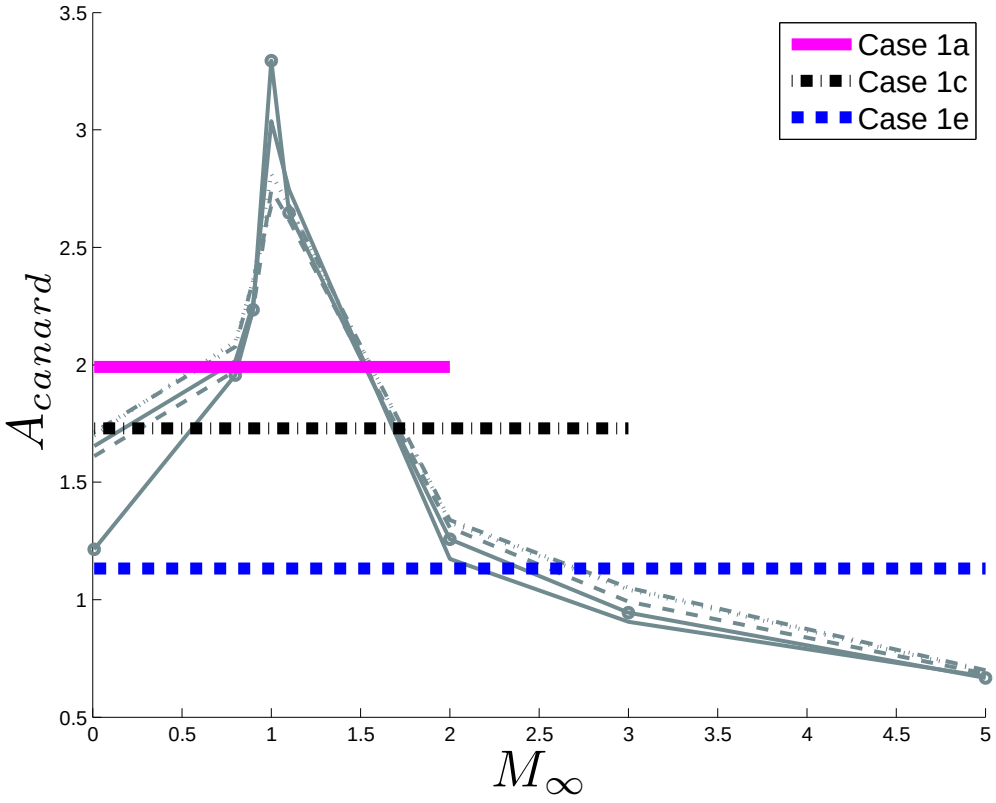

Figure 4.26: Case 1 constraint set 1 canard aspect ratio as a function of freestream Mach number as compared to Case 3

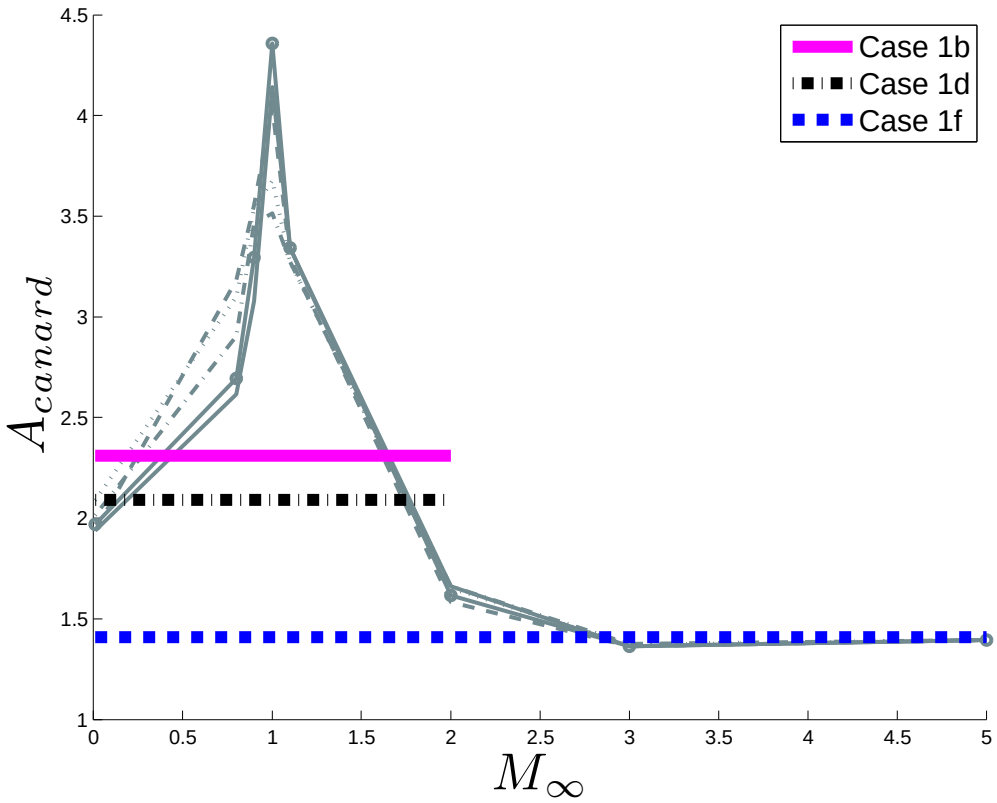

Figure 4.27: Case1 constraint set 2 canard aspect ratio as a function of freestream Mach number as compared to Case 3

This straightforward relationship with the curves produced by Case 3 can also be seen in Figure 4.27 and Figure 4.29 pertaining to the canard and wing aspect ratio of Case 1 constraint set 2 respectively. However, the wing aspect ratio relationship for Case 1 constraint set 1, shown in Figure 4.28, does not follow this pattern. An explanation of why these designs are optimum, would require further investigation. Potential explanations are given in the analysis of Case 3 in Section 4.3. A more complete understanding of the influence the wing geometry has on the design space for constraint set 1 would also help explain why the patternsearch method had difficulties in Case 2.

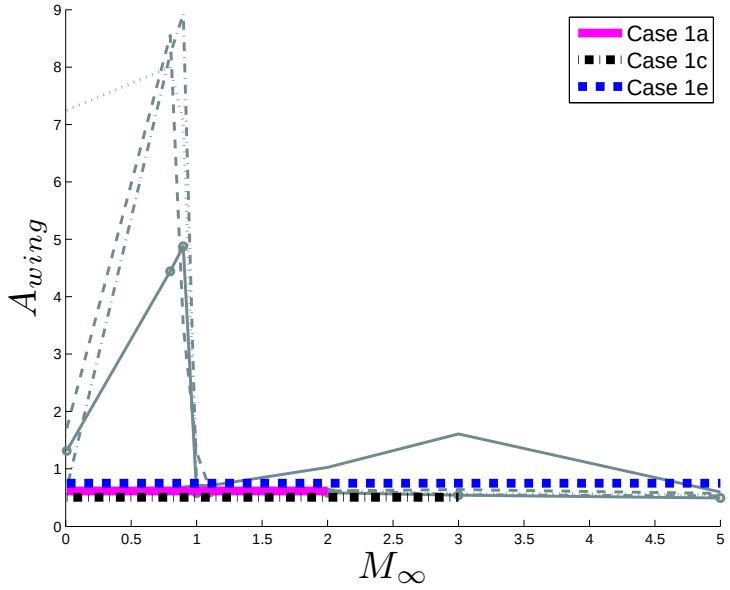

(a) Constraint set 1

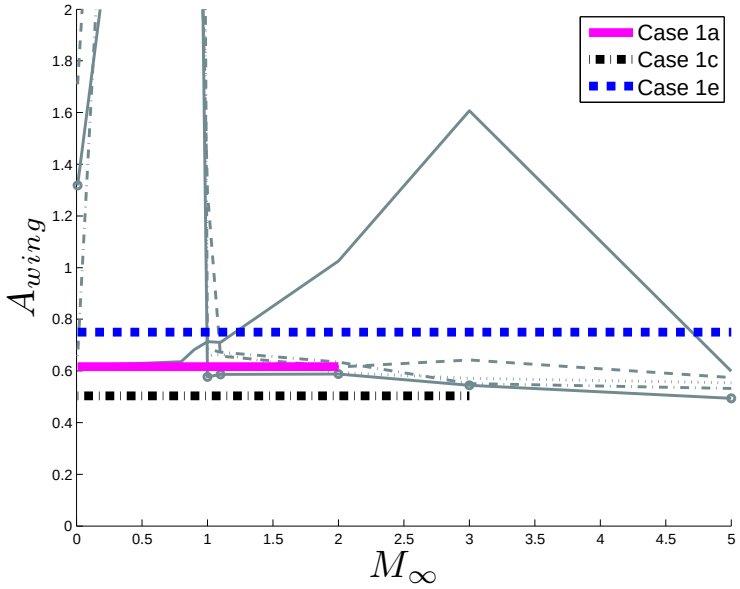

(b) Constraint set 1 zoom

Figure 4.28: Case 1 set 1 wing aspect ratio as a function of freestream Mach number as compared to Case 3

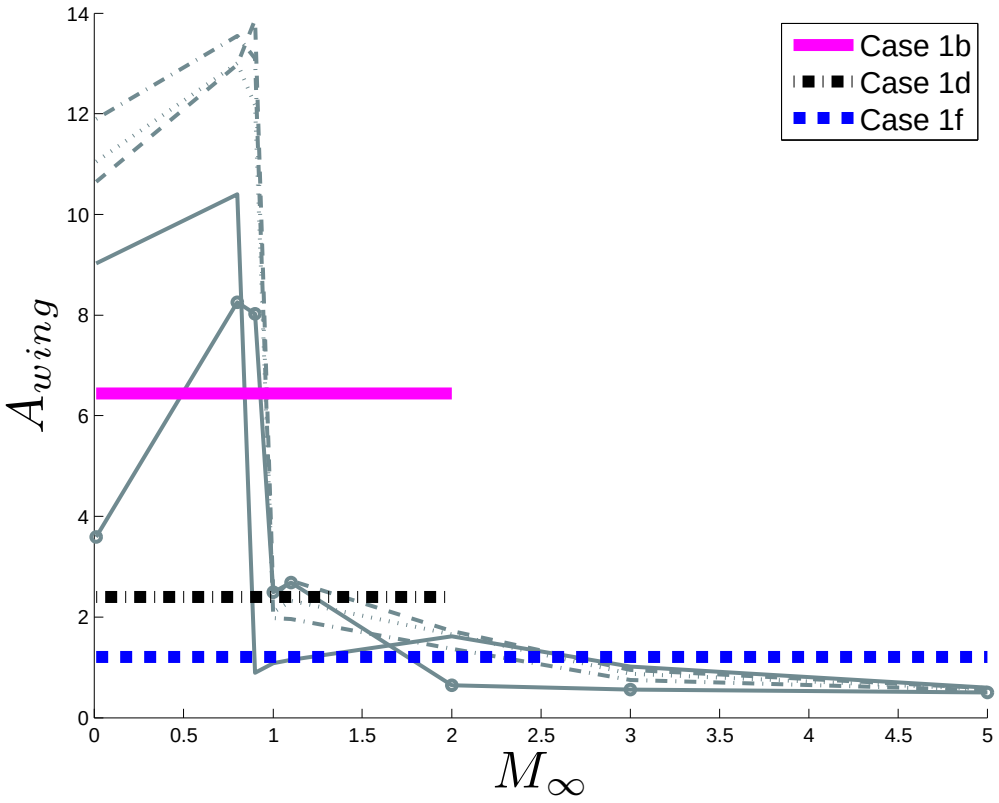

Figure 4.29: Case 1 set 2 wing aspect ratio as a function of freestream Mach number as compared to Case 3

Comparisons between the optimum designs of Case 2b and Case 2f with Case 3 are provided in Figure 4.30 and Figure 4.31. The analysis of these results parallel that of Case 1. The optimum aspect ratio of the wings or canards are values that minimize the differences from the Case 3 curves. The optimum way to accomplish this using two sets of wing and canard geometries was to designate each geometry to a particular Mach regime. For example, the canard aspect ratio of Configuration 1 for Case 2f was deployed for subsonic flight where $M_\infty \leq 1.1$. The figure shows that the optimum aspect ratio of 2.6 best fits the Case 3 values for $M_\infty \leq 1.1$. When the freestream Mach is greater than this range, the optimum Configuration 2 canard aspect ratio of Case 2f jumps down to 1.4. This value best fits the Case 3 values for $M_\infty > 1.1$. Now Case 2 uses two geometries in an attempt to minimize off-design lift to drag ratio penalties. The same explanation is valid for both the wing and canard aspect ratios for all configurations in Case 2b and Case 2f. In general, it was seen that the range and residence time of the freestream Mach numbers experienced during a particular trajectory is an important design driver for the optimum designs for Case 1 and Case 2.

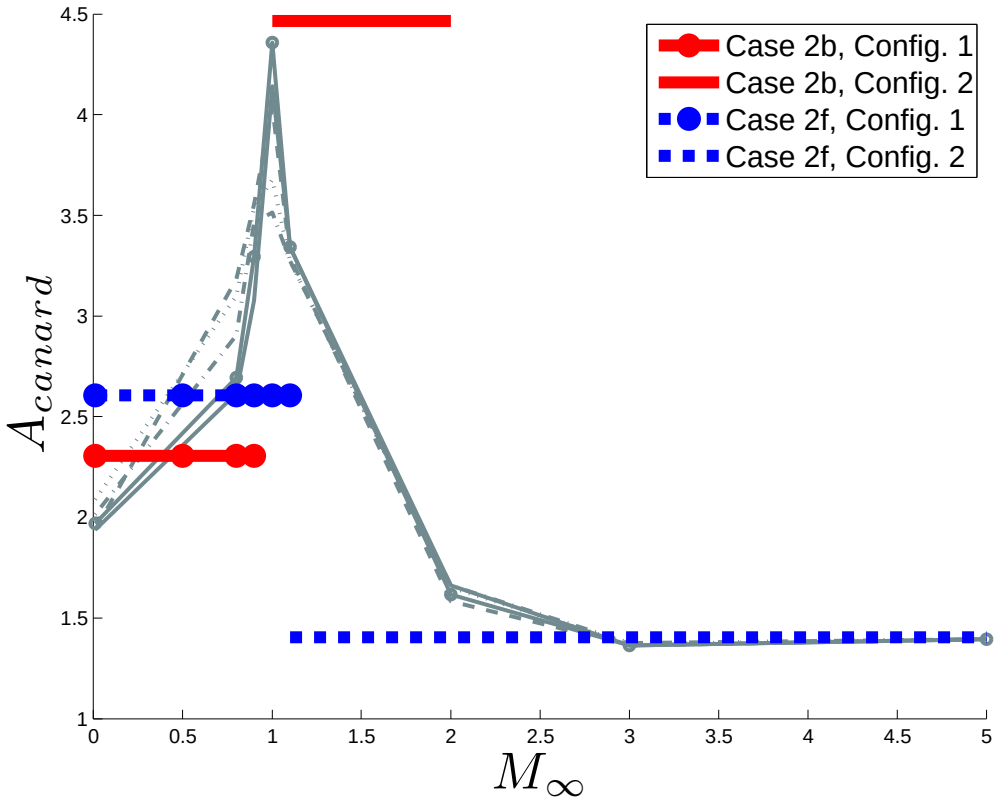

Figure 4.30: Case 2 canard aspect ratio as a function of freestream Mach number as compared to Case 3

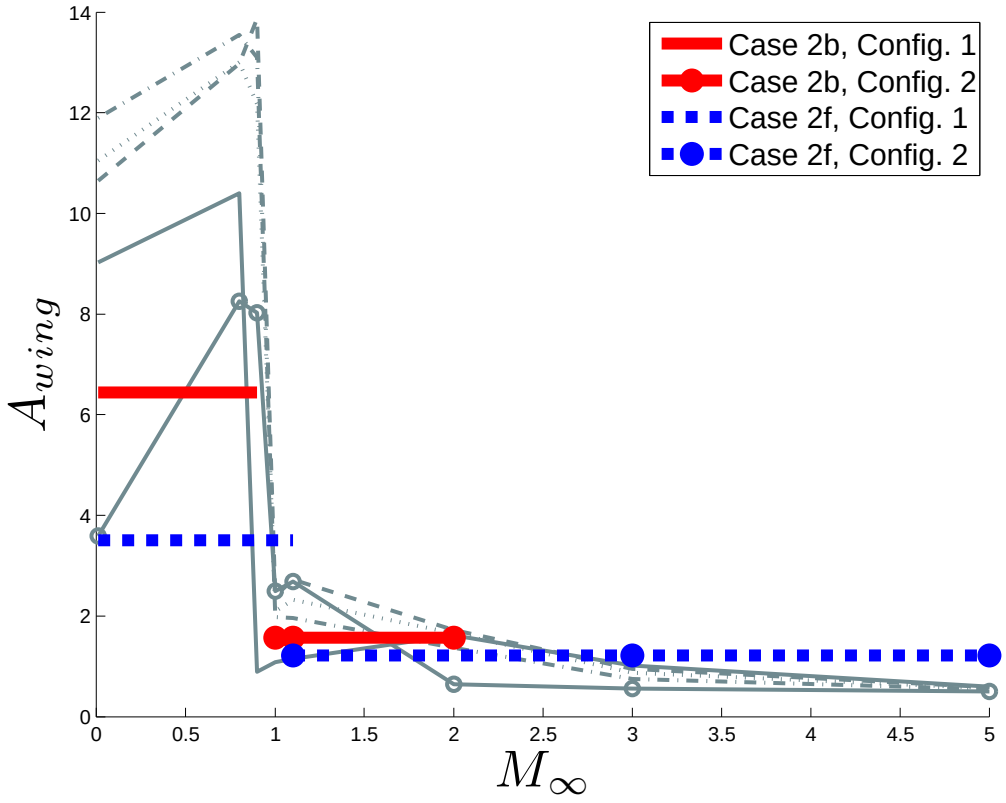

Figure 4.31: Case 2 wing aspect ratio as a function of freestream Mach number as compared to Case 3

4.5 Phugoid motion of the gliding trajectories

The canard control modeled in this thesis is all in the pitching plane of the projectile. This motion is termed longitudinal motion and is distinct from the lateral motion which governs rolling and yawing behavior. The longitudinal and lateral motions can be decoupled when considering projetiles of small, or in this case, zero degree roll angles [57]. The longitudinal motions posses two characteristic modes, a well-damped short period mode and a lightly damped long period mode. The motion of the short period mode is evident when the projectile exhibits pitching maneuvers. The long period or phugoid mode is a product of the velocity and attitude behavior of the trajectory. The current work made the assumption that the projectile instantaneously sets itself to the angles of attack dictated by the optimizer. No transient pitching motion is modeled, meaning the short period mode is not excited in these simulated trajectories. The oscillatory motion evident in the optimum trajectory plots is the phugoid motion of the projectile.

The phugoid mode of a gliding projectile is excited via a freestream velocity or angle of attack perturbation from the equilibrium conditions of an undisturbed or equilibrium flight path. For an equilibrium unpowered gliding flight path, the vertical component of the aerodynamic lift is a little less than the weight, where the gliding projectile sinks at a rate at which the potential energy loss balances the energy dissipated due to drag. For a given projectile design and flight altitude, there exists an optimum flight velocity and angle of attack such that the projectile is sustaining an equilibrium glide at a maximum possible lift to drag ratio. These

conditions produce the smallest possible glide angle and maximize the range of the gliding flight.

The trajectories studied in this thesis are more complex than the case of unpowered gliding flight at a given initial altitude and projectile design. The trajectories studied in this thesis find an optimum projectile design and launch angle for a given launch velocity such that the total range (sum of the pre-apogee and post-apogee range) is maximized. It was found that a maximum total range was produced at a launch angle which increases apogee altitude at the expense of apogee velocity. The apogee velocity is therefore smaller than the velocity needed for an undisturbed gliding flight for the given projectile design. A trade-off exists between the necessary conditions for equilibrium gliding flight and the altitude at apogee. Even though the post-apogee flight is not flying at the optimum equilibrium glide conditions, the combination of a phugoidal motion and the added altitude produces a longer range.

A simplified example of this is illustrated in Figure 4.32. In this hypothetical scenario, Trajectory A and B are both produced using the same projectile design for the same launch velocity. The varying parameter between the trajectories was simply the launch angle. Trajectory A was simulated using a launch angle of 41 degrees. At apogee, the projectile velocity is the value needed for the projectile to sustain an equilibrium glide at maximum global lift to drag ratio at a near constant angle of attack post-apogee. For Trajectory B, the launch angle was 55 degrees. Therefore, once apogee was reached, the velocity was below the necessary equilibrium condition. The altitude at the apogee of Trajectory B is higher than

that of Trajectory A. Trajectory B exhibits a phugoid motion oscillating around the equilibrium gliding flight path excited by the negative velocity perturbation at apogee. The decrease in post-apogee range brought forth by the non-optimum gliding phugoid motion of Trajectory B is counteracted by the vertical translation in the apogee position. Trajectory B therefore ends up producing a longer total range than that of Trajectory A.

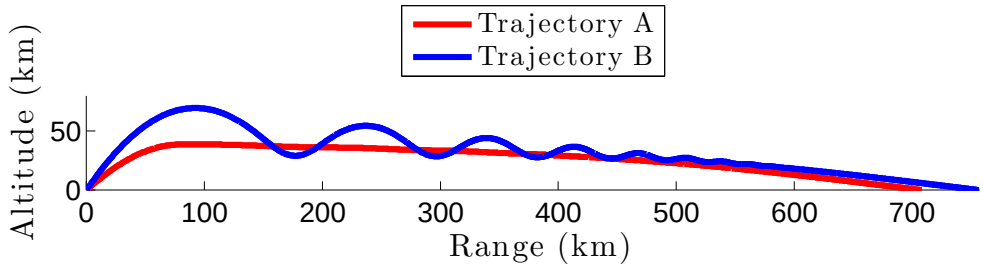

Figure 4.32: Example comparison of equilibrium and phugoid gliding flight paths

The illustrated example above helps explain the oscillatory characteristics exhibited in the optimum trajectories given in this chapter. It also helps explain why the maximum range of the entire trajectory does not necessarily exist when the post-apogee range is maximized (i.e. an equilibrium glide at global maximum lift to drag ratio). A more detailed discussion on the phugoid motion of gliding projectiles can be found in Ref. [58].

Chapter 5
Conclusions
5.1 Summary of Results

The primary objective of this research was to perform a detailed investigation into optimization trade-offs. This included an analysis of continuously varying geometry vs. discrete-point morphing concepts. To accomplish this, the present work included a combination of a detailed aerodynamic analysis, applicable to a wide flight envelope, coupled with studies of optimal trajectories. The aerodynamic modeling is applicable to subsonic, transonic, and supersonic conditions, for small-finned and winged geometries. The aerodynamic modeling is integrated within optimization techniques, where best projectiles shapes were found for any given trajectory, and then the best combination of trajectory and shape was identified.

This work provides many contributions to the field of both morphing projectiles and projectile design optimization. Lifting body projectile aerodynamic phenomena are identified and their importance to modeling gliding trajectories are discussed. These aerodynamic phenomena may not always be included in standard military projectile aero-prediction codes. The optimization design code in this thesis provided a working example which implemented direct search and gradient based optimization methods for searching a gliding projectile design space. Most importantly, this research acts as a tool for analyzing a given baseline projectile with a particular mission profile and identifying the best morphing strategy to maximize the range. It can determine the feasibility of extending the mission profile for

existing fin stabilized munitions through morphing.

For the gun muzzle energies used in the analysis, it was found that the trade-off between range and morphing complexity is clearly most beneficial for a single optimized geometry. Deployment of a single optimum set of wings and canards at apogee provided a substantial increase in range over a canard controlled glide of the baseline "low drag" configuration. The largest increase in range for the cases that enforce constraint set 1 was 36.8%, seen in Case 1a. For the runs that enforce side constraint set 2, the largest increase in range was 98.6% in Case 1b. The main advantage comes from using a low drag design for the pre-apogee mission leg and an optimum gliding geometry for the gliding phase. Two different geometries are tailored for the two phases of the trajectory.

When extending the idea to dual geometries or continuously changing geometries during the gliding phase, the added benefit in range was not substantial. For the dual geometry optimization, only runs 2b and 2f converged with a unique two configuration design. Deploying and swapping between the two optimized geometries only increased the range of Case 2b by an additional 3.23km over Case 1b. That is a mere 3.41% of the baseline range. For Case 2f, Deploying these two optimized geometries at their given freestream Mach regimes over the entire trajectory, increased the range of the projectile by 4.14km over Case 1f (1.74% of baseline range). When extending the scenario to continuous morphing, the largest percent increase in range over the baseline case was 12.1%, seen in Case 3b. The morphing wings and canards essentially tailor the projectile geometry to changes in flight Mach number. A lack of added range for these morphing strategies are a direct

correlation to a lack of extreme freestream Mach number changes throughout the gliding phase of the trajectory.

It is important to keep in mind that the more complex morphing schemes analyzed in this thesis would be technologically difficult to implement and added aerodynamic penalties paid by such mechanisms are not modeled. If transient aerodynamic effects of wing and canard morphing and other projectile imperfections were taken into account it is possible that the minor benefits found for the more complex morphing schemes would no longer exist. The most ideal morphing scheme of continuously changing geometries was modeled while using optimistic assumptions on how the integration of the morphing mechanics would effect aerodynamic performance. Even so, for standard gun muzzle velocities, the range only extends several kilometers past the range of a single optimized wing and canard geometry. For standard 155mm projectiles the most feasible way of extending the range by utilizing morphing gliding projectiles would be to deploy a single optimized set of wings and canards for post-apogee gliding flight.

An analysis of the optimum geometries for Case 1, 2, and 3 brought forth several interesting and important conclusions. The first characteristic to recognize was the importance of the upper limit of the canards span. It was concluded that for the scale of projectiles studied in this thesis, the canard span was the limiting design variable in the optimization. Maximizing the upper limit of the canard span, while minimizing canard wake interference effects, should be a main focus of morphing projectile preliminary design. The extent and residence time of the freestream Mach numbers experienced during a particular trajectory are also important design drivers

for the optimum designs of Case 1 and Case 2. Single and dual optimum wing/canard geometries minimize the loss of lift to drag ratio due to off-design Mach conditions. This can qualitatively be seen by comparing the aspect ratios of the single and dual wing/canard geometries to that continuously varying aspect ratio wings.

For the design space being explored in Case 2, when starting from the given initial designs, it was found that the "areas" of better solutions within the design hyperspace were too small for the pattern search algorithm to find them in all six runs. This may be a product of the fact that the projectile does not experience enough of a range of Mach number altitude variations and hence the increment in range for a swapping geometry is minimal. If, for instance, the projectile being optimized happened to be a powered cruise missile, the range of freestream Mach numbers experienced during the flight would be more extreme for longer periods of time. This would open up the design space making it easier for the pattern search technique to find two different geometries to swap between and therefore increasing the range.

Alternatively, a way to remedy this problem would be to customize the procedure for updating the mesh size or even use a different zero-th order method all together (Genetic Algorithms or Simulated Annealing). Another possible explanation for these results would be an existence of multiple local maxima within the design space. To check this, a denser multistart optimization should be conducted. Analyzing all these results would more likely capture any local maxima, and hopefully pinpoint the global maximum. A further investigation into this design space is necessary to reveal the true nature of the optimum geometry found in this study.

Even though the pattern search method does not guarantee global optimum solutions, it is important to note that the global optimum solution may not be the "best" solution. Local optima may just as well satisfy the mission requirements or even be more beneficial than the global optimum. This happens because optimizers, by default, put no weight on off-design conditions. For example, the global optimum for the type of problem studied in this work is likely to be extremely sensitive to angle of attack perturbations. Meaning, a slight wind gust in the pitch plane could cause the projectile to go unsteady, causing catastrophic failure. Whereas a local optimum design, even though it results in a slightly shorter range, may be more robust to such off-design conditions while still fitting the mission requirements. Therefore, it is important to never write off any of the local optimums. If possible, the entire design space should be analyzed and a sensitivity analysis should be completed at some time during the preliminary design phase.

5.2 Future Work

Future additions to this work fall into two categories: 1) improved aerodynamic modeling, and 2) improved optimization schemes. For computational efficiency, aerodynamics in the optimizer is modeled with relatively simple, yet robust, analytical formulations. This captures most of the relevant aerodynamics, but should be confirmed with a more detailed computational solution. It would be computationally prohibitive to include a detailed model in the optimization subroutines; however, once a geometry is chosen by the optimizer using the analytical tools described in this thesis, a more detailed computational study can be performed on one,

or perhaps several, candidate shapes at various points in the trajectory. Further, the analytical modeling has not included the effects of pivoting devices or losses associated with the actual mechanics of morphing geometries, because of the limits of the analytical description. Subsequent efforts could investigate wing deployment or morphing mechanisms, similar to work done by Cui [59], and explore the drag penalties and overall performance degradation associated with realistic mechanisms.

Future work in exploring the morphing projectile design space is needed to better understand its characteristics. Differentiation between a global maximum or minimum and local maxima or minima is necessary to make valid comparisons between optimum projectile geometries of varying morphing capabilities. In order to accomplish this, the capabilities of other optimization algorithms to solve the problem statement in this thesis needs to be explored. The use of genetic algorithms or simulated annealing would require a significant amount of objective function evaluations. This would require that the runtime of the current optimization problem statement be reduced through a faster CPU or more efficient software.

Once the current design space is fully understood, increased complexity and realism can be accomplished through multi-objective optimization. Several different metrics, such as lateral acceleration, static margin, pitch damping, etc., could be included offer a more complete picture of the required projectile performance for a given mission. Global trajectory properties such as minimizing time of flight or maximizing impact velocity, for example, may also play a significant role in the mission requirements. All of these factors may be included as separate objective functions in a multi-objective optimization scheme yielding different optimal solutions.

Appendix A
Optimization Iteration Histories

NOTE: Design variables are normalized using the following equation:

$$X_{norm} = \frac{\left(X - X^L\right)}{\left(1.00001\right)\left(X^U\right) - \left(X^L + 0.00001\right)} \tag{A.1}$$

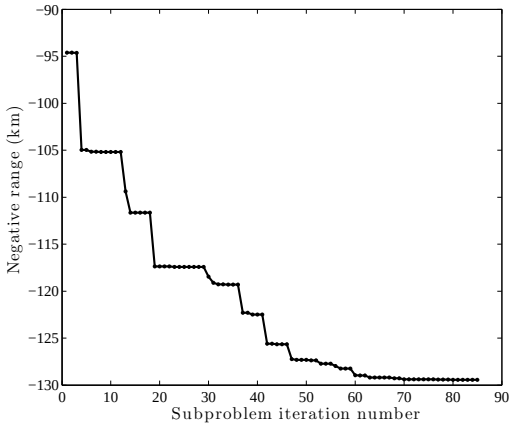

(a) Case 1a objective function iteration history

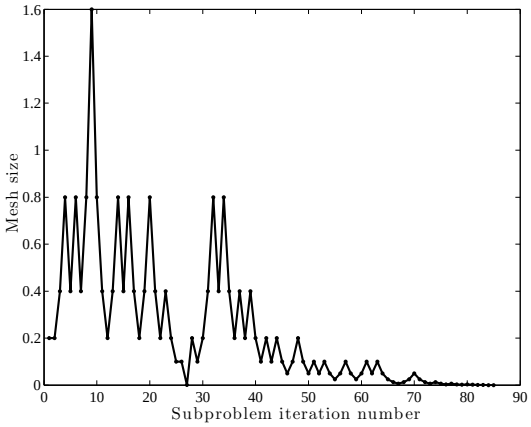

(b) Case 1a mesh iteration history

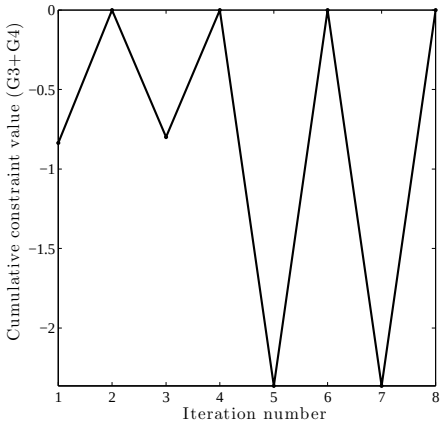

(c) Case 1a constraint iteration history

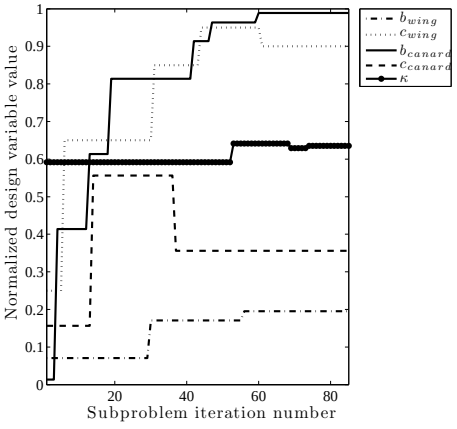

(d) Case 1a design variable iteration history

Figure A.1: Case 1a iteration histories

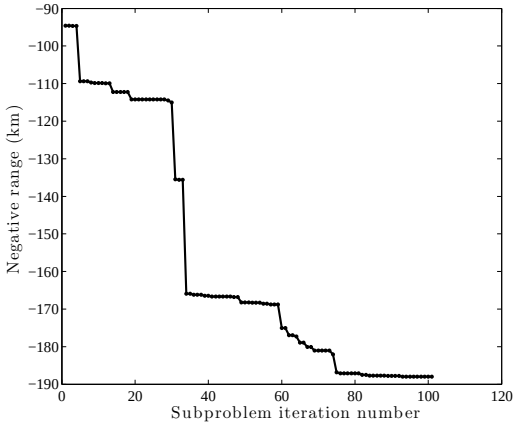

(a) Case 1b objective function iteration history

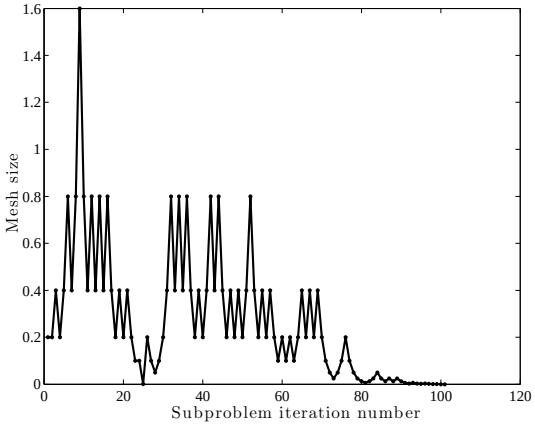

(b) Case 1b mesh iteration history

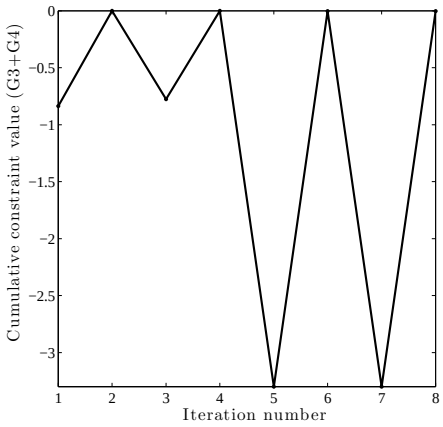

(c) Case 1b constraint iteration history

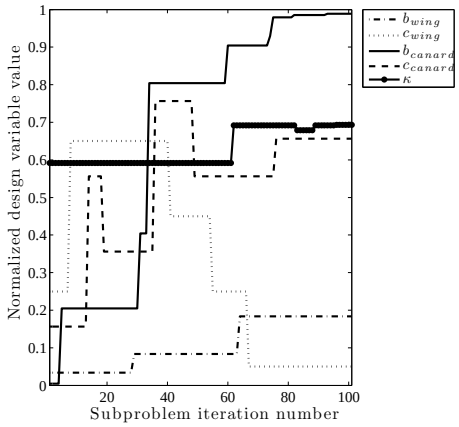

(d) Case 1b design variable iteration history

Figure A.2: Case 1b iteration histories

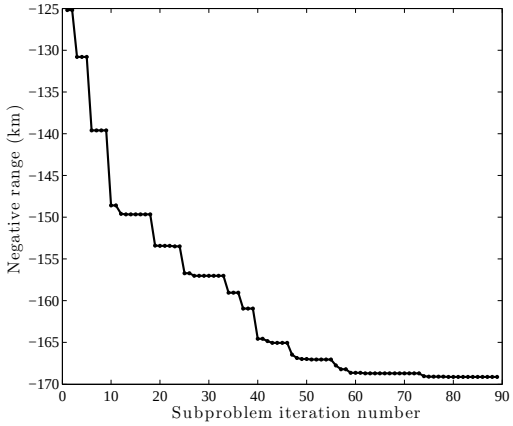

(a) Case 1c objective function iteration history

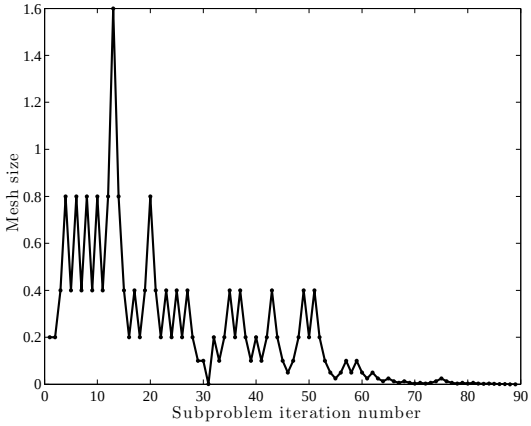

(b) Case 1c mesh iteration history

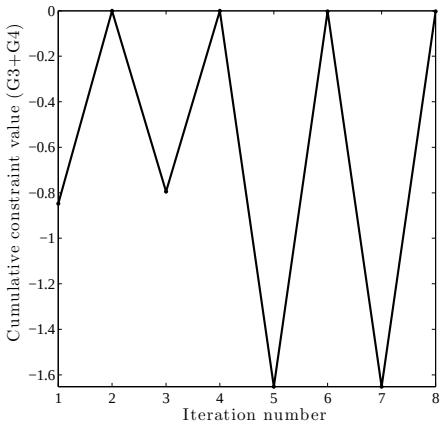

(c) Case 1c constraint iteration history

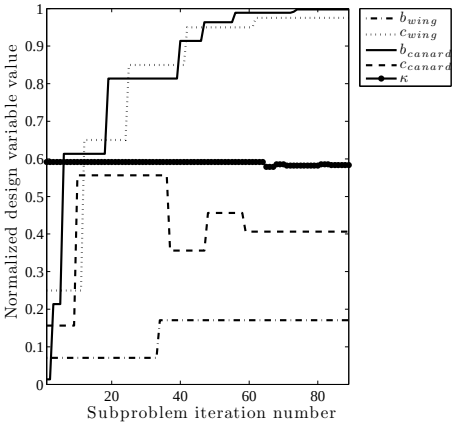

(d) Case 1c design variable iteration history

Figure A.3: Case 1c iteration histories

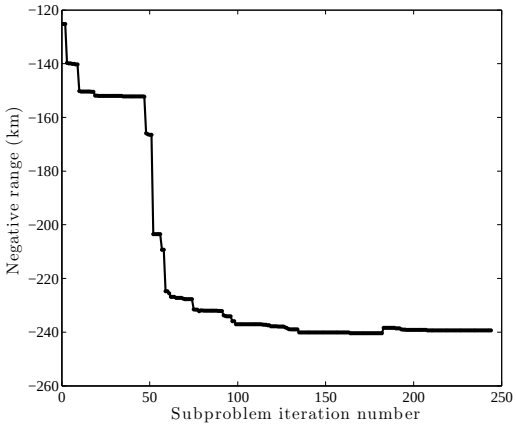

(a) Case 1d objective function iteration history

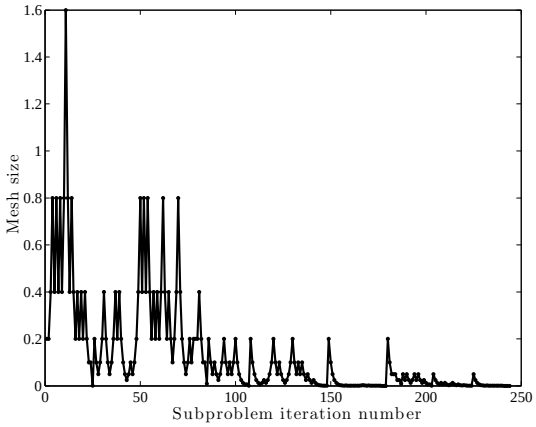

(b) Case 1d mesh iteration history

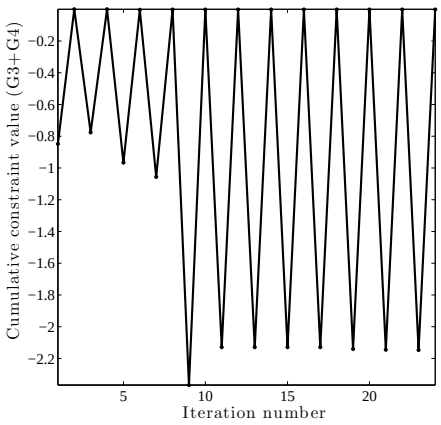

(c) Case 1d constraint iteration history

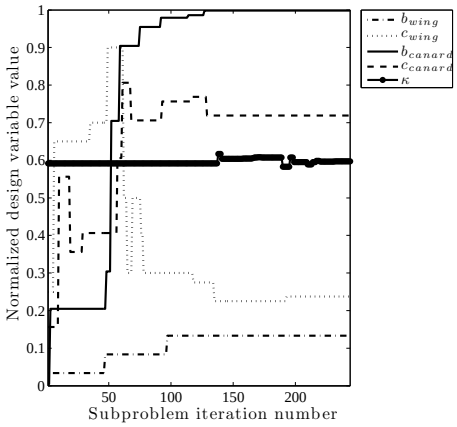

(d) Case 1d design variable iteration history

Figure A.4: Case 1d iteration histories

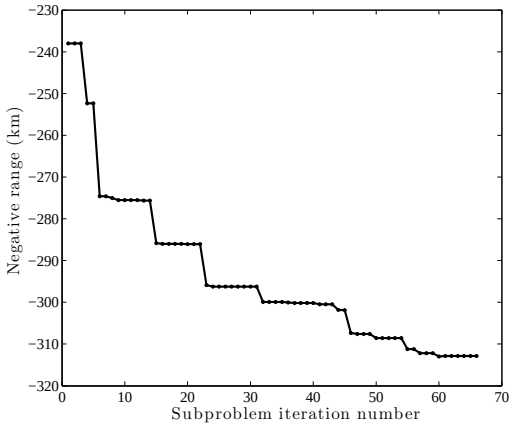

(a) Case 1e objective function iteration history

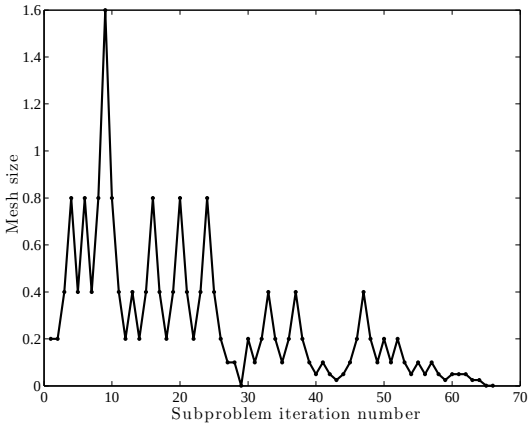

(b) Case 1e mesh iteration history

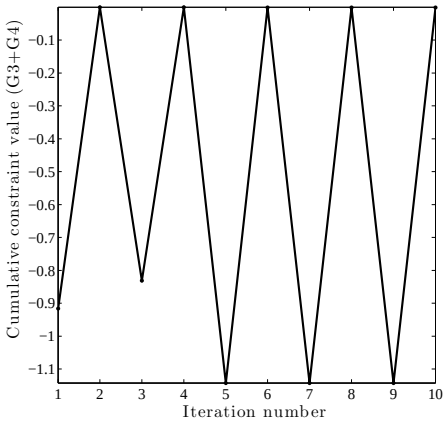

(c) Case 1e constraint iteration history

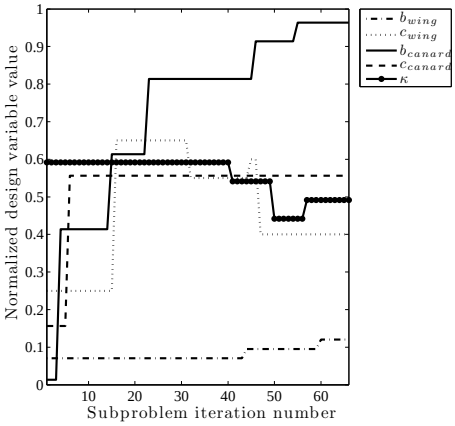

(d) Case 1e design variable iteration history

Figure A.5: Case 1e iteration histories

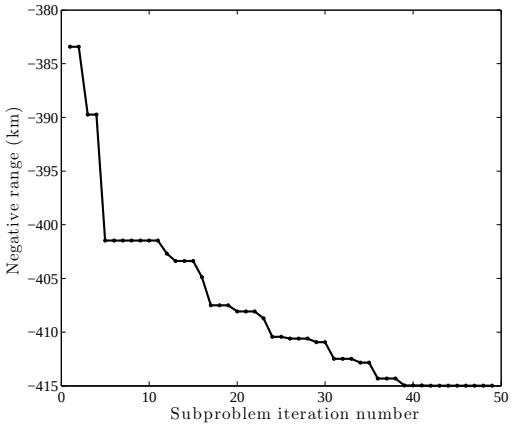

(a) Case 1f objective function iteration history

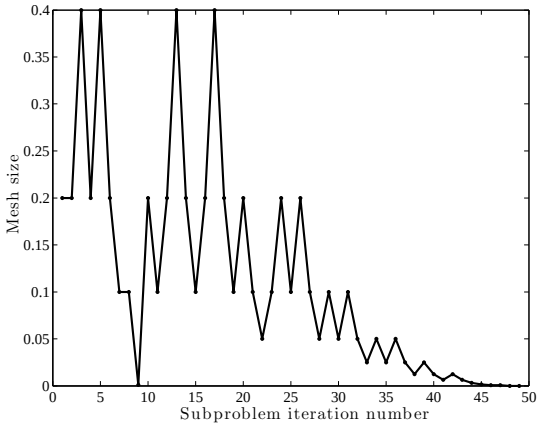

(b) Case 1f mesh iteration history

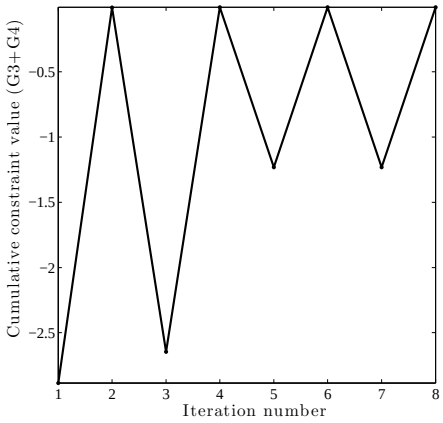

(c) Case 1f constraint iteration history

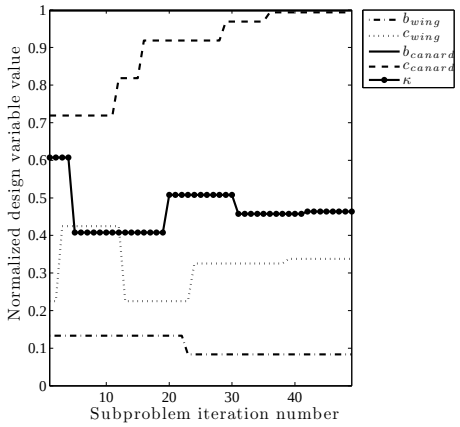

(d) Case 1f design variable iteration history

Figure A.6: Case 1f iteration histories

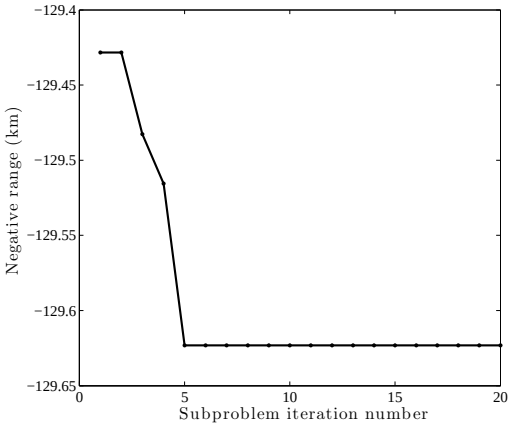

(a) Case 2a objective function iteration history

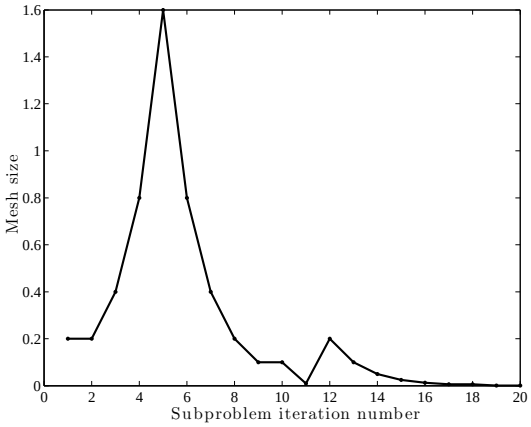

(b) Case 2a mesh iteration history

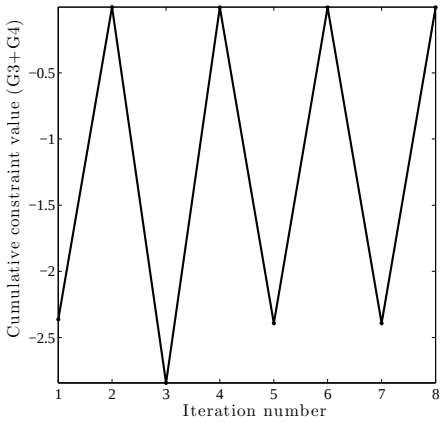

(c) Case 2a constraint iteration history

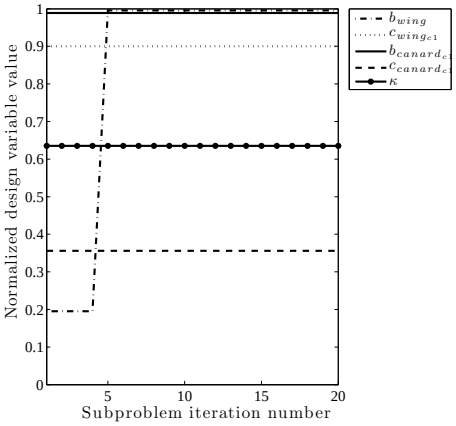

(d) Case 2a design variable iteration history

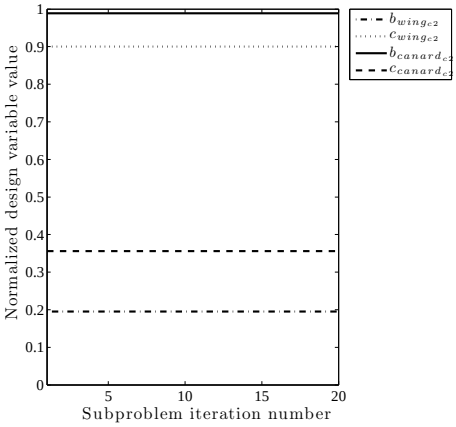

(e) Case 2a design variable iteration history

Figure A.7: Case 2a iteration histories

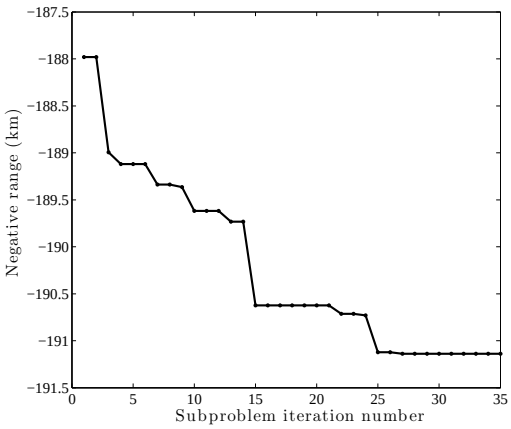

(a) Case 2b objective function iteration history

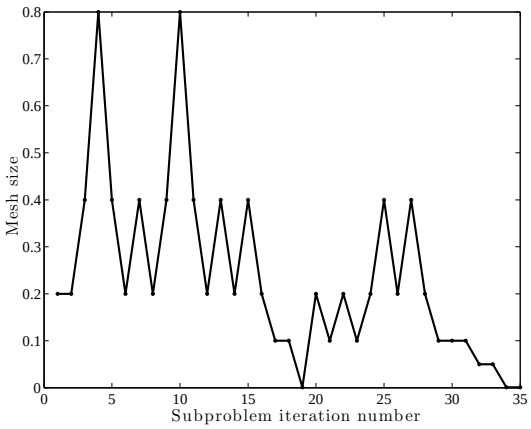

(b) Case 2b mesh iteration history

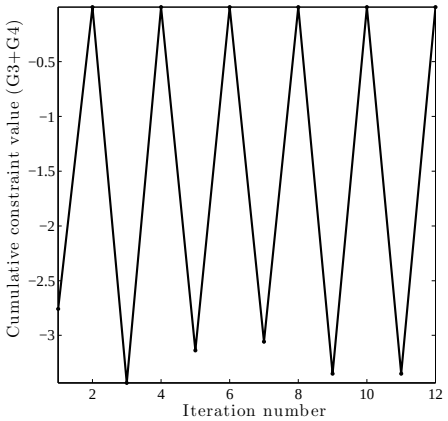

(c) Case 2b constraint iteration history

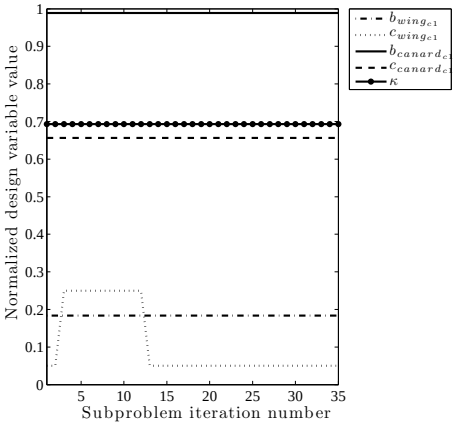

(d) Case 2b design variable iteration history

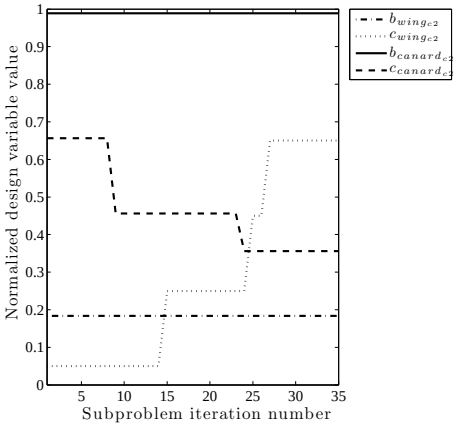

(e) Case 2b design variable iteration history

Figure A.8: Case 2b iteration histories

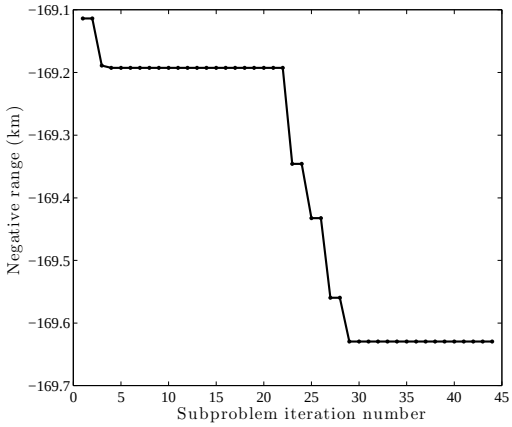

(a) Case 2c objective function iteration history

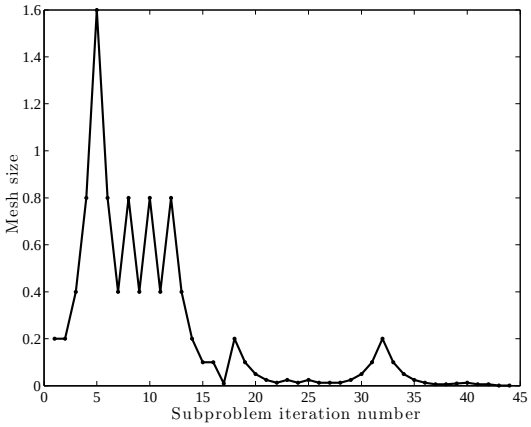

(b) Case 2c mesh iteration history

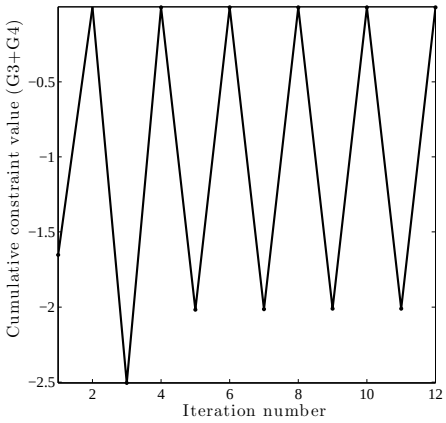

(c) Case 2c constraint iteration history

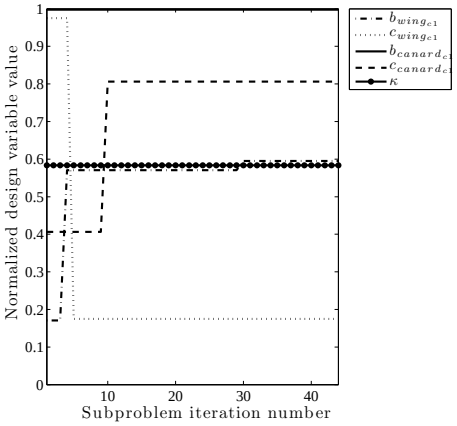

(d) Case 2c design variable iteration history

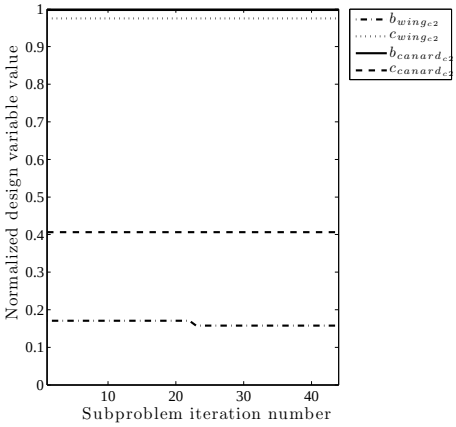

(e) Case 2c design variable iteration history

Figure A.9: Case 2c iteration histories

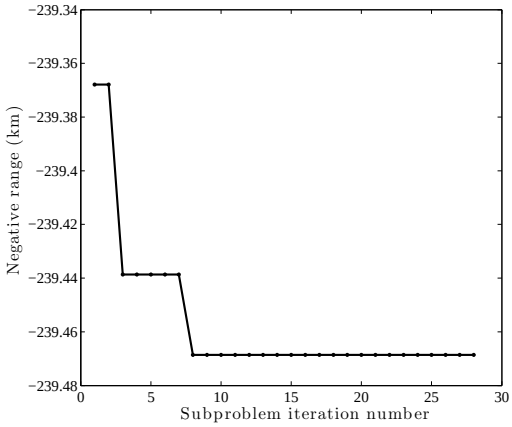

(a) Case 2d objective function iteration history

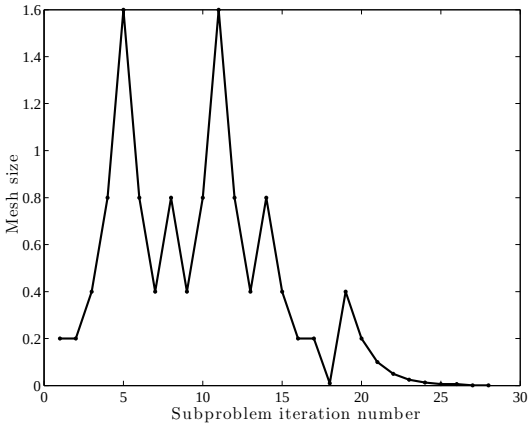

(b) Case 2d mesh iteration history

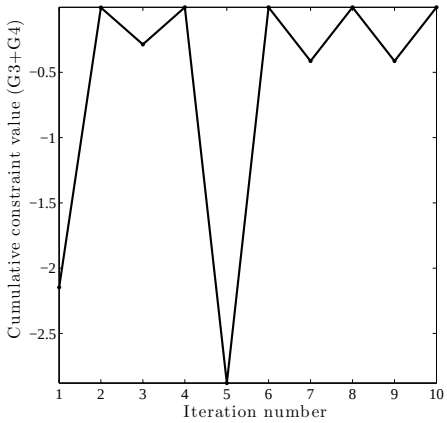

(c) Case 2d constraint iteration history

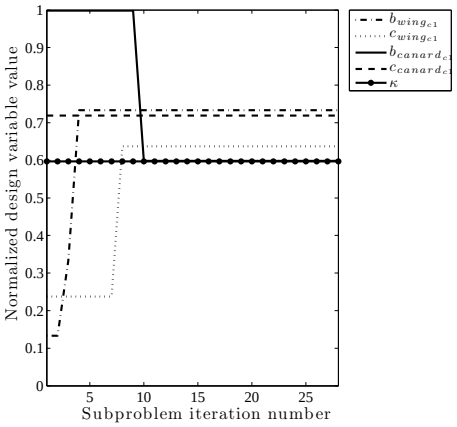

(d) Case 2d design variable iteration history

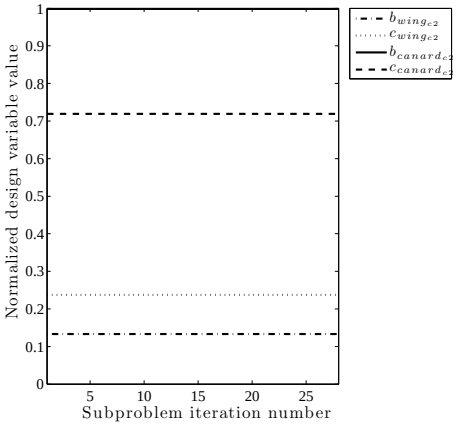

(e) Case 2d design variable iteration history

Figure A.10: Case 2d iteration histories

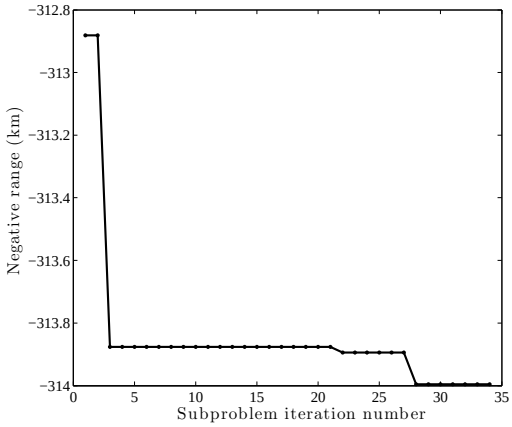

(a) Case 2e objective function iteration history

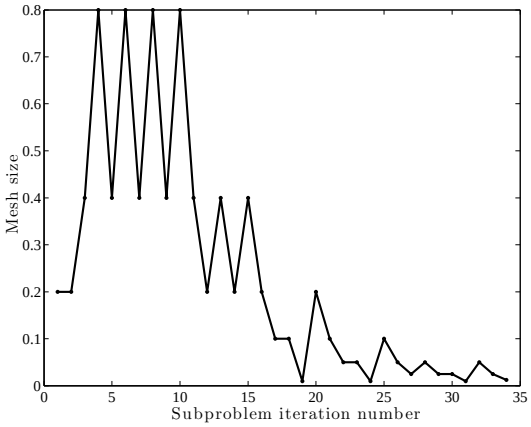

(b) Case 2e mesh iteration history

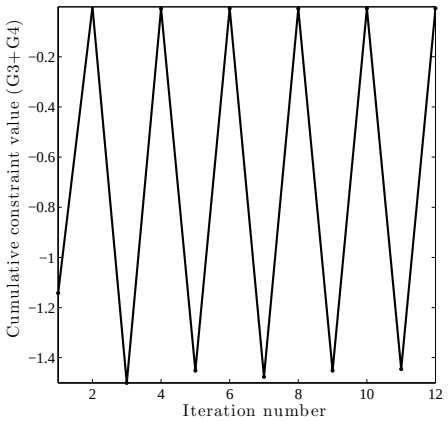

(c) Case 2e constraint iteration history

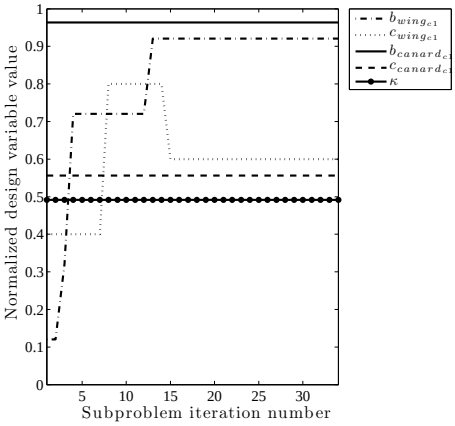

(d) Case 2e design variable iteration history

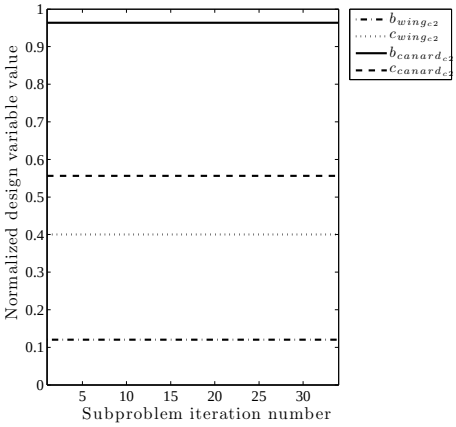

(e) Case 2e design variable iteration history

Figure A.11: Case 2e iteration histories

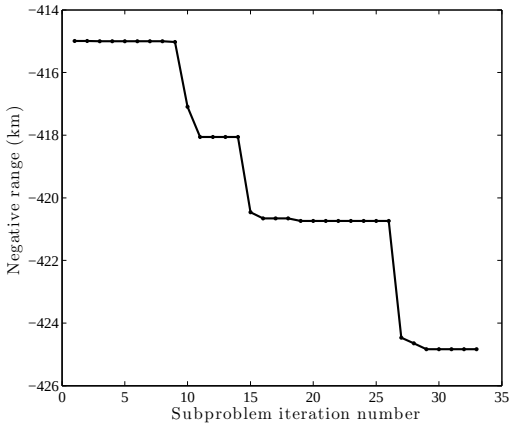

(a) Case 2f objective function iteration history

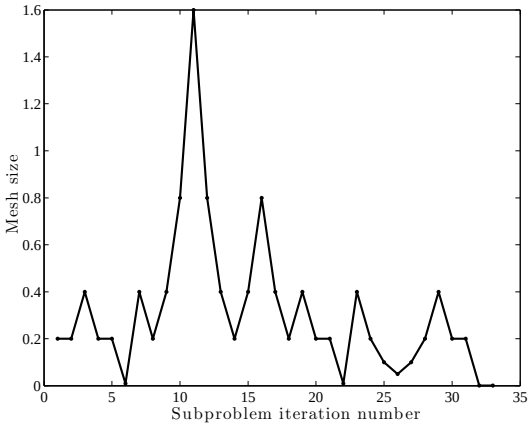

(b) Case 2f mesh iteration history

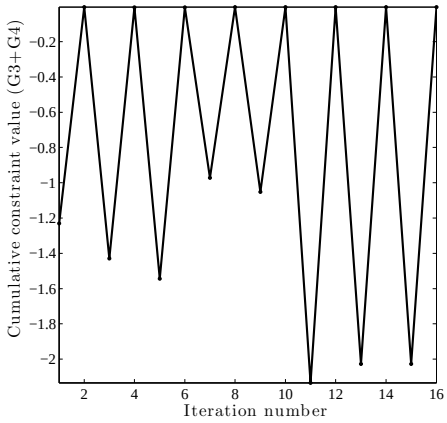

(c) Case 2f constraint iteration history

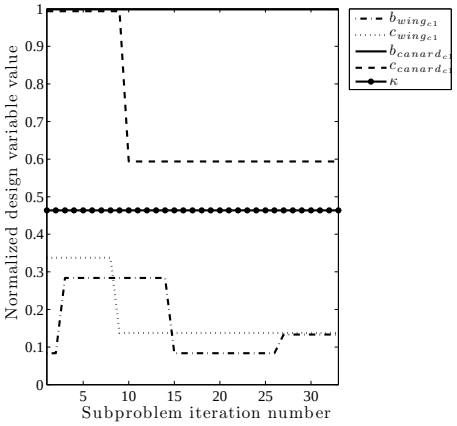

(d) Case 2f design variable iteration history

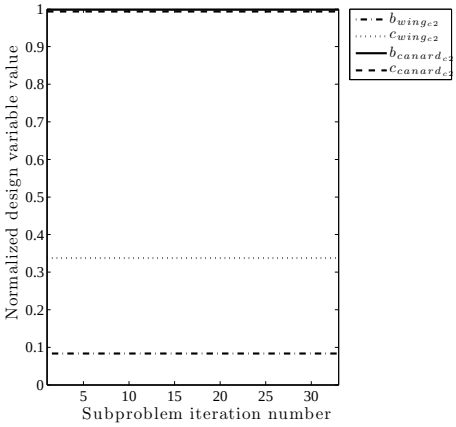

(e) Case 2f design variable iteration history

Figure A.12: Case 2f iteration histories

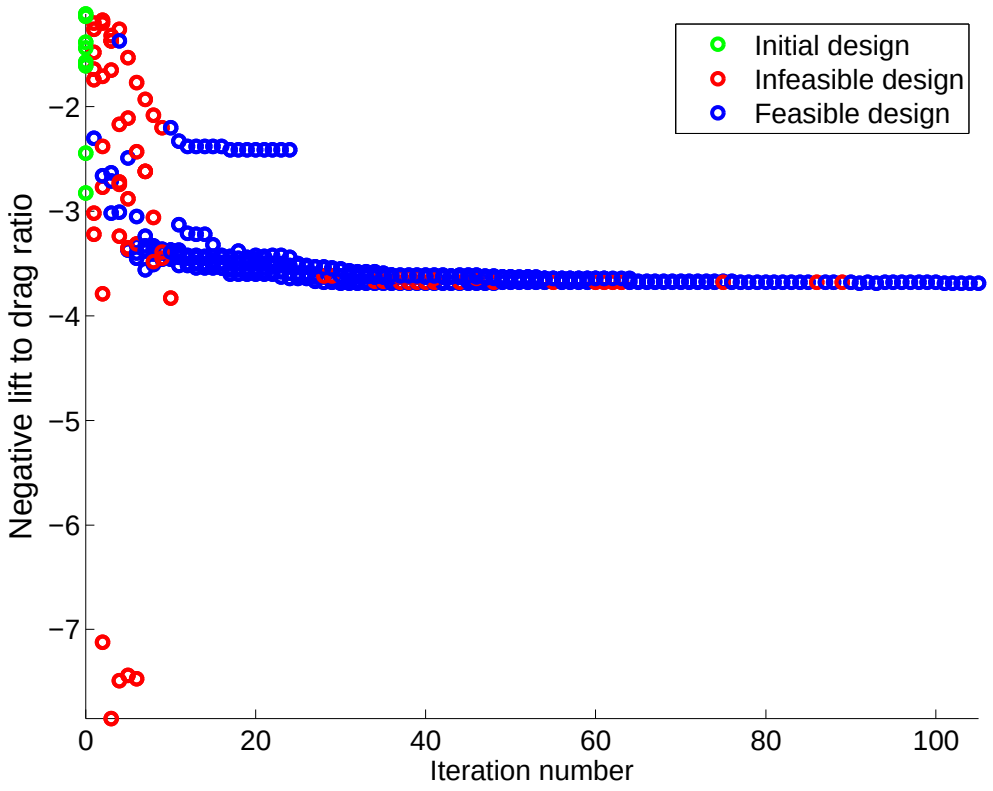

Figure A.13: Case 3 example objective function iteration history for constraint set 1 with $h = 0$ and $M_\infty = 0.01$

Bibliography

[1] A.R. Rodriguez. Morphing aircraft technology. *48th AIAA Aerospace Sciences Meeting and Exhibit*, January 2007.

[2] W.A. Crossley, M.D. Skillen, J.B. Frommer, and B.D. Roth. Morphing aircraft sizing using design optimization. *Journal of Aircraft*, 48(2):612–622, March-April 2011.

[3] E.A. Leylek and M.F. Costello. Benefits of autonomous morphing aircraft in loiter and attack missions. *AIAA Atmospheric Flight Mechanics Conference*, August 2010.

[4] J. Mestrinho, P. Gamboa, and P. Santos. Design optimization of a variable-span morphing wing for a small uav. *AIAA Atmospheric Flight Mechanics Conference*, August 2010.

[5] S.P. Joshi, Z. Tidwell, W.A. Crossley, and S. Ramakrishnan. Comparison of morphing wing strategies based upon aircraft performance impacts. *45th AIAA Structures, Structural Dynamics, and Materials Conference*, April 2004.

[6] T.T. Takahashi, R.J. Spall, D.C. Turner, J.C. Otto, and P. O'Hagan. A multi-disciplinary assesment of morphing aircraft technology applied to tactical cruise missile configurations. *45th AIAA Structures, Structural Dynamics, and Materials Conference*, April 2004.

[7] D. Lesieutre, M. Dillenius, and T. Lesieutre. Multidisciplinary design optimization of missile configuraitons and fin planforms for improved performance. *7th Symposium on Multidisciplinary Analysis and Optimization*, September 1998.

[8] O. Tekinalp and M. Bingol. Simulated annealing for missile optimization: Developing method and formulation techniques. *Journal of Spacecraft and Rockets*, 27(4):616–626, July-August 2004.

[9] D. Lisk, T. Robinson, and D. Robinson. Multi-objective optimization of supersonic projectiles using evolutionary algorithms. *48th AIAA Aerospace Sciences Meeting Including the New Horizons Forum and Aerospace Exopsition*, January 2010.

[10] C. Tanil, B. E. Platin, and G. Mahmutyazicioglu. External configuration optimization of missiles in conceptual design. *AIAA Atmospheric Flight Mechanics Conference*, August 2009.

[11] M.B. Anderson, J.E. Burkhalter, and R.M. Jenkins. Missile aerodynamic shape optimization using genetic algorithms. *Journal of Spacecraft and Rockets*, 37(5), September-October 2000.

[12] Y. Yang, S. Jung, T. Cho, and R. Myong. An aerodynamic shape optimization study to maximize the range of a guided missile. *28th AIAA Applied Aerodynamics Conference*, June-July 2010.

[13] Army Materiel Command. Design of aerodynamically stabilized free rockets. Technical Report MIL-HDBK-762, US Army Missile Command, July 1990.

[14] H. Gwin and D. Spring. Stability characteristics of a family of tangent ogive - cylinder bodies at mach numbers from 0.2 to 1.5. Technical Report RG-TR-61-1, ABMA, June 1961.

[15] L.H. Johnson. High supersonic and hypersonic aerodynamic derivatives. Technical Report 00.182, Temco, June 1960.

[16] C. De Jong. The effect of low aspect ratio rectangular and delta cruciform fins on the stability of bodies of revolution with tangent ogives at small angles of attack through a mach number range of 0 to 3.5. Technical Report RF-TR-62-1, U.S. Army Ordnance Missile Command, July 1962.

[17] F.M. White. *Viscous Fluid Flow*. McGraw-Hill, second edition, 1991.

[18] R.A. Minzner, K.S. Champion, and H.L. Pond. The ardc model atmosphere. Technical Report TR-59-267, Air Force Cambridge Research Center, 1959.

[19] W.E. Stoney Jr. Collection of zero-lift drag data on bodies of revolution from free-flight investigations. Technical Report NASA TR-R-100, NASA, 1952.

[20] M.D. Van Dyke. Practical calculation of second-order supersonic flow past non-lifting bodies of revolution. Technical Report NASA TN-2744, NASA, July 1952.

[21] G.E. Soloman. *Transonic Flow Past Cone-Cylinders*. PhD thesis, California Institute of Technology, Pasadena, California, 1953.

[22] S.F. Hoerner. *Fluid-Dynamic Drag*. Published by the Author, first edition, 1958.

[23] Bureau of Naval Weapons. Handbook of supersonic aerodynamics. Technical Report 1488, Department of the Navy, October 1961. Section 8: Bodies of Revolution.

[24] D.R. Chapman. An analysis of base pressure at supersonic velocities and comparison with experiments. Technical Report TR-1051, NACA, 1951.

[25] C.E. Brazzel. A kinetic energy concept for establishing power-off base pressure. Technical Report RD-TN-68-8, US Army Missile Command, 1968.

[26] E.S. Love. Base pressure at supersonic speeds on two-dimensional airfoils and bodies of revolution with and without fins having turbulent boundary layers. Technical Report TN-3819, NACA, 1957.

[27] A. Seiff and et al. Aerodynamic characteristics of bodies at supersonic speeds. Technical Report RN-A51J25, NACA, 1951.

[28] D.V. Rubin, C.E. Brazzel, and J.H. Henderson. The effects of jet plume and boattail geometry on base and afterbody pressures of a body of revolution at mach numbers of 2.0 and 3.5. Technical Report RD-TR-70-5, US Army Missile Command, 1970.

[29] A.S. Mahdi and M. Al-Atabi. Effect of body shape on the aerodynamics of projectiles at superosnic speeds. *Journal of Engineering Science and Technology*, 3(3):278–292, 2008.

[30] K. Gersten. Calculation of non-linear aerodynamic stability derivatives of aeroplanes. Technical Report Rept. 342, AGARD, April 1961.

[31] C.E. Brown and W.H. Michael. On slender delta wings with leading-edge separation. Technical Report TN-3430, NACA, 1955.

[32] K.W. Mangler and J.H.B Smith. A theory of the flow past a slender delta wing with leading edge separation. *Proceedings of the Royal Society*.

[33] E.C. Polhamus. Predictions of vortex-lift characteristics by a leading-edge suction analogy. *Journal of Aircraft*, 8(4):193–199, 1971.

[34] E.C. Polhamus. Application of the leading edge suction analogy of vortex lift to the drag due to lift of sharp edge delta wings. Technical Report TN-D-4739, NASA, August 1968.

[35] E.C. Polhamus. Charts for predicting the subsonic vortex lift characteristics of arrow, delta, and diamond wings. Technical Report TN-D-6243, NASA, April 1971.

[36] E.C. Polhamus. A concept of the vortex lift of sharp-edge delta wings based on a leading edge suction analogy. Technical Report TN-D-3767, NASA, December 1966.

[37] H. Multhopp. Methods for calculating the lift distribution of wings (subsonic lifting-surface theory). Technical Report No. 2884, British A.R.C, January 1950.

[38] H.J. Stewart. The lift of a delta wing at supersonic speeds. *Quarterly of Applied Mathematics*.

[39] A.H. Shapiro. *The Dynamics and Thermodynamics of Compressible Fluid Flow*, volume 1. Ronald Press Co., 1953.

[40] C.E. Brown. Theoretical lift and drag of thin triangular wings at supersonic speeds. Technical Report Rept. 839, NACA, November 1946.

[41] H.W. Leipmann and A. Roshko. *Elements of Gas Dynamics*. Dover Publications, 2002.

[42] A.V. Gafarian and W.L. Phillips. The supersonic lift and centers of pressure of rectangular and clipped-delta fins in combination with ling cylindrical bodies-comparison between theory and experiment. Technical Report NOTS TM-966, US Naval Ordnance Test Station, 1953.

[43] K. Margolis. Supersonic wave drag of sweptback tapered wings at zero lift. Technical Report NACA TR-1448, NACA, 1947.

[44] K. Margolis. Supersonic wave drag of nonlifting sweptback tapered wings with mach lines behind the line of maximum thickness. Technical Report NACA TR-1672, NACA, 1948.

[45] G. Morikawa. Supersonic wing-body lift. *Journal of the Aeronautical Sciences*.

[46] W. C. Pitts, J. N. Nielsen, and G. E. Kaattari. Lift and center of pressure of wing-body-tail combinations at subsonic, transonic, and supersonic speeds. Technical Report NACA TR-1307, NACA, 1957.

[47] E.L. Tu. Navier-stokes simulation of a close-coupled canard-wing-body configuration. *AIAA Aerospace Sciences Meeting*, January 1991.

[48] *Program to Optimize Simulated Trajectories (POST)*.

[49] R.H. Byrd, J.C. Gilbert, and J. Nocedal. A trust region method based on interior point techniques for nonlinear programming. *Mathematical Programming*.

[50] R.H. Byrd, M.E. Hribar, and J. Nocedal. A trust region method based on interior point techniques for nonlinear programming. *SIAM Journal on Optimization*.

[51] R.A. Waltz, J.L. Morales, J. Nocedal, and D. Orban. An interior algorithm for nonlinear optimization that combines line search and trust region steps. *Mathematical Programming*.

[52] R. Fletcher and M.J.D. Powell. A rapidly convergent descent method for minimization. *Computer Journal*, 6:163–168, 1963.

[53] D. Goldfarb. A family of variable metric updates derived by variational means. *Mathematics of Computing*, 24:23–26, 1970.

[54] T.G. Kolda, R.M. Lewis, and V. Torczon. A generating set direct search augmented lagrangian algorithm for optimization with a combination of general and linear constraints. Technical Report SAND2006-5315, Sandia National Laboratories, August 2006.

[55] A.R. Conn, N.I.M Gould, and Ph.L. Toint. A globally convergent augmented lagrangian algorithm for optimization with general constraints and simple bounds. *SIAM Journal on Numerical Analysis*, 28(2):545–572, 1991.

[56] A.R. Conn, N.I.M Gould, and Ph.L.Toint. A globally convergent augmented lagrangian barrier algorithm for optimization with general inequality constraints and simple bounds. *Mathematics of Computation*, 66(217):261–288, 1997.

[57] R.C. Nelson. *Flight Stability and Automatic Control*. McGraw Hill, 1998.

[58] G. Jepps. Linearized optimal control and application to a gliding projectile. Technical Report AD-A135605, December 1983.

[59] K. Cui and G. Yang. Shape optimization for hypersonic arc-wing missiles. *Journal of Spacecraft and Rockets*, 47(4):694–700, July-August 2010.